Tracking the $\nu i_{13/2}$ orbital in the neutron-deficient polonium isotopes with the high-precision ISOLTRAP mass spectrometer at CERN-ISOLDE

A thesis submitted to the University of Manchester for the degree of Doctor of Philosophy in the Faculty of Science and Engineering

2017

Numa Abdulmaeen Althubiti

School of Physics and Astronomy

University of Manchester

The remainder of this page was intentionally left blank.

Contents

The remainder of this page was intentionally left blank.

List of Figures

The remainder of this page was intentionally left blank.

List of Tables

The remainder of this page was intentionally left blank.

Abstract

The measurements that will be presented investigate the neutron-deficient polonium isotopes in the region of $A = 195 - 199$, with a special emphasis on ^{195}Po and ^{197}Po. These isotopes were produced at ISOLDE/CERN and delivered to the ISOLTRAP experiment where mass measurements and α-decay spectroscopy were performed. The decay-spectroscopy studies were carried out for the first time at ISOLTRAP with the support of the multi-reflection time-of-flight mass spectrometer (MR-TOF MS). The masses of $^{(195,197)g,m}$Po were measured precisely with Penning-trap mass spectrometry, from which the state ordering and the energy of the $13/2^+$ states in ^{195,197}Po were determined for the first time. Furthermore, the state ordering and the energy of the $13/2^+$ state in lead, radon, and radium were obtained through α-decay chains. The new data complete the knowledge of the energy systematics in this region. The presented mass measurements provide information on the behaviour of the $13/2^+$ states in the lead region near $N = 104$, which remain excited states.

Additionally, ^{195}Po half-life measurements were performed in isobarically pure conditions. The resulting ^{195g}Po half-life value is in agreement with the one in the literature, with improving in the precision of the value, whereas the ^{195m}Po half-life value is significantly smaller than the literature value.

Declaration of Authorship

I, Numa Abdulmaeen Althubiti, confirm that no portion of the work referred to in the thesis has been submitted in support of an application for another degree or qualification of this or any other university or other institute of learning.

Copyright Statement

i. The author of this thesis (including any appendices and/or schedules to this thesis) owns certain copyright or related rights in it (the "Copyright") and s/he has given The University of Manchester certain rights to use such Copyright, including for administrative purposes.

ii. Copies of this thesis, either in full or in extracts and whether in hard or electronic copy, may be made **only** in accordance with the Copyright, Designs and Patents Act 1988 (as amended) and regulations issued under it or, where appropriate, in accordance with licensing agreements which the University has from time to time. This page must form part of any such copies made.

iii. The ownership of certain Copyright, patents, designs, trade marks and other intellectual property (the "Intellectual Property") and any reproductions of copyright works in the thesis, for example graphs and tables ("Reproductions"), which may be described in this thesis, may not be owned by the author and may be owned by third parties. Such Intellectual Property and Reproductions cannot and must not be made available for use without the prior written permission of the owner(s) of the relevant Intellectual Property and/or Reproductions.

iv. Further information on the conditions under which disclosure, publication and commercialisation of this thesis, the Copyright and any Intellectual Property and/or Reproductions described in it may take place is available in the University IP Policy (see http://documents.manchester.ac.uk/DocuInfo.aspx?DocID=24420), in any relevant Thesis restriction declarations deposited in the University Library, The University Library's regulations (see http://www.library.manchester.ac.uk/about/regulations/) and in The University's policy on Presentation of Theses

Acknowledgements

I would like, first of all, to convey my sincere gratitude to my supervisor Prof. Jonathan Billowes, who was always ready to answer my enquiries with patience and directed me in the right path whenever I needed it.

Also, I would like to extend my sincere appreciation and thanks to my co-supervisor at Leuven University Dr. Thomas Elias Cocolios, who offered me a lot of help, guided me, and inspired me with confidence through my research work. I am really grateful for all your encouragement and support you have given me.

Many thanks are due to the ISOLTRAP collaborations. I am thankful and blessed to work with them. A very special gratitude goes to Dr. Vladimir Menea, thank you, most sincerely, for all the help and guidance that you have given me since I have started my research at ISOLTRAP, and for all your wonderful contributions to this work.

Special thanks are given to Dr. Kara Marie Lynch, who contributed to this work and offered me a lot of help when I wrote this thesis.

I would also like to thank Prof. Kris Heyde for his valuable inputs on my published work.

My deepest appreciation goes to the nuclear physics group at Manchester University including staff and colleagues for providing me with a helpful working environment.

I am grateful to my amazing small family including husband and children: Tareq, Layan, and Rakan, who share with me every moment and bring me love, joy, and support. *"Thank you, very much,... you make my days so special"*.

I am also very grateful to my adorable siblings, who have provided me with moral and emotional support during my life. I am blessed to have you in my life, *"you mean the world to me"*.

Finally, my dearest father, you deserve more than mere thanks words. It is just because of you I am who I am today. Thank you from the bottom of my heart for the love, kindness, encouragement that you have provided to me along the way. *"You are... God's special gift to me"*.

Mother these last words for you *"you will always stay in my heart, non-never forgotten, until we meet again "*....

The remainder of this page was intentionally left blank.

Chapter 1

Introduction

In the neutron-deficient lead region, nuclei around $Z = 82$ and below $N = 126$ are known for the phenomenon of shape coexistence [1–4]. In these nuclei, shape coexistence arises from (particle-hole) excitations of protons across the $Z{=}82$ proton closed shell to an intruder state. The intruder states have a lower excitation energy than expected from the single-particle excitation picture. Shape coexistence has been discussed extensively within the shell model description by K. Heyde and co-workers Ref. [1, 5, 6], where it has been concluded that it arises from a combination of factors including: pairing, monopole, and quadrupole interactions. The deformation is found to be maximum at $N = 104$, where the $\nu i_{13/2}$ orbital is partially depleted. Here the proton-neutron interactions between proton pairs and valence holes in the $\nu i_{13/2}$ orbital are expected to be maximal [7–12]. An interesting example of shape coexistence in this region is ^{186}Pb nucleus [7], where spherical and deformed nuclear configurations are found to compete all at an energy below 700 keV.

According to the shell model, the normal ordering of the low-lying states of odd-A isotopes in this region, starting from the $N = 126$ closed shell and moving down until reaching the mid-shell ($N = 104$), would be as follows: $3p_{1/2}$, $2f_{5/2}$, and $3p_{3/2}$, before reaching the high-spin $1i_{13/2}$ orbital, see Fig. 1.1. Thus, the sequence of the spin and parity of the ground state in these isotopes start from $1/2^-$, vary over, $5/2^-$, $3/2^-$, and then reach a spin and parity of $13/2^+$, when $N < 114$.

The single-particle shell-mode orbits in this region are shown in Fig.1.1. Such a situation is similar to what we have in the odd-A Sn nuclei. The shell model suggests that the high-spin $1i_{11/2}$ orbital gives rise to a $11/2^-$ ground state for nuclei from $A = 121$ to $A = 132$, yet this is only observed for the $A = 123$ to $A = 127$ nuclei (i.e., $N = 73$ to $N = 77$) [14, 15]. Based on this observation, it would be expected that the $13/2^+$ state is the ground state at a lower neutron number beyond the mid-shell. This, however, is not the case: experimental data in the odd-A isotopes (namely Pb, Po, and Hg) demonstrate that the high-spin $13/2^+$ state is higher in energy and is degenerate with the low-spin $3/2^-$ state halfway between the shell-closures $N = 82$ and $N = 126$ [16–18]. The pairing effect plays an essential role in lifting the high-spin $13/2^+$ state above the low-spin $3/2^-$ state. The energy gain from pairing increases linearly with increasing j [19]. Therefore, the $1i_{13/2}$ orbital is one with a large pairing energy compared to the single-particle orbitals near $3p_{3/2}$ orbital, implying that when removing a couple more neutrons from the $N = 126$ core, neutrons tend to form pairs within the $1i_{13/2}$ orbital. This will keep the ground state in the odd-neutron sequence away from having a single-particle (or hole) in the $1i_{13/2}$ orbital. Thus, the precise ordering will be influenced by the pairing energy in an orbital against the energy separation to the next higher-lying neutron orbital. Consequently, in the region with $N \sim 116$, the normal ordering for most of the ground states will be inverted. The $13/2^+$ state can remain an excited state over a long chain of isotopes and the valence neutron will occupy the $3p_{3/2}$ orbital if the single-particle energy difference between these two orbitals is smaller than the pairing gain in the $1i_{13/2}$ orbital.

Similarly, a competition between the neutron $13/2^+$ state and $3/2^-$ state was also observed in even-A thallium ($Z = 81$), bismuth ($Z = 83$) and actinium ($Z = 85$) isotopes [20–22] where the level spacings between states decrease with smaller N. The isomeric states 7^+ (10^-) that arise from $\pi s_{1/2} \otimes \nu i_{13/2}$ ($\pi h_{9/2} \otimes \nu i_{13/2}$) configurations were found to be above the ground states 2^- (3^+), that originate from $\pi s_{1/2} \otimes \nu p_{3/2}$ ($\pi h_{9/2} \otimes \nu p_{3/2}$) configuration, by about a few keV.
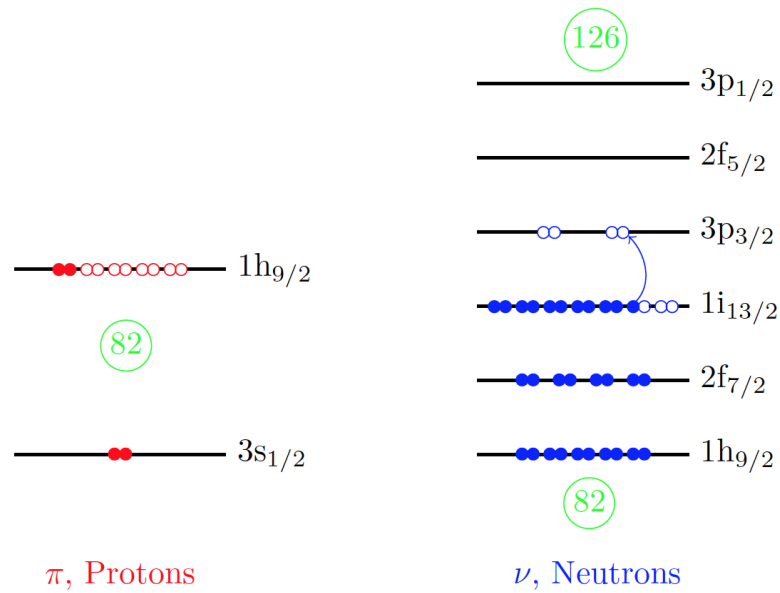
Figure 1.1: The spherical shell model orbitals in the lead region according to the experimental data on ^{207}Pb [13]. The orbitals are filled to represent ^{195}Po. The $13/2^+$ and $3/2^-$ states are determined by which orbital is occupied by the valence neutron.

The $13/2^+$ state has been investigated in previous studies, however, information about the level spacing between this state and the $3/2^-$ state is not complete near N=104, especially in odd-A lead and polonium isotopes. Most importantly, it is not known whether the $13/2^+$ state ever becomes the ground state near N=104 as the single-particle shell model would suggest.

In this regard, the measurements of the energy of the $13/2^+$ state are of interest to bridge the gap in the knowledge and to track the evolution of the nuclear structure in the lead region. As no decay path exists between these states, the excitation energy can be obtained by measuring the mass values of the isomeric and ground states with high precision. The masses of the isotopes of interest were thus measured with the ISOLTRAP mass spectrometer at CERN-ISOLDE, having relative uncertainties of 10^{-8} [23, 24]. The identification of the investigated state was needed prior to the mass measurements of each individual state. This was achieved by using a combination of the Resonance ionisation Laser Ion Source (RILIS) [25–27] with complementary α-decay spectroscopy studies.

In this thesis, the state ordering and excitation energy of odd-A polonium isotopes were revealed for the first time. The polonium isotopes were produced at ISOLDE/CERN [28] and transported to ISOLTRAP for measurements. The measurements contained two steps: α-decay measurements that were performed to identify the spin of the nuclear state, and mass measurement on the state of interest. The isomeric purification process was carried out with the combination between ISOLTRAP's MR-ToF MS [29, 30] and ISOLDE's RILIS. In addition, the extracted information from both measurements allowed the determination of the state ordering and excitation energies in odd-A lead, radon, radium through α-decay chains.

This thesis is organized as follows. Chapter 2 briefly displays the basics nuclear physics that are related to this work. Chapter 3 discusses the operating principles of the Penning trap and how it is used by the ISOLTRAP experiment for beam purification and mass measurements. The experimental setup of the ISOLTRAP facility is presented in Chapter 4. Since the ISOLTRAP's MR-TOF MS assisted the α-decay spectroscopy for the first time, some modifications to the ISOLTRAP beam-line were needed. The transmission-efficiency simulations and detection efficiencies of the decay-spectroscopy system are presented in Chapter 5. Chapter 6 discusses the data analysis and the results for each investigated states. In Chapter 7, the results of the half-life measurements that were performed at ISOLTRAP for $^{195(g,m)}$Po are presented. Finally, a summary of the results presented in this work is given in Chapter 8.

The remainder of this page was intentionally left blank.

Chapter 2

Basic principles of Nuclear Physics

For a better understanding of the nuclei properties, their structure can be described by using mathematical models. In this chapter, two basic types of simple nuclear model are briefly discussed. The macroscopic liquid-drop model, which describes the nucleus as a collective body with no individual nucleon state, while the shell model gives a description for individual nucleons in discrete energy states.

2.1 Liquid-drop model

The liquid-drop model [33] is one of the first nuclear models that was proposed to describe the nuclear properties. In some aspects, the similarity between the nucleus and a the liquid drop helps to explain global behaviours of nuclei such as nuclear masses, nuclear fission and binding energies. The liquid-drop model led to a formula that approximates the nuclear mass which is known as the "semi-empirical mass formula" (is based on the Bethe-Weizaecker formula) [34–36]:

$$B(Z, A) = a_{\mathrm{v}}A - a_{\mathrm{s}}A^{\frac{2}{3}} - a_{\mathrm{c}}\frac{Z^2}{A^{\frac{1}{3}}} - a_{\mathrm{a}}\frac{(N-Z)^2}{A} + \delta(Z, A)$$

(2.1)

$$\text{where} \quad \delta(Z, A) \begin{cases} > 0 & A \text{ even} & Z \text{ and } N \text{ even,} \\ = 0 & A \text{ odd} & Z \text{ or } N \text{ odd} \\ < 0 & A \text{ even} & Z \text{ and } N \text{ odd.} \end{cases}$$

The five parameters in Equ. (2.1) are: the volume, surface, Coulomb repulsion, asymmetry, and paining [37]. The first three terms that contribute to the binding energy of nuclei are produced from the analogy between the nucleus and the liquid-drop [34, 35]. The attempt to explain the odd-even staggering phenomenon of the binding energy and the additional binding in nuclei with $Z = N$, led to the correction to the formula [37, 38], in which the last two terms, asymmetry [36] and pairing, were added.

The binding energy of nuclei $B(A, Z)$ is defined as an energy that is needed to separate all the nucleons that form a nucleus. It is expressed in terms of the atomic mass $M_{a.m}$ as follows [39]:

$$B(A, Z) = Zm_P + Nm_N - M_{a.m}(A, Z) + Zm_e - B_e(Z).$$

(2.2)

$M_{a.m}(A, Z)$ is the experimental atomic masses, $m_{P,N}$ are proton and neutron masses, and $B_e(\mathrm{Z})$ is the binding energy of electrons.

2.2 Shell Model

The shell model is a quantum description of the nuclear structure. It is based on the assumption that each nucleon moves independently in a potential produced by the interaction with all other nucleons in the nucleus. The appropriate potential to produce the nuclear shell structure is the Woods-Saxon potential, which has an

intermediated form between the square well and the harmonic oscillator potentials
[39],

$$V(r) = \frac{-V_0}{1 + e^{(r-R_0)/a}}. \tag{2.3}$$

Here, V_0 is the potential depth, R_0 is the radius of the nucleus, $R_0 = r_0 A^{1/3}$,
r_0=1.25 fm, and $a \sim 0.5$ fm. This version of potential produces the first three
magic numbers (which are 2, 8, and 20), but not the higher ones.

In 1949 M. Mayer, D. Haxel, J. Jensen and H. Suess [40–42] proposed to add
an extra term in the nuclear potential that describes the spin-orbit interaction
$V_{os}(r)$. The $V_{os}(r)$ term re-orders the energy levels and gives the correct magic
numbers at which the higher shell closures occur. One of the major effects of the
$V_{os}(r)$ term is that the splitting in the energy levels increases proportionally to
$(2l+1)$. The energy levels resulting from Woods-Saxon potential and spin-orbit
contribution are illustrated in Fig. 2.1.

According to the shell model, the energy levels of protons and neutrons are in-
dependent and characterised by quantum numbers nlj. The maximum number
of protons or neutrons in each level is given by $(2j + 1)$, $j = l + s$. The shell
model also predicts spin (j) and parity $(\pi = -1^l)$ of nuclei in the ground state.
In even-even nuclei, all nucleons are paired and so, for each pair, the angular mo-
menta couple and then the nucleus will have zero spin and even parity. In case of
odd-odd nuclei, there is an unpaired proton and neutron. Thus, the total spin of
the nucleus will be the sum of the total angular momentum of these two unpaired
nucleons. The parity is determined by $(-1)^{l_1+l_2}$, l_1 and l_2 are the orbital angular
momenta of the remaining unpaired nucleons. In odd-A nuclei (whether Z or N
is odd), the extra-unpaired nucleon, a valence nucleon, determines the spin and
parity of the ground state and other properties. The excitation of the nuclei, from
the shell model perspective, requires to excite nucleons from one energy level to
another. The spin and parity of the nucleus will be changed according to the new
energy level that is being accommodated by the excited nucleons [39, 43].
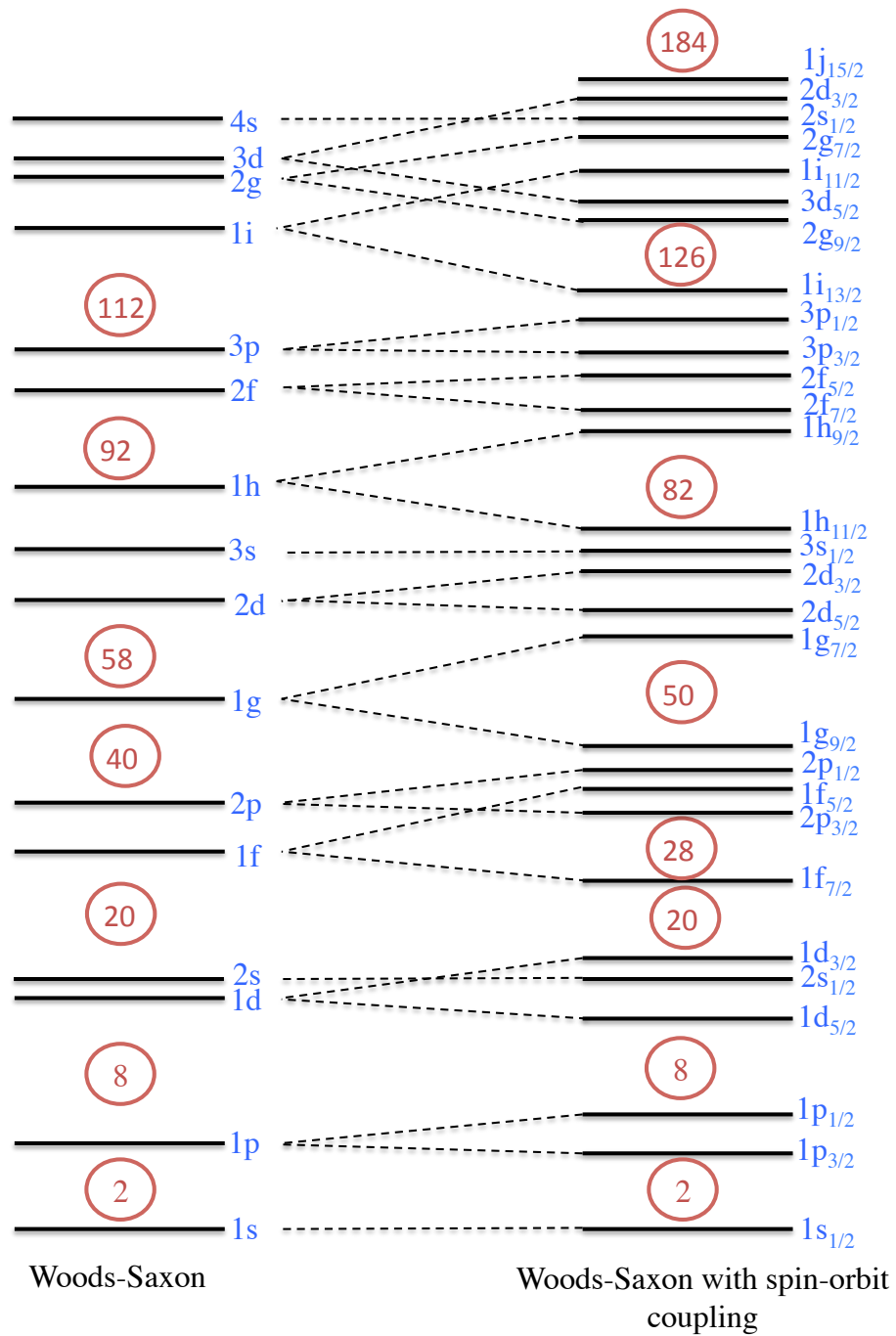
Figure 2.1: Protons and neutrons orbitals. The left column shows the magic numbers and energies of the Woods-Saxon potential. The spin-orbit coupling in nuclei leads to a split in the levels between $j = l \pm 1/2$ as shown on the right.

2.3   Collective model

The collective model [44, 45] combines some of the features of the liquid-drop model and the shell model. It was proposed to explain certain nuclear properties such as the excitation of high mass nuclei. The spherical-shell model confronts a difficulty in describing the low-energy spectra of many heavy nuclei that have the neutron or proton numbers away from the magic numbers, in particular with 150 $\lesssim$ A $\lesssim$ 190, and A $\gtrsim$ 224 [46]. The excited states in these regions are formed from collective motions of many nucleons, as opposed to the prediction of the shell model: individual nucleons move to another orbit. According to the collective model, the excitations of the nuclei can be the result from two different types of collective motion: vibrational motion, in which the nuclei vibrate about spherical or ellipsoidal shape (shape oscillations), and rotational motion of the entire nucleus [39]. The collective behaviour of nuclear states at low excitation energy is associated with a deformation in the surface. More specifically, a surface of nucleons deforms from spherical shapes. The shape of the deformed nucleus is described by the nuclear radius $R(\theta, \phi)$. For axially symmetric nuclei [39]:

$$R(\theta, \phi) = R_0 \left(1 + \beta_2 Y_2^0(\theta, \phi)\right),\tag{2.4}$$

where R_0 as defined in Eq. (2.3), and $Y_2^0(\theta, \phi)$ is the second-order spherical harmonic. β_2 is the quadrupole deformation parameter. It describes how deformed the nucleus is, positive β_2 value corresponds to the prolate shape, and the negative β_2 corresponds to the oblate shape [39].

2.4   Shape coexistence in the Pb region

Shape coexistence is a phenomenon where different nuclear shapes based on different configurations can be found in one nucleus at low energy [1]. It is observed in the neutron-deficient lead region ($Z = 82$) when moving down from $N = 126$ to $N = 104$. A well-known case is the ^{186}Pb nucleus at the mid-shell $N = 104$. Two

coexisting configurations (oblate and prolate) have been observed in addition to the spherical ground state 0^+ within less than 700 keV [7].

According to the spherical shell model description, shape coexistence can be explained through the so-called intruder states. The intruder orbitals are a result of the interaction between proton and neutron orbitals. In heavy nuclei, where there is a sufficient number of valence protons and neutrons, there is a large overlap between these orbitals. This improves the proton-neutron interactions which, in turns, decreases the excitation energy of the intruder state and leads to particle-hole excitations across a shell closure. The lowering of the energy level is linearly increased when the number of valence neutrons becomes large [1]. The attractive proton-neutron interactions can polarize the nucleus, thereby creating a significant deformation.

In neutron-deficient lead nuclei, shape coexistence occurs when a pair of protons are scattered into $h_{9/2}$ orbital, and thus forming intruder configurations [1]. For ^{186}Pb, one expects that the energy required to excite one proton pair from the closed sd shell to the $h_{9/2}$ orbit, which is above the shell closure, is ~ 7 MeV (obtained from one proton excitation in ^{208}Pb, which is determined experimentally as 3.9 MeV, [47]). However, the observed excitation energy of the intruder states is less than 7 MeV as in ^{186}Pb. Therefore, the difference in proton single-particle energies between two major shells needs to be corrected by including other factors, such as pairing and proton-neutron interactions gained from the change in the proton configurations outside the inert core. The energy of the $\pi(2p - 2h)$ intruder configuration can be described with these corrections by [1, 6]:

$$E_{intr}(0^+) = 2(E_j - E_{j'}) - \Delta E_{pairing} + \Delta E_{monopole} + \Delta E_{quadrupole}, \qquad (2.5)$$

where $2(E_j - E_{j'}) \sim 7$ MeV. E_j and $E_{j'}$ are the proton single-particle energies of j and j' orbit, respectively. The large contribution to the intruder energy comes from the last term [6], which represents the attractive quadrupole proton-neutron interaction. The strength of proton-neutron interaction increases with valence neutron space and then reaches the maximum as the mid-shell is approached.

This results in lowering the excitation energy of the intruder state, and thus reducing the shell gap.

In this picture, the first excited state in ^{186}Pb results from the $\pi(2p - 2h)$ configuration $\pi h_{9/2}^2$, and corresponds to oblate shape, while the second one comes in through $\pi(4p - 4h)$ configuration $\pi h_{9/2}^4$, and leads to the prolate shape. The spherical ground state has a $\pi(0p - 0h)$ regular configuration [1].

A similar mechanism can be used to describe the intruder configurations, with regard to change in the proton configuration in Hg , Po and Pb isotopes. According to the Eq. (2.5), the intruder energy in odd N-even Z nuclei will be affected by proton configurations and their interaction with the neutrons, which comes in through the monopole and quadrupole terms [1].

2.5   Radioactive decay

Unstable nuclei are known to exhibit a radioactive decay which is a process where the nuclei emit radioactive radiations such as α particles, β particles or γ rays. In this process, the probability of a radioactive nuclide decaying goes according to [39]:

$$A(t) = A_0 e^{-\lambda t}. \tag{2.6}$$

Here, $A(t)$ is the measured activity and A_0 is initial activity. $A(t)$ is defined as $\Delta N / \Delta t$, where ΔN is the change in the number of nuclei. The half-life $(t_{1/2})$, which is the time required to reduce the number of radioactive nuclei by a half, can be determined from the decay constant (λ) as follows [39, 48]:

$$t_{1/2} = \frac{\ln 2}{\lambda}. \tag{2.7}$$

Note that $1/\lambda$ has the dimensions of time. The half-life of radioactive isotopes can vary from less than microseconds to millions of years. For example, the half-life of ^{212}Po is 0.3 μs, while ^{40}K has a half-life $\sim 1.3 \times 10^9$ years [49, 50].

The radioactive process aims to reduce the energy of the nuclei by either trans-muting the energetic nuclei (parent) into other stable nuclei (daughter) through the emission of α or β particles, or by de-exciting the nuclei by emitting γ rays.

2.5.1 Alpha decay

In heavy elements with a proton number $Z \geqslant 82$, the binding energy per nucleon (B/A) decreases due to Coulomb repulsion, which grows as Z^2. Thus, the nuclei with high A mass tend to decay toward lighter nuclei by releasing an α particle in an attempt to reach the region of stability. In α decay, the nucleus relieves two protons and two neutrons, which is essentially a nucleus of helium. The nucleus mass reduces by 4 units of mass as the daughter nucleus is emitted [39]:

$$^{A}_{Z}P_{N} \;\rightarrow\; ^{A-4}_{Z-2}D_{N-2} + Q_{\alpha} + \alpha. \tag{2.8}$$
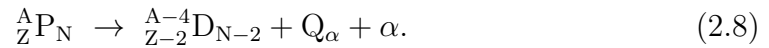
Generally, a parent nucleus can decay from ground state through α emission to either ground or one of the excited states of a daughter nucleus. As the α particle has 2 neutrons and 2 protons, they are paired to zero intrinsic spin momenta. Therefore, the total angular momentum is totally obtained by the orbital momentum l_{α}, which is in the range $\mid I_i - I_f \mid \leq l_{\alpha} \leq \mid I_i + I_f \mid$, I_i (I_f) is the angular momentum of the initial (final) state. If the initial and final states have different parities, $\pi_i \neq \pi_f$, then the parity of α emission is odd and vice versa [39]. The energy Q_{α} that is released in the decay process is given by [39]:

$$Q_{\alpha} = (m_{P} - m_{D} - m_{\alpha})c^2. \tag{2.9}$$

This decay energy will be shared between the α particle and the daughter (heavy recoiling), thus, the α-particle energy will be a bit less than Q_{α} [39]:

$$T_{\alpha} = \frac{A_{D}}{(A_{D}+4)} Q_{\alpha}, \tag{2.10}$$
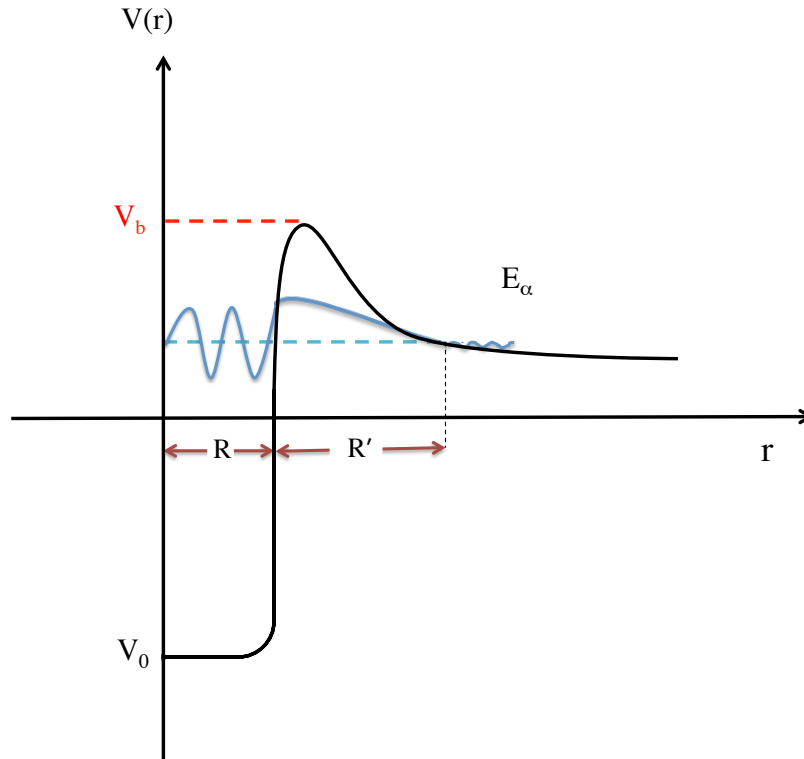
Figure 2.2: The potential energy diagram of α particle. The kinetic energy of α particles emitted from nuclei ranges from 4-10 MeV. Therefore, it is impossible classically for the α particle to overcome the Coulomb potential height V_b ($\approx$ 28 MeV for ^{238}U). However, the α particle is able to tunnel from r=R to r=R$^{'}$ and escape, when r>R$^{'}$, with an energy E_α.

where A_D is the atomic mass of the daughter. The α-particle energy is typically 4 to 10 MeV, however, this energy is small compared to the energy needed to overcome the electrical repulsion and exit the nucleus which is around 28 MeV in ^{238}U element for example. The quantum mechanic theory nicely explains the emission of the α particle through the tunnelling effect (see Fig. 2.2). Inside the nucleus, where r<R, the nucleons are confined to an attractive potential well (short range force). Outside the nucleus r>R, the nucleons are subject only to the long-range Coloumb potential. The nucleons randomly come together as an α particle (2p and 2n with particle-wave feature), tunnel through the barrier well, become free of the nuclear attraction, eject away from the nucleus by repulsion force, and then appear on the other side as α particles [39, 48].

2.5.2 Beta decay

Unstable nuclei may reach the line of stability by the emission of the β particle. The β-decay process involves three type of emissions: beta-negative decay (β^-), beta-positive decay (β^+) or electron capture (EC) [39]. The conversion of a neutron into a proton or vice versa inside the nucleus is the basic way to describe this process. In the β^- emission, a neutron converts to proton and electron as follows [39]:

$$^A_Z\text{P} \;\rightarrow\; ^{\;\;A}_{Z+1}\text{D} + \beta^- + \overline{\nu}_{\text{e}}. \tag{2.11}$$

We can write β^+ emission in analogous to the β^- process [39]:

$$^A_Z\text{P} \;\rightarrow\; ^{\;\;A}_{Z-1}\text{D} + \beta^+ + \nu_{\text{e}}. \tag{2.12}$$

In the EC process, the atomic number Z (neutron number N) is decreased (increased) by one [39]:

$$^A_Z\text{P} + \text{e}^- \;\rightarrow\; ^{\;\;A}_{Z-1}\text{D} + \nu_{\text{e}}. \tag{2.13}$$
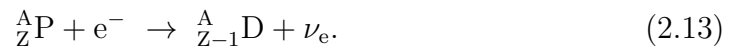
The β decay includes transmutations among isobars, at which the A remains constant in any of the three β emissions and Z changes by one [39].

2.5.3 Gamma decay

Gamma decay is often associated with α or β decay. When a nucleus is formed in a high-lying state, it decays to the lower states and releases its extra energy by emitting photons. The γ-ray energy corresponds to the energy difference between the initial and final nuclear states (neglecting the recoil energy) [39]:

$$\text{E}_\gamma = \text{E}_{\text{i}} - \text{E}_{\text{f}} \tag{2.14}$$

The total angular momentum of the photon I can take any value between $\mid I_i - I_f \mid$ and $\mid I_i + I_f \mid$, with the exception that I can not be zero.

Two different transitions can be classified between nuclear states; electric and magnetic transitions. The parity π of the photon is subject to selection rules depending on the type of transition and the angular momentum I [39]:

$$\pi = \begin{cases} (-1)^I & \text{for electric transitions,} \\ (-1)^{I+1} & \text{for magnetic transitions.} \end{cases}$$

The angular momenta and the parity of the initial and final nuclear states will determine the type of transition. If the two nuclear states have the same parity $\pi_i = \pi_f$ then, even angular momentum I characterises the electric, while the odd angular momentum I characterises the magnetic. In case of the two nuclear states have different parity $\pi_i \neq \pi_f$, the transition is electric for odd I, and magnetic for even I [39, 48].

2.5.4   Internal conversion

Another electromagnetic process, which could compete gamma emission, is what is known as internal conversion. Nucleus in this process de-excites to the ground state by transferring its energy to the orbital electron (usually K- electron) [39]. The energetic electron will then be ejected from the atom and another electron that occupies a high energy level will fill the vacancy. This results in X-rays emission due to the difference in energy between the two levels. The electron will be emitted with an energy E_e less than the excitation energy E^* by an amount equals to the binding energy of the orbital electron E_B.

As this decay process competes with gamma emission photons, one can define the ratio between these process as follows [39]:

$$\alpha = \frac{N_e}{N_\gamma}, \tag{2.15}$$

where α is the internal conversion coefficient, N_e is the number of decays via internal conversion and N_γ is number of decays via gamma rays [39].

The remainder of this page was intentionally left blank.

Chapter 3

Ion traps for mass measurements and beam purification

The ISOLTRAP mass spectrometer at ISOLDE/CERN was used to determine precisely the masses of Po isotopes, which will be described in this work. ISOLTRAP currently consists of four ion traps [23, 24]. They use either static or radio-frequency electromagnetic fields to confine radioactive ions in a well-defined volume, allowing their study for a time limited only by their decay half-life and hence achieving high precision measurements. For this work, three of the four ion traps were used for beam preparation and purification and one for mass measurements. In the following, their basic operating principles will be presented

3.1   Ion motion in a Penning trap

A Penning trap is considered a useful tool to determine the atomic mass of a confined ion [51, 52]. The confinement of the ion in the xy-plane can be achieved by a homogeneous magnetic field $\vec{B}$. In addition, the ion is trapped in the z-axis direction by means of an electric quadrupole field. In practice, the electric field is produced by a set of three electrodes, a central one called a ring electrode and the other two are called end caps (as shown in Fig. 3.1). Correction electrodes
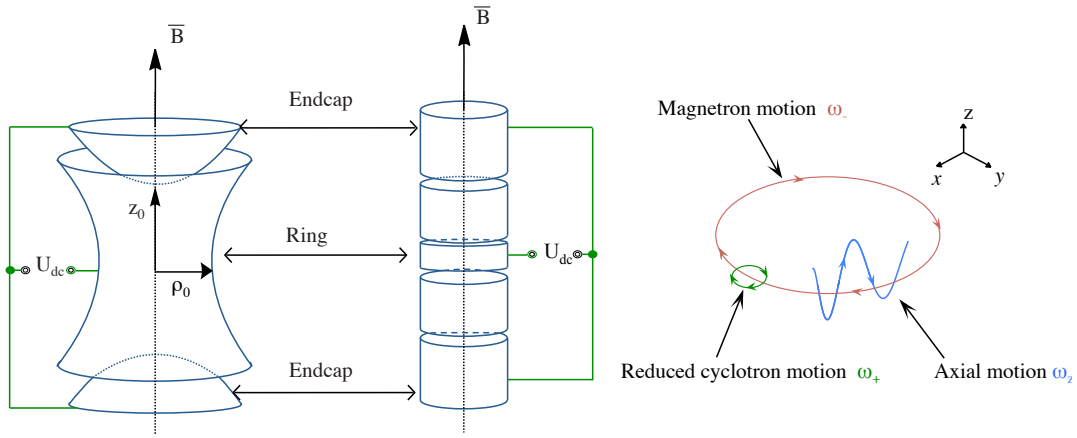
Figure 3.1: Hyperbolic and cylindrical Penning trap configurations are illustrated on the left. The right diagram shows the three motions of the ion in the Penning trap.

are added to achieve a very precise quadrupole potential (as shown in Fig. 3.1 for a cylindrical-shaped trap). The magnetic field is added by inserting the electrode set in a very homogeneous superconducting magnet.

This results in different motions of the ion in the Penning trap: a cyclotron motion, a magnetron motion, and an axial motion in the z-axis direction. The two former motions give a radial epicyclic orbit in xy-plane. The three motions are illustrated in Fig. 3.1.

Assume a particle with a mass of m, carrying a charge q and placed in a magnetic field $\vec{B}$. This particle will move in a cyclotron orbit due to the Lorentz force $\vec{F}_{Lor}$ [52]:

$$\vec{F}_{Lor} = q(\vec{v} \times \vec{B}). \tag{3.1}$$

The cyclotron motion is periodic, with a cyclotron frequency given by:

$$\omega_c = \frac{q}{m} B \; \hat{z}. \tag{3.2}$$

In an ideal Penning trap, the ion will be confined axially by an electrical force produced by the quadrupole potential $U(z, r)$ [52]:

$$U(z, \rho) = U_{dc} \frac{(2z^2 - \rho^2)}{4d^2}, \tag{3.3}$$

$$\rho^2 = x^2 + y^2, \tag{3.4}$$

where $d^2 = \frac{1}{4}(2z_0^2 + \rho_0^2)$ stands for the so-called "characteristic trap dimension" and is given in a hyperbolic Penning trap (such as the precision trap of ISOLTRAP) by the constant z_0 and ρ_0 at the minimum axial and radial distances, respectively. U_{dc} stands for the voltage difference that is applied between the end caps and the ring electrode.

The equations of the ion motion can be derived starting from the Lorentz and electrical forces that act on the ion in the Penning trap as follows [52]:

$$\ddot{\vec{r}} = \frac{q}{m}(\vec{E} + \vec{v} \times \vec{B}). \tag{3.5}$$

Using $\vec{B} = B\vec{e}_z$, and defining the electric field in terms of the quadrupole potential, $U(z, \rho)$, as $\vec{E} = -\vec{\nabla}U(z, \rho)$, Eq. (3.5) can be reformulated as [52]:

$$\begin{pmatrix} \ddot{x} \\ \ddot{y} \\ \ddot{z} \end{pmatrix} = \frac{qU_{dc}}{2md^2} \begin{pmatrix} x \\ y \\ -2z \end{pmatrix} + \frac{q}{m}B \begin{pmatrix} \dot{y} \\ -\dot{x} \\ 0 \end{pmatrix}. \tag{3.6}$$

The equation of the axial motion has the following structure:

$$\ddot{z} + \omega_z^2 z = 0. \tag{3.7}$$

This equation represents a simple harmonic motion, with an axial frequency ω_z:

$$\omega_z = \sqrt{U_{dc}\frac{q}{md^2}}. \tag{3.8}$$

The radial components can be written using the definition of the ω_c and ω_z, as follows:

$$\begin{pmatrix} \ddot{x} \\ \ddot{y} \end{pmatrix} - \omega_c \begin{pmatrix} \dot{y} \\ -\dot{x} \end{pmatrix} - \frac{1}{2}\omega_z^2 \begin{pmatrix} x \\ y \end{pmatrix} = 0. \qquad (3.9)$$

The solution of the Eq. (3.9) shows that the radial motion combines two circular motions (cyclotron and magnetron motion) with the following eigenfrequencies [52]:

$$\omega_\pm = \frac{1}{2}[\omega_c \pm \sqrt{\omega_c^2 - 2\omega_z^2}], \qquad (3.10)$$

where ω_- and ω_+ are the magnetron and reduced cyclotron frequencies, respectively. They satisfied the following relation [52]:

$$\omega_c = \omega_+ + \omega_-. \qquad (3.11)$$

Three important relations for the Penning trap mass spectrometry can be deduced from Eq. (3.8) and Eq. (3.10):

- The magnitudes of the radial and axial frequencies have the following order:

$$\omega_- < \omega_z < \omega_+. \qquad (3.12)$$

- In order to achieve the ion confinement the quantities $\omega_c^2 - 2\omega_z^2$ and qU_{dc} must be real. The use of the Eq. (3.2) and Eq. (3.8) results in the condition of a stable confinement from which the minimum magnetic field can be determined [52]:

$$\frac{qB}{m} > 2\frac{U_{dc}}{d^2}. \qquad (3.13)$$

- The Taylor expansion for the Eq. (3.10) results in the following expressions:

$$\omega_- \approx \frac{U_{dc}}{2dB}, \tag{3.14}$$

$$\omega_+ \approx \omega_c - \frac{U_{dc}}{2dB}, \tag{3.15}$$

it follows, to the first order, that the magnetron motion is mass-charge independent.

3.2 Excitation modes of the ion motion in the Penning trap

In the Penning trap, the ion motions can be controlled by applying radio frequency electric (rf) fields, namely dipolar and quadrupolar fields, to the electrodes. Two excitation modes are used to either eliminate unwanted ions (isobaric mass separation) or to couple different ion motions. The dipolar field is accomplished by applying a rf voltage to the ring segments with opposite phase on opposite segments (see Fig. 3.2, left panel). It can be utilized to remove an undesired ion from the trap [23]. Depending on the frequency of the applied field, it is possible to excite the magnetron or the reduced cyclotron motion.

The magnetron motion of ions can be excited when a dipolar rf field, with $\omega_d = \omega_-$ is applied. The excitation of the magnetron motion increases the magnetron orbit of all ions with different masses and then removes them from the trap centre. If only one ion species needs to be driven away from the trap centre, then a dipolar rf field with $\omega_d = \omega_+$ has to be applied [23].

The quadrupolar excitation is achieved when a rf field U_q, with a frequency ω_q, is applied to the ring segments with the same phase on opposite segments (see Fig. 3.2, right panel). This excitation mode aims to convert the ion motion from one radial mode to another. A full conversion, from one radial motion to another, can be accomplished when ω_q matches the cyclotron frequency $\omega_c = \omega_+ + \omega_-$ [54].
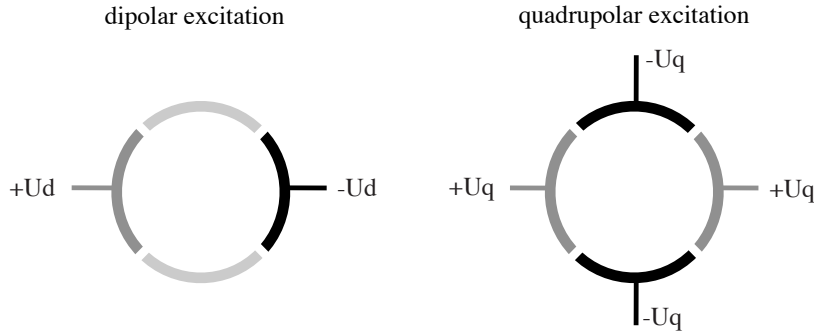
Figure 3.2: A dipolar excitation is obtained by applying the rf field to two opposite ring segments and a quadrupolar excitation is obtained by applying the rf field to all rings segments, in quadrature.

The conversion process takes some time and it depends on the amplitude of the applied quadrupole voltage [23]:

$$T_{conv} \propto \frac{1}{U_q}. \tag{3.16}$$

The conversion of the initial magnetron motion into a cyclotron motion affects the radial energy of the ions. The orbit of the magnetron motion becomes smaller, while at of the cyclotron motion increases, until, for full conversion, it becomes equal to the initial magnetron orbit, see Figure. 3.3. Due to the much higher cyclotron frequency, the radial energy is this way significantly enhanced [23].

3.3 Mass-selective buffer-gas centring technique in the Penning trap

The so-called mass-selective buffer-gas centring technique employs a rf field, to excite the ion motions, and a buffer gas (typically is the helium gas at low pressure of the order of a 10^{-5} mbar) to cool the ions and then damp the axial and radial ion motions. The radial cooling is also employed as a means to separate the ions of interest from others species [23]. In this technique, the ion motion can be
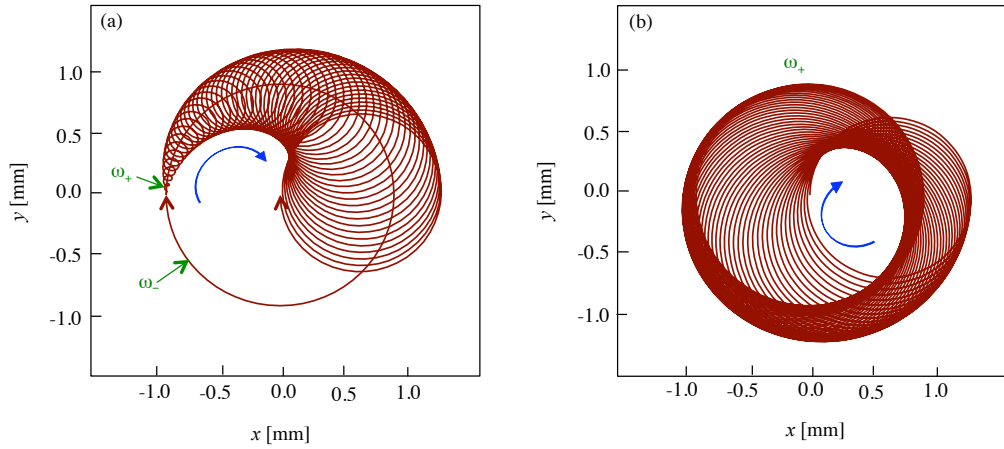
Figure 3.3: The conversion between the two radial motions due to quadrupole excitation. (a) illustrates the magnetron motion at the beginning of the conversion process. (b) shows a full conversion from one radial motion to another when $\omega_q = \omega_c$.

excited with a dipole excitation at ω_-. This excision mode leads to an increase in the magnetron orbit for all ions, since the frequency ω_- is in first order mass-charge independent. To separate the ions of interest from other ion species, a quadrupole excitation at a cyclotron frequency of ω_c has to be applied. The quadrupole excitation couples the two radial motions and resonantly converts the magnetron motion into the cyclotron motion. Consequently, the orbit of the magnetron motion of the ions of interest is reduced with a concomitant expansion in the orbit of the cyclotron motion (the cyclotron motion is much faster and will, therefore, induce many more collisions with the helium gas, hereby damping the motion faster for the excited ions than for the non-excited ions). This increase in cyclotron motion will be damped due to the helium gas. Therefore, the ion of interest will be driven to the centre of the trap, as shown in Fig. 3.4(b), while the unwanted species remain on a large orbit [23, 55].
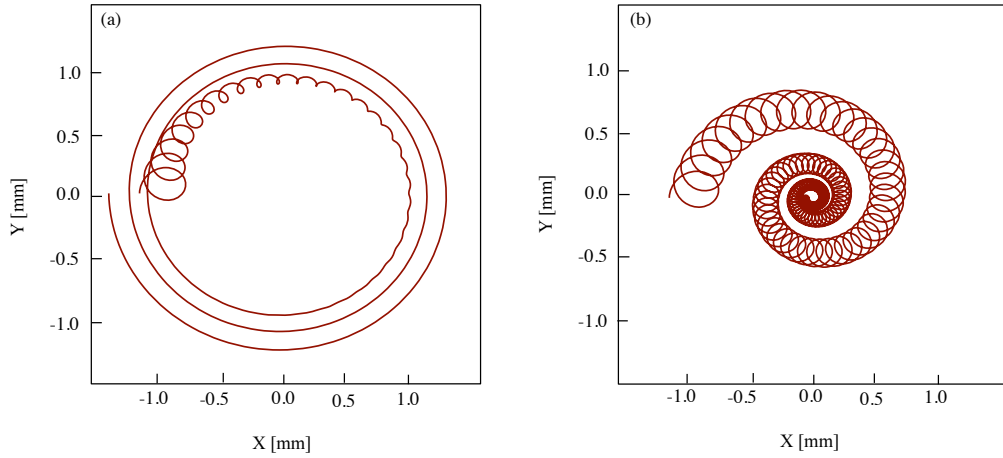
Figure 3.4: The ion motion in a buffer-gas-filled Penning trap. (a) shows a decrease (increase) in the orbit of the cyclotron (magnetron) motion results from the ion-helium collisions. (b) shows the mass-selective centring where both motions (cyclotron and magnetron) are simultaneously decreased.

3.4 Cyclotron frequency measurements

The time-of-flight ion-cyclotron-resonance (ToF-ICR) method [56] is employed at ISOLTRAP to measure the cyclotron frequency of the ion [57]. In the TOF-ICR method, the ion is released from the precision Penning trap and guided towards a micro channel plate (MCP) detector, which is placed at a distance out of the magnetic field strength. The time-of-flight (ToF), starting from the center of the trap until reaching the MCP, can be measured and allows sensing the response of the detected ions excitations applied while they were trapped [23].

Assuming that the ions in the Penning trap are first excited by a dipolar excitation and then by a quadrupolar excitation with frequency $\omega_q = \omega_c$, the magnetron motion will be turned into the cyclotron motion. The conversion between the two radial motions leads to an enhancement in the radial kinetic energy E_r since $\omega_+ \gg \omega_-$. Due to the radial motion, the ions will possess a magnetic moment μ when they are ejected from the Penning trap and exit the region of the strong magnetic field $\vec{B}$ [23]:
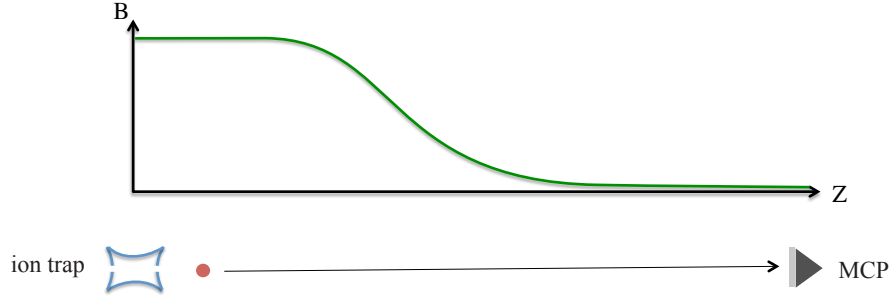
Figure 3.5: Schematic of the flight path of the ion after ejection from the Penning trap. In ToF-ICR technique one measures the ToF of the ion from the center of the trap to the MCP through the magnetic field gradient [56].

$$\mu \approx \frac{E_r}{B}. \tag{3.17}$$

In this region, the radial energy will be converted to an axial energy under the influence of the force $\vec{F}$ resulting from the magnetic-field gradient [23] (see Fig. 3.5):

$$\vec{F} = -\vec{\mu} \cdot (\vec{\nabla}\vec{B}) = -\frac{E_r}{B}\frac{\partial B}{\partial z}\hat{z}. \tag{3.18}$$

The time that is required for the ion to travel from the center of the trap to the MCP is given by [23]:

$$T(\omega_q) = \int_0^{z_1} \sqrt{\frac{m}{2(E_0 - qU(z) - \mu(\omega_q)B(z))}}dz. \tag{3.19}$$

Here the initial kinetic energy (magnetic field) in the z-direction is represented by E_0 ($B(z)$), while $U(z)$ represents the electrostatic voltage [23]. In Eq. (3.19) we already expressed the general case, in which the conversion frequency is not necessarily equal to the ω_c of the ion and hence the magnetic moment can take different values, depending on the degree of conversion.

Figure. 3.6 shows the ToF resonance of ^{133}Cs$^+$, in which the minimum ToF is observed in the resonance case $\omega_q = \omega_c$. The minimum ToF follows from the fact that the radial energy has its maximum value at $\omega_q = \omega_c$, and thus the $\mu(\omega_q)$ will
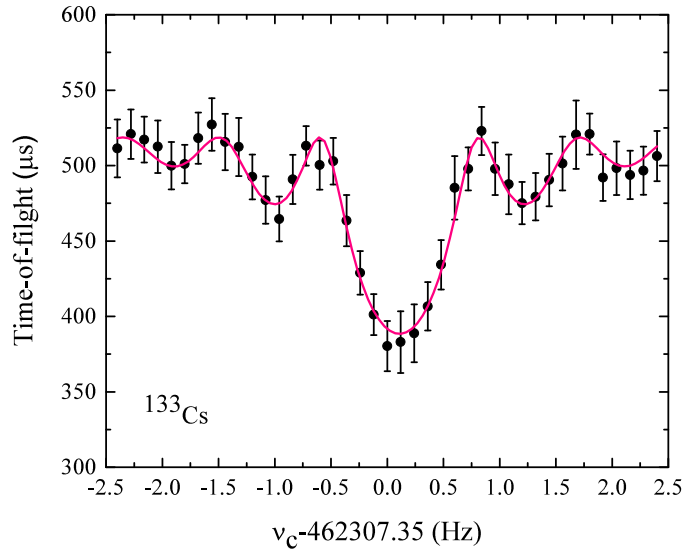
Figure 3.6: The ToF-ICR resonance of ^{133}Cs$^+$. The cesium isotope was produced off-line (in preparation for the polonium run) by using the ion source at ISOLTRAP. The cyclotron frequency was measured with T_q=1.2 s. The pink line represents the fit of the experimental data to the theoretical model [57].

be maximum according to Eq. (3.17). Conversely, the non-resonant excitation $\omega_q \neq \omega_c$ leads to a smaller magnetic moment and hence shows an increase in the ToF.

It must be noted that the precision of the cyclotron-frequency measurement depends on the full-width-at-half-maximum (FWHM) of the peak, which itself depends on the length of the duration time required for the quadrupole excitation (T_q) [58]. Therefore, the resolving power of the precision traps obeys the following equation [23]:

$$R = \frac{\nu_c}{\Delta\nu(FWHM)} = \frac{m}{\Delta m} \approx \nu_c \cdot T_q. \tag{3.20}$$

Here, $\nu_c = \omega_c/2\pi$ and $\Delta\nu$ is the spectral width of the peak. Longer excitation time is used to reduce the width of the resonance peak and enhance the resolving power [59]. However, in the case of short-lived radionuclides, the possible T_q of the excitation is limited by the half-life of the ion of interest. The radioactive decay process will likely take place if the ion half-life is shorter than T_q. As a consequence of that, the number of ions will be reduced [23]. In addition,

collisions with rest gas molecules can limit the resolution for long excitation times. This is dependent on the vacuum quality in the Penning trap and requires the whole system to operate at pressures better than 10^{-8} mbar.

The remainder of this page was intentionally left blank.

Chapter 4

Experimental setup of ISOLTRAP

4.1 The radioactive ion beam source at ISOLDE

The Isotope mass Separator On-Line Device facility (ISOLDE) at CERN is dedicated to producing a variety of radioactive ion beams [61]. The experimental hall of ISOLDE is shown in Fig. 4.1 [60]. The radioactive elements are produced by protons, with a kinetic energy of 1.4 GeV, coming from the Proton-Synchrotron-Booster (PSB). The accelerated proton impinges on a thick target, e.g., uranium carbide UC_x, [28, 62]. The radioactive products resulting from the nuclear reactions are stopped in the target material. In order to release them, the target is heated to a temperature of 2000°C, which facilitates the processes of diffusion and effusion from the target material into an ionisation cavity. The ionisation process is accomplished by using one of three ionisation techniques: surface ionisation [63], plasma ionisation [64] and laser ionisation with RILIS [25–27]. The last method is an element-selective, providing a beam with a superior purity. During the ionisation procedure, unwanted nuclides can also be ionised (by surface) and contaminate the ion beam. These contaminants can be removed by magnetic mass separators. At ISOLDE, there are two mass separators: the high-resolution
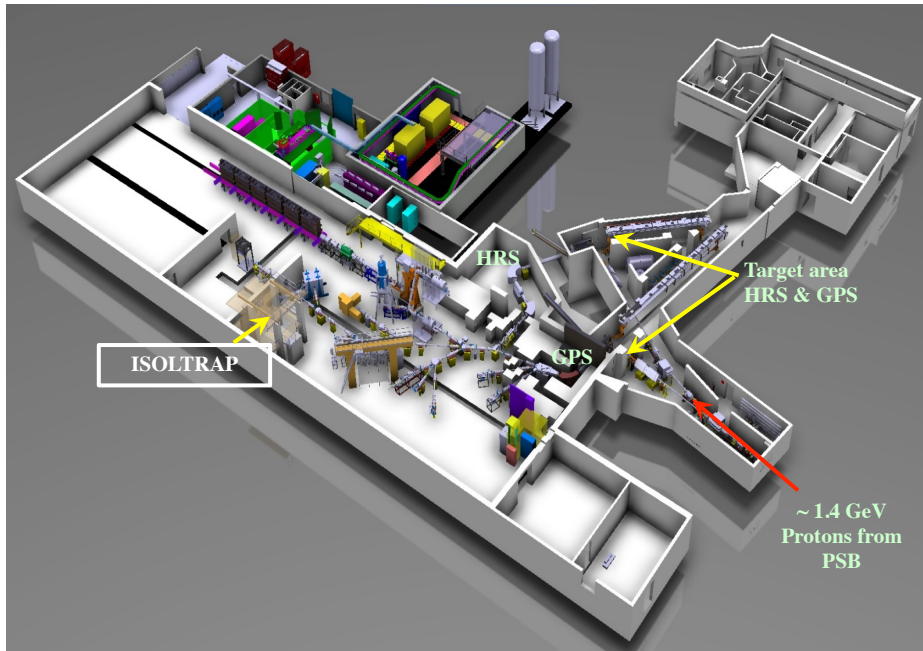
Figure 4.1: The schematic view of the ISOLDE facility at CERN. A thick target is bombarded with 1.4 GeV protons from the PSB. Proton-induced reactions in the target lead to the production of different isotopes. The isotopes are then ionised, separated with HRS or GPS and then forwarded to different experiments. The ISOLTRAP experiment is shown on the left [60].

separator (HRS) [65] and the general purpose separator (GPS). They are different from one another in design and resolution. The HRS is configured with two magnet mass separators, thus achieving a high resolving power of $R = m/\Delta m$ up to 5000. The GPS has one magnetic mass separator with $R \approx 1200$. Starting from the ion source, the ion beam is accelerated to 30-60 keV and transported through the separator to different ISOLDE experiments [66].

4.2   The ISOLTRAP facility

The ISOLTRAP facility is situated at ISOLDE (CERN). It is dedicated to measure the masses of nuclei with a relative precision down to $\delta m/m \approx 10^{-8}$ [23, 24] and resolving power up to 10^6 [23]. The ISOLTRAP experiment is composed of: a radio-frequency quadrupole (RFQ) trap [67] for preparing ion beams; two
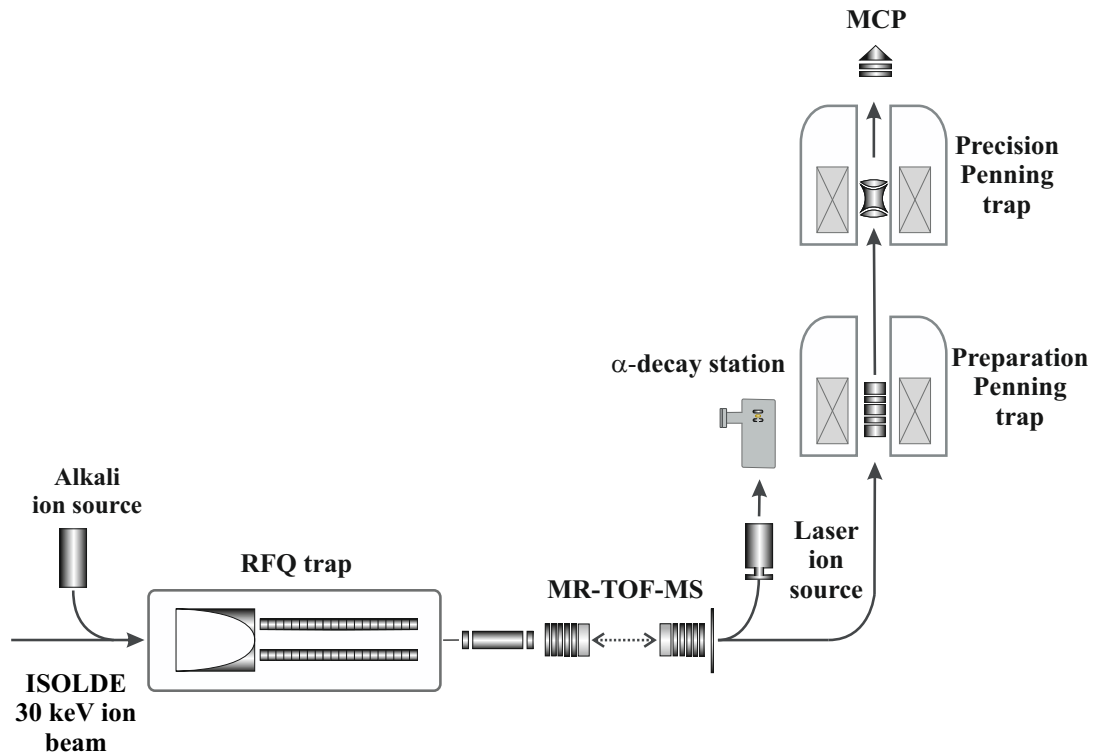
Figure 4.2: The schematic diagram of the ISOLTRAP setup as used in this work. This figure is taken from Ref. [68]

Penning traps [69, 70] for confining and purifying ion beams from isobaric contaminations; and the multi-reflection time-of-flight mass separator (MR-ToF MS) for isobaric separation [29, 71]. In addition to these parts, a decay-spectroscopy station can be installed to assist mass measurements studies. It can be added behind the precision Penning trap as was shown in Refs. [20, 80], or placed directly after MR-ToF MS. The following sections present the descriptions of the setup at ISOLTRAP. The schematic diagram of the setup is indicated in Fig. 4.2.

4.2.1   Linear radio-frequency quadrupole (RFQ) trap

A linear radio-frequency quadrupole (RFQ) trap is designed to accumulate and decelerate the ions. The configuration of the RFQ trap is shown in Fig. 4.3. It comprises four segmented rods on which rf potentials can be applied [67]. The cooling method requires the RFQ trap to be filled with a 10^{-3} mbar helium gas. The ions that are injected into the RFQ trap undergo three processes: cooling,
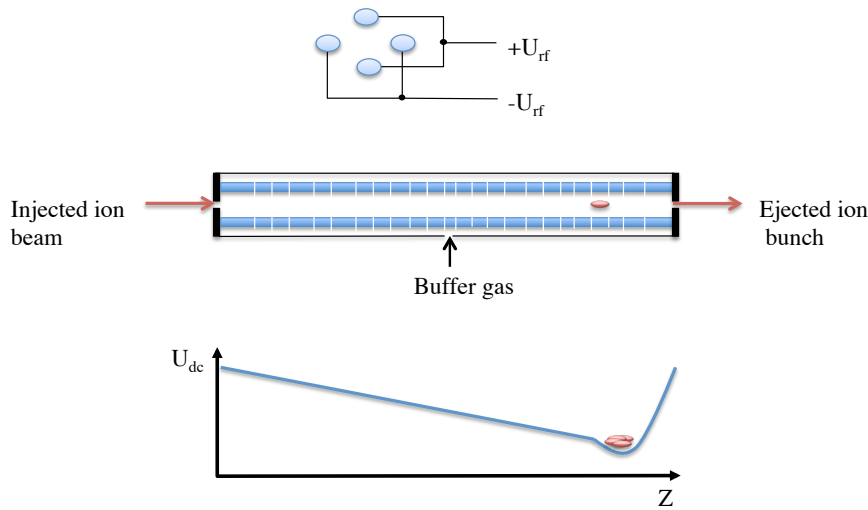
Figure 4.3: Schematic view of the RFQ trap. The top view is a cross section showing the connection of the rf potential to the electrode rods. The middle shows the axially segmented electrodes of the RFQ trap. The bottom shows the axial dc potential that is used to accumulate ions and then eject the bunch.

accumulation and the release as a narrow bunch. In the first process, the rf voltages are applied to the electrodes, which lead ions to be radially confined. A three-dimensional confinement is achieved when a dc potential is applied to the segmented rods. In the cooling process, the ions lose a part of their energy through successive collisions with the helium gas. In preparation for the accumulation process, a potential minimum is produced axially to capture the scattered ions. Therefore, the ions move toward the potential and accumulate before the end of the trap [67]. In the final process, the potential of the last segments is switched and the ion bunch is ejected to the MR-ToF MS [23].

4.2.2   Multi-reflection time-of-flight mass separator (MR-ToF MS)

The multi-reflection time-of-flight mass separator (MR-ToF MS) is one of the most recent additions to the ISOLTRAP experiment [29, 71]. It is coupled with the RFQ trap and the Penning traps, see Fig. 4.2. The MR-ToF MS can be used to measure the masses of shorter-lived nuclides or those nuclides that have
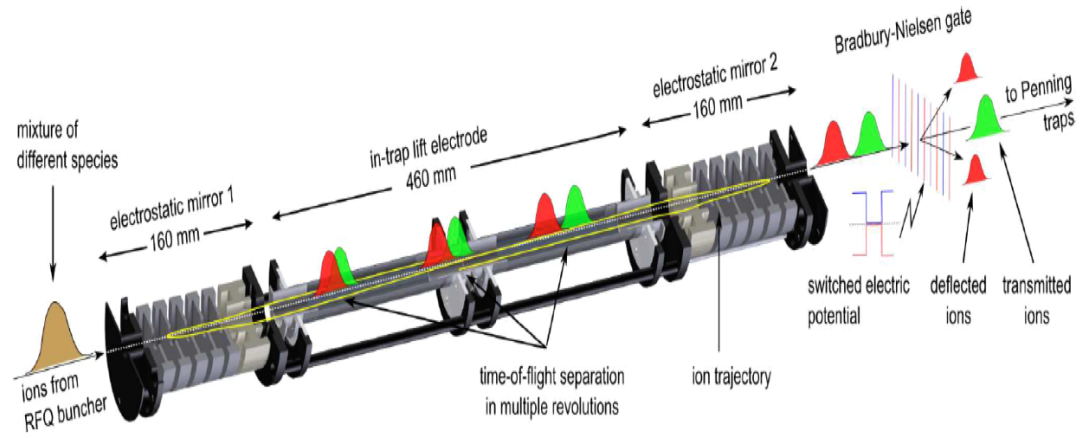
Figure 4.4: Multi-reflection time-of-flight mass separator at ISOLTRAP [29].

a yield too small to be measured with the Penning trap [72, 73]. Moreover, the MR-ToF MS is used as a purification system at ISOLTRAP. As illustrated in Fig. 4.4, the MR-ToF MS contains two 160 mm-long electrostatic mirrors. The ions can be reflected between the mirrors up to a thousand times or more back and forth. Ions with different masses are distinguished temporally by their different velocities. By using this temporal separation, the unwanted isobaric species can be deflected and the ions of interest transmitted by the use of a Bradbury-Nielson gate. A resolving power on the order of 10^5 is achieved in the MR-ToF MS within only 20-30 ms [71].

4.2.3 Preparation Penning

The ejected ion beam from the MR-ToF MS is captured into the first Penning trap which is known as the preparation Penning trap [74]. It is a cylindrical Penning trap inserted in a 4.7 T magnetic field strength and filled with 10^{-5} mbar helium gas. The ion bunch is prepared for the later frequency measurements through a process of cooling and purifying [55]. The purification cycle is performed by employing the mass-selective buffer-gas centring technique, previously described in Section 3.3. The ions of interest can be separated from different isobars with a resolving power; $R = 10^4 - 10^5$ and then ejected to the next Penning trap. The

preparation Penning trap ensures an optimal injection of the purified ions into the precision Penning trap [23].

4.2.4   Precision Penning trap

The precision Penning trap is the second Penning trap. It is a hyperbolic Penning trap and is situated in a 5.9 T magnetic field strength. In this trap, the mass is measured by using the TOF-ICR method. The measurement process requires applying the magnetron dipolar excitation and later the cyclotron quadrupolar excitation [23]. This is achieved in the same way as in the preparation trap but with the major difference that the first trap is filled with buffer gas and the second is operated under an ultra-high vacuum of $< 10^{-8}$ mbar [59]. After the excitation is stopped, the ion is ejected from the trap towards the ToF section in order to measure the cyclotron frequency as described in Section 3.4.

4.2.5   Mass determination

Referring to Section 3.1, the mass can be derived from the cyclotron frequency expression in Eq. (3.2). In order to obtain the mass, one needs to eliminate the dependence on $\vec{B}$. To this end, in addition to the cyclotron-frequency measurement of the nuclide of interest $\nu_{c,n}$, a cyclotron frequency of a reference nuclide $\nu_{c,ref}$ has to be measured. At ISOLTRAP, there are two off-line ion sources that are used in mass measurement to produce reference ions [75, 76].

The atomic mass of the nuclide of interest m_n can be determined from the weighted average cyclotron-frequency ratios $\bar{r}$ as follows [23]:

$$m_n = \bar{r} \left(m_{ref} - m_e \right) + m_e, \qquad (4.1)$$

where m_{ref} and m_e are the atomic masses of the reference nuclide and the electron, respectively. The weighted average cyclotron-frequency ratios $\bar{r}$ is given by [23]:
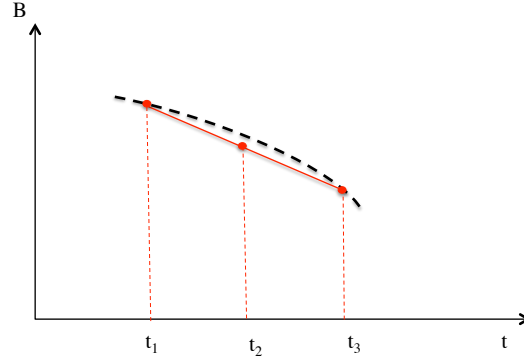
Figure 4.5: Schematic illustration of the magnetic field calibration. The black dashed line represents the magnetic field and the red line is the linear interpolation. The time of the reference ion measurements are performed at t_1 and t_3, while t_2 is time of the actual measurement.

$$\bar{r} = \frac{\sum_i [r_{ref,n}^i / (u_{r_{ref,n}^i})^2]}{\sum_i [1/(u_{r_{ref,n}^i})^2]}, \tag{4.2}$$

where $r_{ref,n}^i = \frac{\nu_{c,ref}^i}{\nu_{c,n}^i}$ denotes the cyclotron-frequency ratio of the i-th measurement, $u_{r_{ref,n}^i}$ is the uncertainty of $r_{ref,n}^i$. The ratio, $r_{ref,n}^i$, can be determined at a given time t_2 (see Fig. 4.5), by measuring $\nu_{c,ref}$ before and after, (i.e., at t_1 and t_3), the measurement of $\nu_{c,n}$. Then, a linear interpolation of $\nu_{c,ref}$ to the measurement time of the nuclide of interest t_2 is performed, according to [23]:

$$\nu_{c,ref}(t_2) = t_2 \cdot \frac{\nu_{c,ref}(t_3) - \nu_{c,ref}(t_1)}{t_3 - t_1} + \frac{t_3 \nu_{c,ref}(t_1) - t_1 \nu_{c,ref}(t_3)}{t_3 - t_1}. \tag{4.3}$$

The uncertainty of the cyclotron-frequency ratio $r_{ref,n}^i$ is determined by considering statistical and systematic uncertainties. The statistical uncertainty of $\nu_{c,ref}$ and $\nu_{c,n}$ are inversely proportional to the number of the counts N and T_q [75]. The systematic uncertainty at ISOLTRAP results from different sources. The drift in the magnetic field between the measurements is the important error source in mass measurements. The ratio $r_{ref,n}^i$ that is resulted from the linear interpolation of the reference measurement to the actual measurement time, is affected by non-linear magnetic field fluctuations. Thus, the error due to the non-linear magnetic fluctuations [77] (which is in order of 6.35×10^{-11} 1/min) is added quadratically

to the statistical error [23, 78, 79]:

$$u_{r_{ref,n}^i} = \sqrt{(u_{r_{ref,n}^i})_{stat}^2 + (u_{r_{ref,n}^i})_B^2}. \tag{4.4}$$

The uncertainty of $\bar{r}$ is then given by:

$$u_{\bar{r}} = \sqrt{\frac{1}{\sum_i [1/(u_{r_{ref,n}^i})^2]}}. \tag{4.5}$$

Another source of the systematic error comes from the mass difference between the reference and the nuclide of interest [75]. This systematic effect leads to a shift in the cyclotron frequency proportional to the difference between the two masses. The total uncertainty of $\bar{r}$ can be obtained after considering the mass-dependent error as [23, 75]:

$$u_{\bar{r}_{tot}} = \sqrt{(u_{\bar{r}})^2 + (u_{r_{ref,n}})_m^2}. \tag{4.6}$$

4.2.6 Decay station at ISOLTRAP

For decay spectroscopy measurements at ISOLTRAP, a decay-spectroscopy system can be added either behind the Penning traps [20, 80] or the MR-ToF MS as was performed in this work. The decay spectroscopy offers access to the information resulting from nuclear decays, such as α, β, and γ transitions that are used to identify the ground and isomeric states in nuclei.

4.2.6.1 Decay tape station:

A typical setup includes a decay chamber that houses a collimator to reduce the implantation area and also a movable Mylar tape for the ion implantation [81]. The tape movement facilitates the transfer of unwanted radioactive products to another point before implanting a new bunch. In the implantation area, the tape is surrounded by a thick plastic-scintillator tube which is 5 cm long and 2 mm thick. In addition, the plastic-scintillator is connected via a light guide to two

photomultiplier tubes for measuring the β decay signals. There can also be up to three germanium detectors around the chamber for measuring the energy of γ particles [81]. This decay system is suited to study β decay but in case of α decay the high absorption inside the tape material can lead to low efficiency in the α detection. In other words, the α particle could be stopped by the tape material before reaching the detector. Thus, in the measurements that require a study of α decay, the α-decay spectroscopy station [82] is favoured over the tape. Concerning the vacuum, the system is directly connected to the precision Penning trap. It is essential, therefore, to be operated under vacuum 10^{-8} mbar. However, the typical vacuum of the tape station is about $10^{-5} - 10^{-6}$ mbar which is a poor vacuum compared to the vacuum in the mass-measurement section. Moreover, the space limitation imposed by the ISOLDE overhead crane leaves only a little room for the decay chamber and detectors and, thus, any additional element that could enhance the vacuum is difficult to install.

4.2.6.2   CRIS decay-spectroscopy station (DSS2.0)

The new CRIS decay-spectroscopy station (DSS2.0) (see Fig. 4.6) is a small rectangular decay chamber with a 10×10 cm^2 cross section and aluminium walls designed to avoid the attenuation of γ rays [82]. Inside the aluminium chamber, there are three main elements: a collimator, carbon foil (C-foil) and two silicon detectors. The collimator is placed in front of the ion beam line and has an aperture of 4 mm at the centre. After the passage of the beam through the aperture, the ion will be implanted into the C-foil which has a thickness of $\approx$90 nm [82]. To record α energies the carbon foil is surrounded by two silicon detectors; passivated implanted planar silicon (PIPS) and annular PIPS (APIPS) as shown in Fig. 4.6.

The PIPS detector is in the form of a solid detector with an active area $300\,\mathrm{mm}^2$ and placed 3.5 mm behind the foil. The APIPS detector is shaped in an annular ring with an active area of $450\,\mathrm{mm}^2$ and positioned at a distance of 4 mm before the foil to measure the energy of the backscattered α (i.e., αs that are emitted
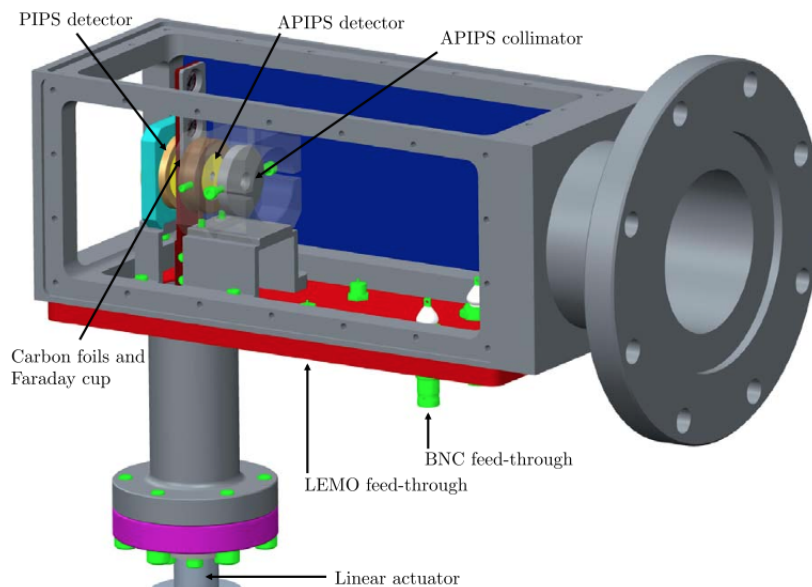
Figure 4.6: The 3-dimensional view of DSS2.0 [82].

in the opposite direction to the incident ion beams). The APIPS wafer has been protected by the collimator, which has a 4 mm central aperture so that the ion beam can pass through this aperture before being implanted into the C-foil. In addition, there is a holder to house the C-foil and Faraday cup (for the beam tuning purpose), which is attached to a linear actuator to change the implantation position [82]. The energy calibration of the detectors can be achieved by using ^{241}Am emitter or beams with known α-decay energies.

To measure the energy of the γ ray, three germanium detectors can be placed outside of the decay chamber. They can be positioned at any place around the implantation site except at the topside of the chamber where the baseplate is thicker. The small dimensions of the DSS2.0 enhance the γ-ray detection efficiency by increasing the solid angle as reported in [82].

In the odd-A polonium isotopes studies, three germanium detectors were used. They were placed at $90°$ in the direction of the incident ion beam. In addition, an MCP detector was installed (instead of the Faraday cup, see Fig. 4.6) on the linear actuator for the purpose of testing the beam transport off-line as well as tuning the beam on-line.

The remainder of this page was intentionally left blank.

Chapter 5

The Recent Setup of the ISOLTRAP and the Modifications

The main parts of ISOLTRAP are presented in Fig. 4.2. The sketch shows four main traps: the RFQ trap, MR-ToF MS, preparation Penning trap and the precision Penning trap. Besides these parts, there are two off-line ion sources to produce stable ions. They are used to calibrate the magnetic field strength in mass measurements. The first is an alkali ion source, which is placed (at a potential of 60 keV) before the RFQ trap and produces a continuous alkali ion beam such as ^{23}Na, ^{39,41}K, ^{85,87}Rb and ^{133}Cs by surface ionisation [23]. The second off-line source is laser ion source (LIS) [75], which is installed after the MR-ToF MS (perpendicular to the beam line, see Fig. 5.1) to produce carbon cluster ions. The carbon cluster ions are generated by using a high-intensity laser pulse from the laser system, which passes an entrance window into the vacuum chamber of ISOLTRAP and strikes a carbon sample (C-pellet) at the end of the ion source chamber. The extraction electrodes, that are shown in Fig. 5.1, are used to extract the ions. The ions are then focused by the einzel lens and guided by the steerer towards the quadruple deflectors, which are used to bend the ions beam by 90° and send them into the ISOLTRAP beam line [23].
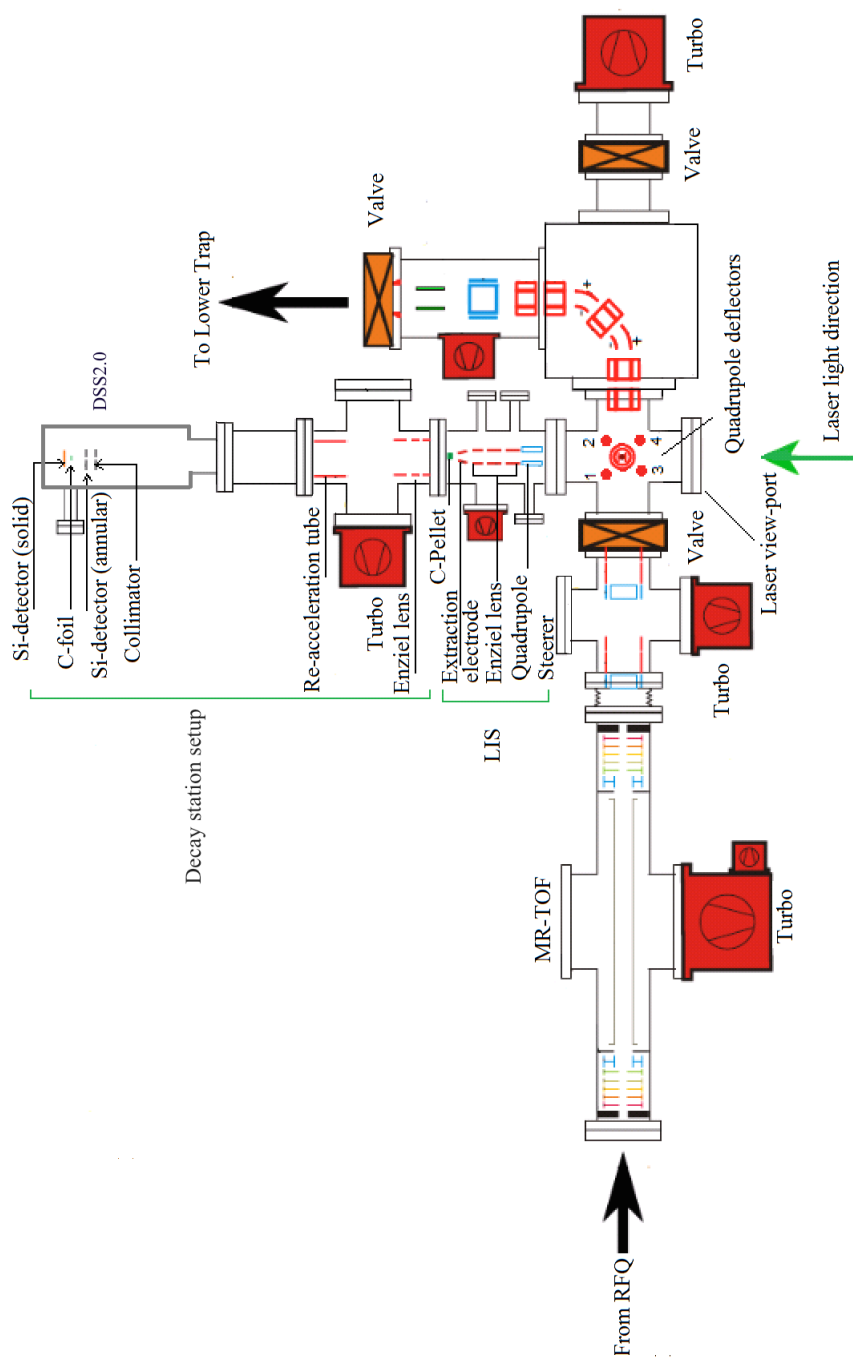
Figure 5.1: The required modification for the ISOLTRAP setup to perform the decay spectroscopy study on a pure sample delivered from MR-ToF MS.

To perform decay spectroscopy studies on a pure beam delivered from the MR-ToF MS, the DSS2.0 chamber was attached to the LIS behind the MR-ToF MS. The new installation of the DSS2.0 required some modifications to the beam-line at ISOLTRAP. The main one was the installation of the decay chamber and a 100-CF cross with one turbo pump, to maintain a good vacuum condition during the measurements. The 100-CF cross houses lenses and a re-acceleration tube, see Fig. 5.1. The lenses were used to focus the ions after passing the LIS section. The aim of the re-acceleration tube was to re-accelerate ions that have an energy of 3.2 keV after ejection from MR-ToF MS. This increasing in the energy could be necessary to ensure that the decay products cannot be diffused out of the C-foil when recoiling from α decays. The re-acceleration tube can be lifted from 0 kV to the maximum value of 10 kV. In fact, this potential is not enough in case of the odd-A polonium isotopes where the energy for the recoiling products is about 140 keV. Besides these modifications, the extraction electrodes and the C-pellet were removed from the LIS chamber. The ion optics of LIS were also used to optimize the transmission of the ion beam towards the DSS2.0.

According to these modification, two simulations were needed. The first was performed with the ion-trajectory program SIMION [83, 84], to optimize the transmission to the DSS2.0 chamber. The second simulation estimated the geometrical efficiency and the implantation depth, and it was made by using SRIM simulation,[85, 86]. Both simulations are presented in the following with the results that were obtained.

5.1   Ion transmission simulation with SIMION

The ion trajectories simulation was performed with the SIMION program. The program defines two kinds of points in a defined volume: electrode points (electrode geometries), which are defined by the electrode boundaries and non-electrode points [83]. The non-electrode points represent the space between the electrodes. The program numerically estimates the potentials at non-electrode points that

are created by the electrode geometries. The results of the numerical approximation of the potential in each point can be stored in a so-called potential array. In SIMION, this numerically process is called a refining. The refined potential array can be loaded into a workbench, where the ions can flow through the defined volume. Usually, the potentials on the electrodes are defined by the user and can be changed in the workbench [83].

To study the transport efficiency, the geometries of the DSS2.0 setup (includes DSS2.0, 100-CF cross, lenses and the re-acceleration tube) were generated, defined in the potential array, and then loaded into the workbench. The LIS geometries that created by Frank Wienholtz[1] were also included in the simulation. The ion bunch in this simulation was defined using the exiting file which was generated based on the ejection conditions from the MR-ToF MS.

Fig. 5.2 shows the geometries and ions trajectory simulations, which correspond to the decay station setup in Fig. 5.1. As shown in Fig. 5.2 ions need first to be focused by the lens 1 and 2, then bent 90° by quadrupole deflector, and focused again using the LIS ion optics and electrode 14.

The simulation aims to find optimum voltages that maximize the ions transmission. This was achieved by using a program which uses the Lua programming language. Note that, the optimization process with Lua program takes very long time, to find the optimal values, since each applied voltage (we have 15 voltages) should be scanned individually with respect to the others. Thus, it was decided to fix the voltages at the quadrupole deflector electrodes to the values that are displayed in the Table 5.1. In addition, the electrodes 9, 11 and 13 were fixed at 0 kV. The results are shown in the Table 5.1. The voltages were classified into two sets V1 and V2. Set V1 were obtained when the potential at the re-acceleration tube was switched to 0 kV. For set V2, the Lua program was used to rise the potential at the re-acceleration tube potential from $0 - 10$ kV. By considering a collimator of central hole 4 mm the transport efficiency can be optimized to at

---

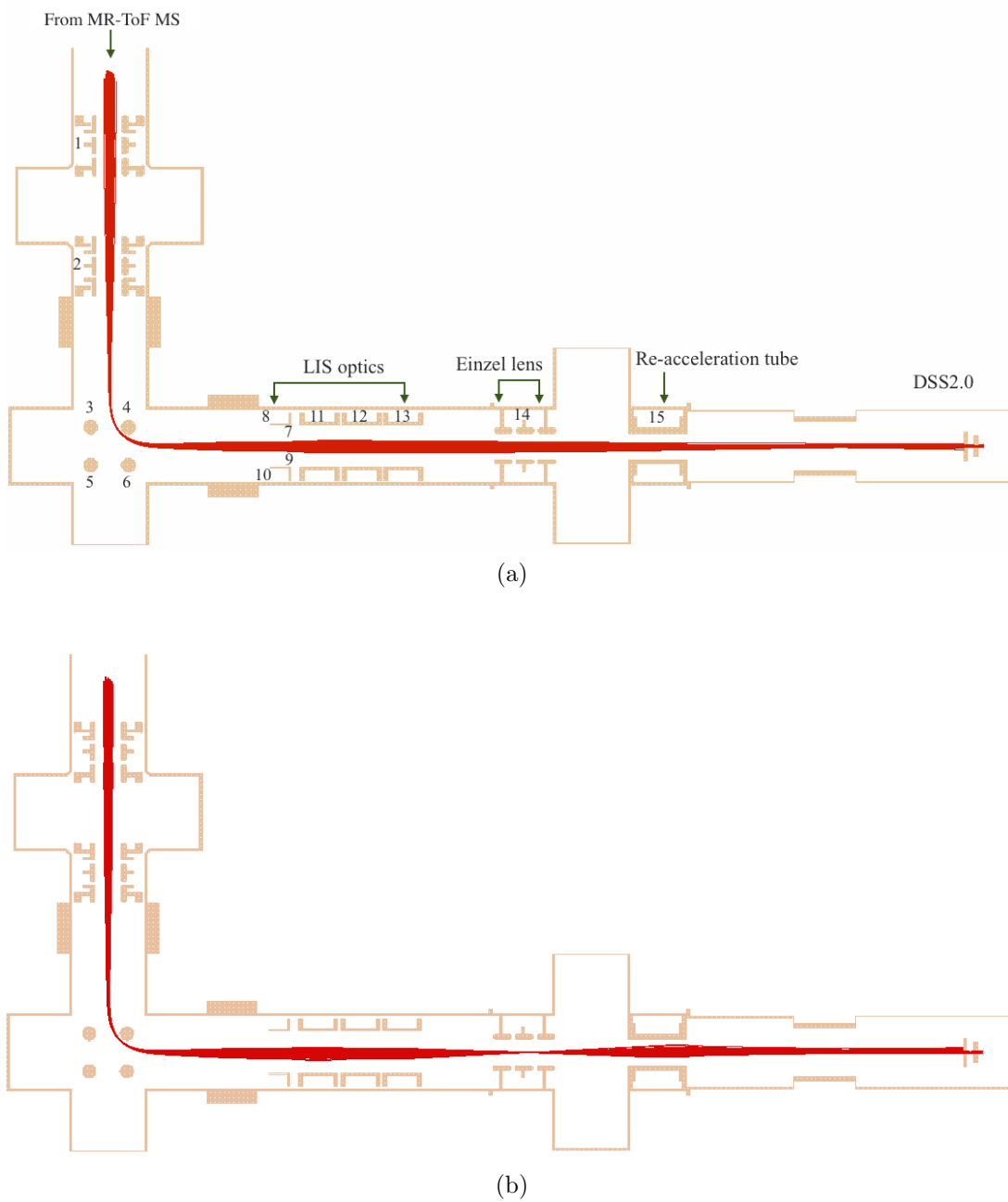[1]PhD student at Ernst-Moritz-Arndt University in Germany.

(a)

(b)

Figure 5.2: The simulation of ion trajectories with using SIMION: (a) is obtained with applying set V1 voltages and (b) is obtained with applying set V2 voltages.

least 90% for V1 and V2. The untransmitted ions to the C-foil were lost in the collimator, which has a radius smaller than the radius of the ion bunch.

Table 5.1: The optimum voltages that were obtained from SIMION simulations. The values are given in volts.

Electrode	V1	V2
1	-2400	-2200
2	+1000	+900
3	+3000	+3000
4	−2000	−2000
5	+2800	+2800
6	+3000	+3000
7, 8 and 10	-6000	-6000
9, 11 and 13	0	0
12	+480	−6000
14	−2000	-600
15	0	+10000

5.2 Preparing of ion optics

Based on the ion trajectory simulations of the decay setup DSS2.0, the ion optics (einzel lenses and the re-acceleration tube) were designed. The idea was to have two separate pieces: the lenses and the tube. They were designed to be fit inside the 100-CF cross and keeping the centre of the 100-CF cross free. The lenses and the re-acceleration tube are coupled to a holder which provides an easy alignment for them inside the 100-CF cross. The ion optics were ordered by the University of Manchester. The manufacture process followed by assembling the elements and set them up in the final position inside the 100-CF cross. The final design of new pieces can be seen in the Fig. 5.3.
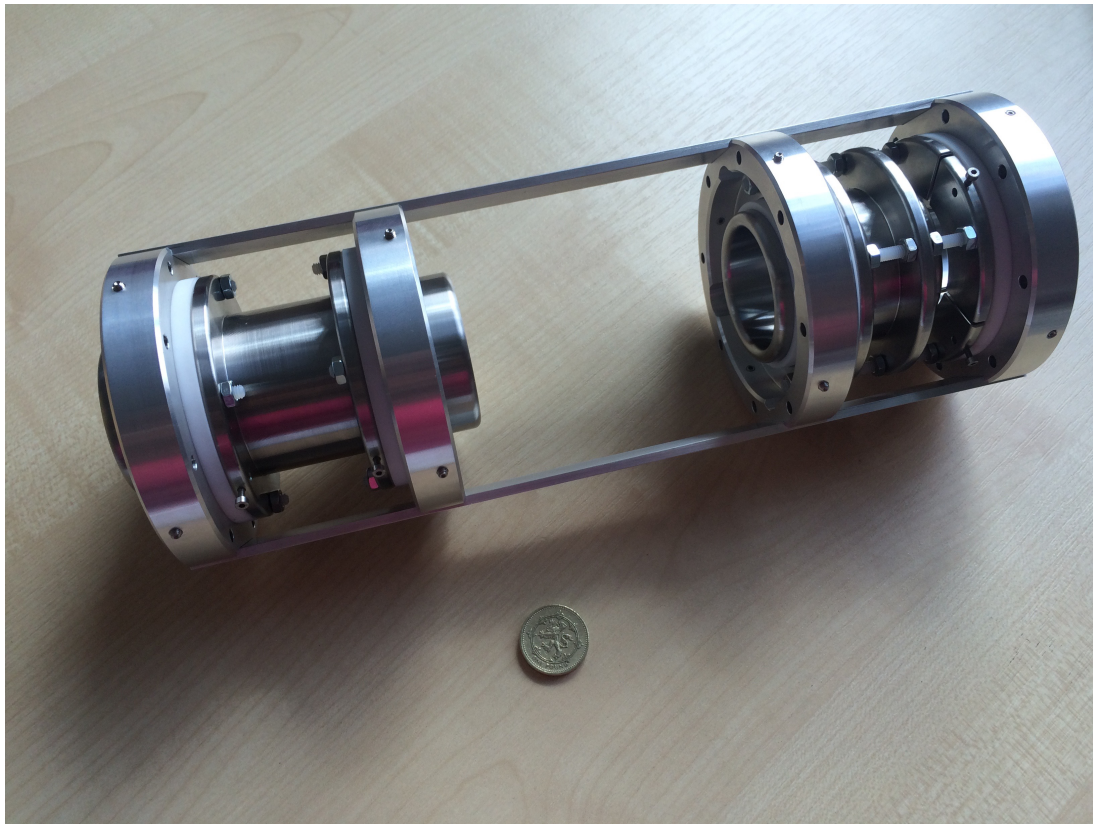
Figure 5.3: The lens units which was used to focus the beam to the DSS2.0.
For details read the text. British pound coin is shown alongside for scale.

5.3   Estimation of the geometrical efficiency using SRIM

The implanted polonium isotopes in the C-foil will decay and produce energetic α particles, with an energy ranging from $6 - 7$ MeV, and a recoil daughter nucleus, with a fraction of the α energy ($T_D = \frac{4}{A_D}T_\alpha$). Both decay products will interact with the carbon atoms, lose some of their energy, and then change their directions. The energy loss depends on the energy of the decay product; the less energetic the particle is, the more the energy loss is [85, 86]. Consequently, a little of the α-particle energy will be lost in the C-foil before reaching the silicon detectors. The recoiling nuclei, however, have energies of ~ 140 keV, which is more than the energy of the implanted ions that may have a maximum energy of 13 keV. In this case, there is a possibility for some of the recoil nucleus to exit the C-foil, which causes recoil loss. In this section, the Stopping and Range of Ions in Matter

(SRIM) program [85, 86] was used to study the decay products trajectories in the C-foil and determine the depth of the implanted ions [86].

SRIM is a Monte-Carlo program based on theoretical calculations of the interaction between the charged particles and the medium atoms [85, 86]. In SRIM program, there is a subset program known as Transport of Ion in Matter (TRIM). Users can use the Graphical User Interface (GUI) window of the TRIM program to setup the initial conditions by specifying the ion, energy, angles of incident ions, with respect to the target layer surface, and the element that is used in the material target. TRIM provides a wide range of predictions such as the energy loss, direction and position of any ion exiting from the target. The program also utilizes a data file (TRIM.dat) as an input in case that the calculations are more complex. Typically, the results of the calculations alongside the initial information are available in the output files, see Appendix A. The user can create TRIM.dat file that includes specific information about the ion i.e., energy, position, and direction. These data can be used later as initial predictions.

Generally, the definition of the absolute α detection efficiency is given by [88, 89]:

$$\epsilon_{abs} = \frac{N_{sp}}{N_s}, \tag{5.1}$$

where N_{sp} is the total number of α counts in the spectrum and N_s is the number of α particles emitted by the source with energy E. The quantity ϵ_{abs} depends on the geometric efficiency as well as on the intrinsic efficiency of the silicon detector [88, 89]. The geometric efficiency detection is defined as $\epsilon_G = \Omega/4\pi$, which represents the ratio between the number of α particles emitted towards the detector and the number that are emitted away from the C-foil.

The TRIM simulation was performed firstly to determine the ^{195}Po depth distributions in the C-foil, which has a width of 888 Å. The results of the implantation depth distributions at 3 and 13 keV are shown in Fig. 5.4. The simulation shows that the maximum depth in the carbon layer for a 13 keV ^{195}Po is twice as much as a 3 keV ^{195}Po, see Table 5.2 for comparison.
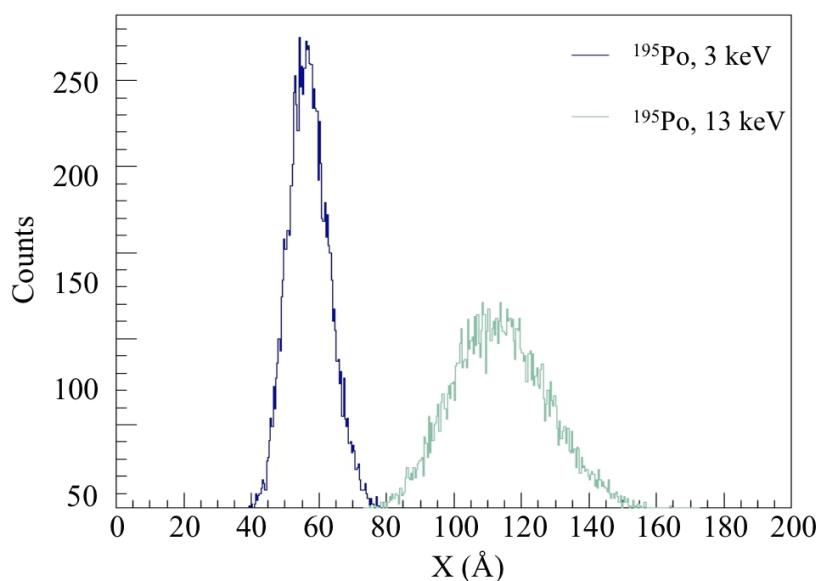
Figure 5.4: The implantation depth of ^{195}Po at 3 and 13 keV. The calculations are performed by using TRIM simulations.

Table 5.2: The maximum depth and full width at half maximum (FWHM) of 3 keV and 13 keV ^{195}Po.

Energy (keV)	Depth (Å)	FWHM (Å)	counts
3	57(1)	15(1)	9983(117)
13	113(2)	34(3)	9942(122)

The trajectories of the decay products can be simulated based on the implantation depth of the parent nucleus. The distribution of the implantation depth obtained from TRIM calculations was used as start positions for the reaction products. The emission directions were uniformly generated and specified by the three directional cosines that have been chosen randomly in the range $[-1, 1]$. Afterwards, the positions, directions and particle energy were included in TRIM.dat file. By using the TRIM.dat file as an input file, the trajectories of the α particles and the daughter were extrapolated.

The geometrical angle from the source to the active detector surface was considered as it determines the number of the αs that leave the C-foil and travel

a distance of 3.5 mm (4 mm) in the vacuum towards the PIPS (APIPS) detector. The overall geometrical efficiency was found to be about 40% for the PIPS (solid) detector and 23% for the APIPS (annular) one. The reduced efficiency in the annular detector refers to the backscattered αs through the 4mm hole of the silicon detector. These results are consistent with previous estimates for the CRIS DSS2.0 [82].

Similarly, the program was used to track the daughter nuclei (^{191}Pb) inside the C-foil. The SRIM results show that in case of 3 keV Po around 60% of the daughter ions are stopped in the C-foil. The high recoil energy of the daughter ions after α decay causes recoil losses, which represent 40% of the daughter ions. The 40% of the daughter ions are fully backscattered, and no transmitted ions out of the C-foil have been found in the SRIM results. The stopped fraction is increased by $\sim 10\%$ if the Po beam was accelerated up to 13 keV before the implantation. In both energies the α particles come out from Pb decay can be detected in the silicon detectors.

Furthermore, α-energy spectra were predicted at different depth distributions of the parent nucleus. Fig. 5.5 displays the simulated energy spectra of α particles after ^{195,197}Po decay at 3 keV. The main feature that can be observed is the asymmetrical shape of the α peak. It is more pronounced in the spectra of the transmitted αs, as shown in Fig. 5.5(a). Usually, the α spectrum has a Gaussian shape from both sides. The long tail at the left side (low-energy tailing) results from the energy loss of the α particles during their passage through the C-foil toward the solid detector. Thus, the peak from the low-energy side can not be describe by the Gaussian tail, which is steeply sloped. The high-energy side will remain as the Gaussian shape unless energy summing of α-electron coincidences occur [90]. Consequently, a simple Gaussian function can not be used to fit α spectra with the low-energy tailing. In this work, α peaks were fitted with a Crystal Ball (CB) function [91–93], which consists of power-law and Gaussian functions. The power-law function is used to fit the tail, while the Gaussian distribution is used to model the peak shape. More details about the fitting procedure will be present in the next chapter.

(a)

(b)
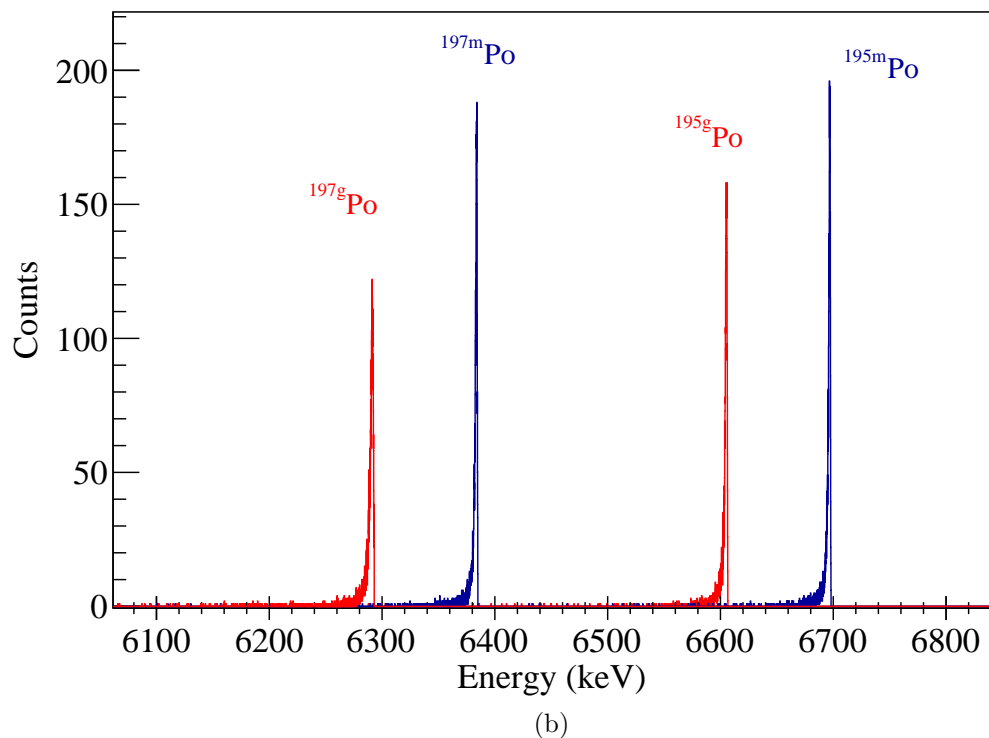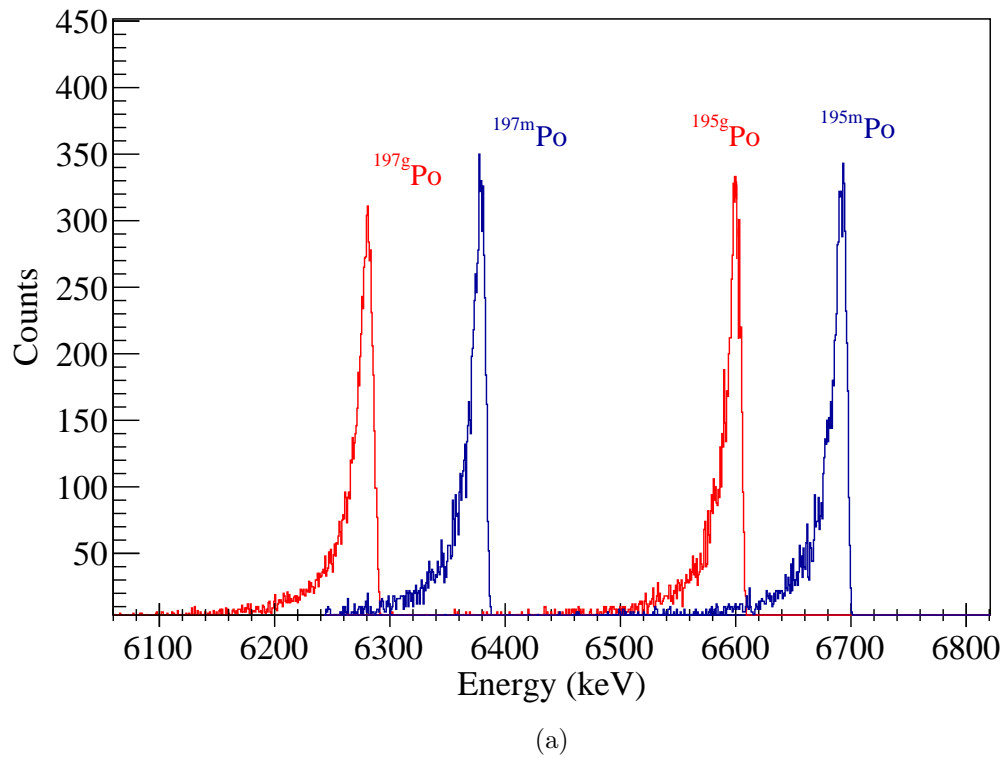
Figure 5.5: The simulated α-energy spectrum after the decay of the Po isotopes. (a) and (b) represent the transmitted and backscattered α particles, respectively, at 3 keV. The panel (a) is the simulated α spectra in PIPS detector, while the panel (b) is the simulated α spectra in APIPS detector.

The remainder of this page was intentionally left blank.

Chapter 6

Mass measurements results

In August 2015, ISOLTRAP performed mass measurements on the radioactive isotopes of polonium. The experiment measured the excitation energy of the $13/2^+$ state in ^{195,197}Po. This chapter will describe the experimental procedure and the data analysis. The experimental results of the polonium isotopes presented in this chapter were taken from my published work in Ref. [68].

6.1 Experimental procedure

The polonium isotopes were produced at ISOLDE facility at CERN [28]. A thick uranium carbide (UC_x) target was bombarded by beams of protons (1.4 GeV), delivered from the CERN PSB. The radioactive polonium products then diffused in the target and effused towards a hot cavity (2000 ^{o}C), and were selectively ionised using the RILIS method [25, 27]. By tuning the laser light to a specific frequency, an enhancement of one isomer over another was possible in polonium isotopes. However, it is difficult to produce completely isomerically pure beams due to the overlapping hyperfine structure of the polonium isotopes [31, 32, 90]. Figure 6.1 shows the hyperfine structure of the low- and high-spin in ^{195,197}Po. The ion beam was extracted from the ion source and then accelerated with an energy of 30 keV to HRS to be separated according to the mass-to-charge ratio.
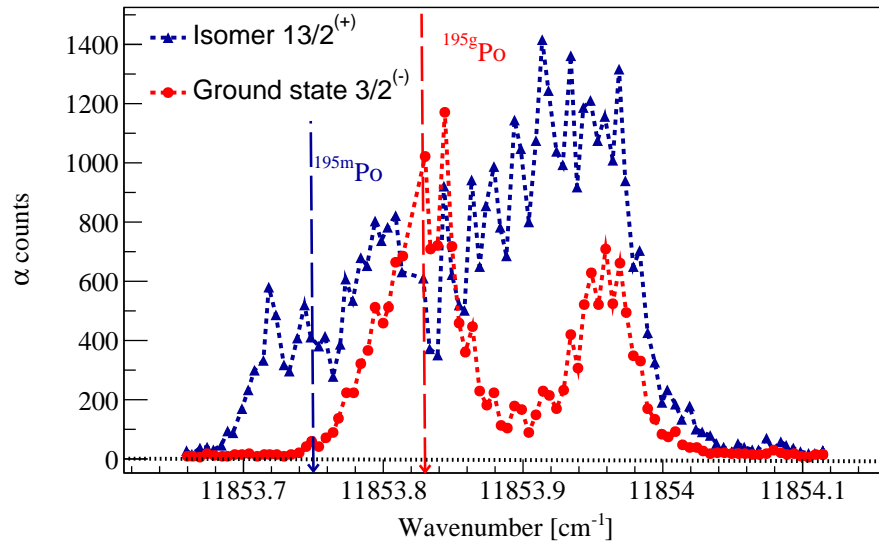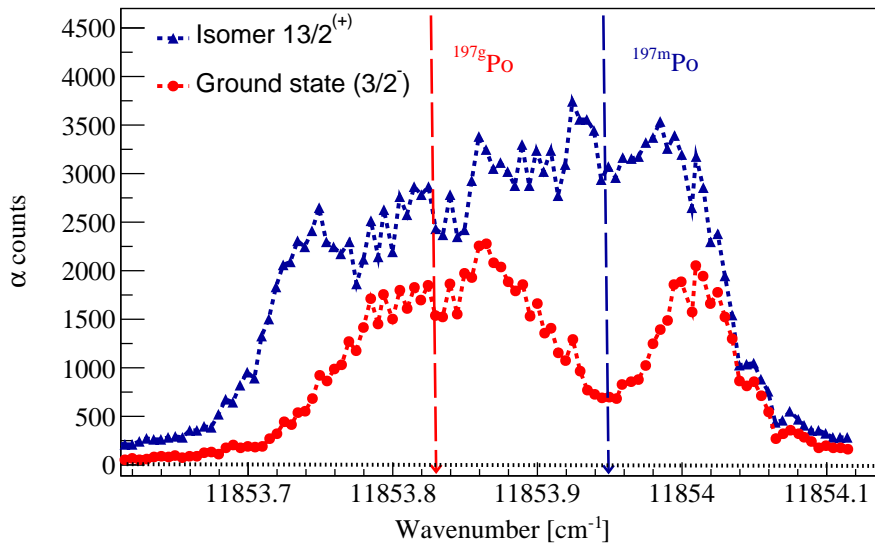
Figure 6.1: The hyperfine structure of the $3/2^-$ and $13/2^+$ states in (a) ^{195}Po and (b) ^{197}Po [31, 32, 90]. The dashed lines denote the wavenumbers that were used for the mass measurements. Note that the hyperfine spectra of both states in ^{195}Po and ^{197}Po were recorded in anther experiment, thus the laser resolution is different in the this work. This figure is taken from Ref. [68].

Afterwards, the beam was guided to the ISOLTRAP experiment where decay and mass measurements were performed.

The 30 keV ion beam from ISOLDE was captured, cooled and bunched for 10 ms
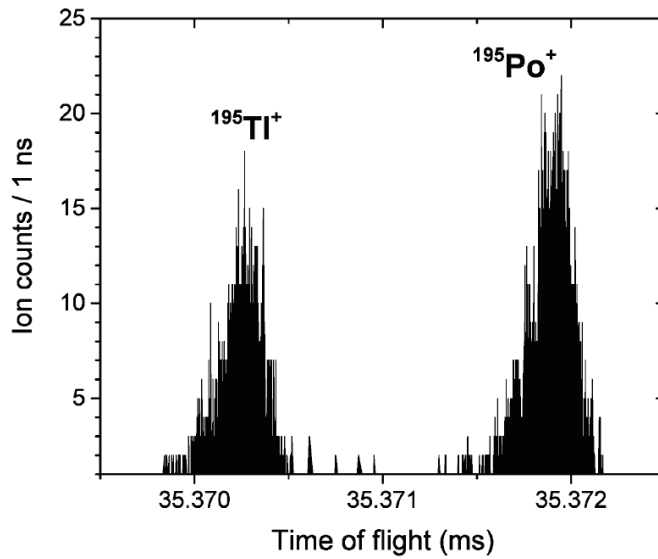
(a)
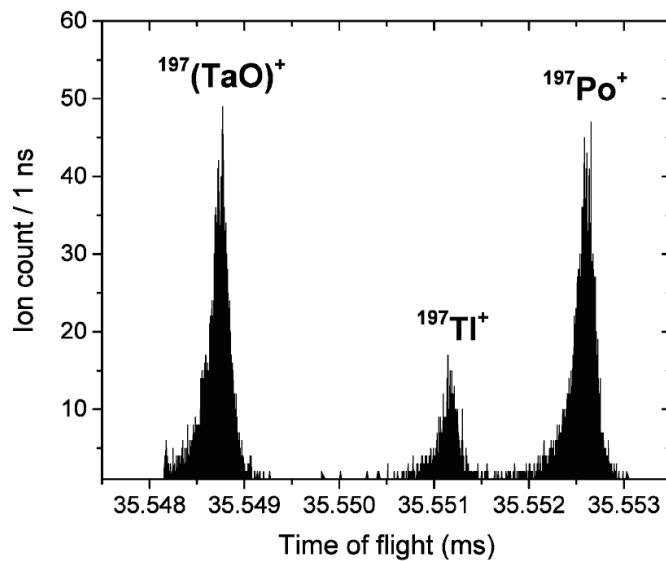
(b)

Figure 6.2: The MR-ToF mass spectrum for (a) ^{195}Po and (b) ^{197}Po, with surface-ionised contamination. The isobaric purification was achieved with trapping times of 35.37 and 35.6 ms, respectively.

in a gas filled RFQ trap [67]. Since the ionisation process took place in a high-temperature cavity, the polonium beam contained isobaric contamination, resulting from surface ionisation. To separate the beam from those isobars, the polonium bunches were ejected from the RFQ trap and transferred to the MR-ToF

MS. The resolving power of the MR-ToF MS ($R = 10^5$ after 30 ms) is sufficient to separate the Po isotopes from Tl isotopes, which requires a resolving power of $\approx 10^4$. An example of the MR-ToF mass spectrum is shown in Fig. 6.2 for ^{195,197}Po with surface-ionised contamination. The isobaric purification of ^{195,197}Po was achieved with trapping times of 35.37 and 35.6 ms, respectively [29, 71].

The pure polonium samples were then ejected from the MR-ToF MS [94] and delivered to either the DSS2.0 chamber [82] or the Penning traps. To identify the nuclear state of the isotopes under investigation prior to the mass measurements, the ion bunches were deflected 90° to the DSS2.0, using an electrostatic quadrupole bender, see Fig. 5.1. The polonium ions were implanted into the C-foil (90-nm thick) where the energy of the α particles emitted from the decay of the polonium isotopes was identified by the silicon detectors that surrounded the C-foil. The solid angle coverage of the silicon detectors was 64% as was obtained from SRIM calculations in the previous chapter.

Following the identification of the individual states, the ions were delivered from the MR-ToF MS to the Penning traps. In the preparation Penning trap, a further purification process was applied via the mass-selective resonant buffer-gas cooling technique [55]. Afterwards, the ion bunch was injected into the precision Penning trap where the mass was measured by using the ToF-ICR technique [95], see Section 3.4. By measuring the cyclotron frequency of the ion, one can extract its charge-to-mass ratio mass q/m from its cyclotron frequency according to Eq. (4.2.5).

6.2 Alpha spectra fitting

Alpha-peak shape information was necessary for analysing the mass-spectrometry data. It helped to compare the ground/isomer ratio observed in the α spectra with the ones resulting from the double resonances in mass measurements. As mentioned before, one cannot use a simple Gaussian function to fit the peak shape in the α spectrum, which generally has an asymmetric tail in the left side. The
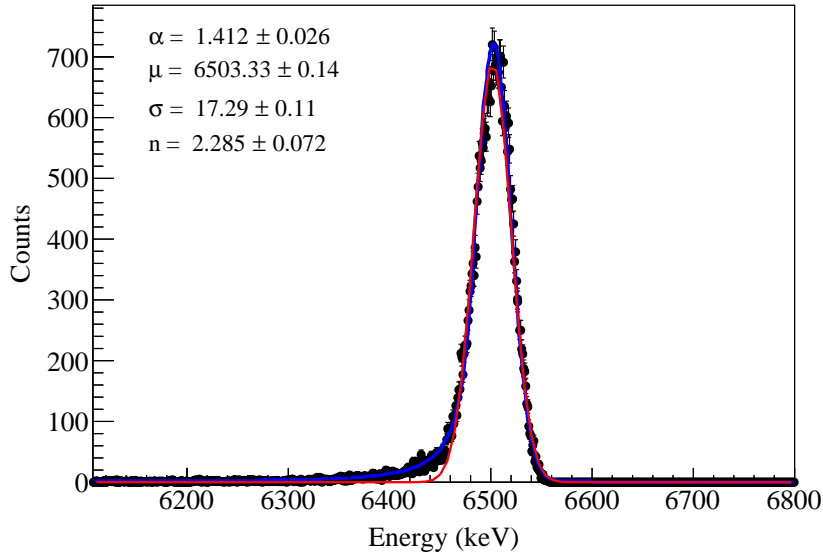
Figure 6.3: The α spectrum of ^{196}Po. For comparison, the spectrum was fitted with CB (blue) and Gaussian (red) functions. The CB fit gives a good description for the tail on the spectrum unlike Gaussian fit which falls steeply.

CB function would be the best choice to fit a spectrum with a side tail. Therefore, the α spectroscopy of ^{196}Po was performed as it has a single α-decaying. The spectrum of ^{196}Po was then fitted with the CB function to extract the parameters of the signal shape. The CB function is a function that is used to model the energy loss by replacing one of the two Gaussian tails by the power-law function [91–93]:

$$
CB(E; \alpha, \mathrm{n}, \mu, \sigma) \sim \begin{cases} \exp - \frac{1}{2}\left(\frac{E-\mu}{\sigma}\right)^2 & \text{for } E > (\mu - \alpha\sigma), \\ \left(\frac{n}{|\alpha|}\right)^n \exp\left(\frac{-\alpha^2}{2}\right) & \text{for } E \leq (\mu - \alpha\sigma). \end{cases}
$$

μ and σ (α and n) are Gaussian (power-law) parameters. The Gaussian function is used to fit events in the range above the energy value $E = \mu - \alpha\sigma$, while the power-law function fits the events that are contributed to the tail (i.e., below the value $E = \mu - \alpha\sigma$), see Fig. 6.3.

The shape parameters that were derived from the fit of ^{196}Po are shown in Fig. 6.3. These parameters were used to analyse other α spectra that were measured during the experiment. The parameters; σ, α and n were fixed during the fitting

procedure, except the parameter μ which represents the position of the peak. In doing so, the accurate isomeric-to-ground state ratio was determined in spectra with overlapping peaks.

6.3 Results

During the polonium experiment, two types of measurements were performed. First measurements were α-decay measurements. The polonium isotopes were ionised with RILIS and then delivered to the decay spectroscopy station to determine the ratio of isomeric-to-ground state from the α-decay spectra. The second measurements were the mass measurements. The ToF-ICR resonances were recorded for each state or both states together. The combination between these measurements allowed mass determination of the investigated states.

6.3.1 ^{195}Po

In the measurements of ^{195}Po, it was possible to enhance the production of either nuclear states by selective ionisation with the RILIS laser. The $13/2^+$ high-spin state with a half-life of 2 s, was selected by tuning the laser to the wavenumber 11853.75 cm^{-1}, where at this wavenumber the ionisation of the $13/2^+$ state is dominant, see Fig. 6.1(a). The ratio of the $13/2^+$ state was extracted from the α spectrum to be $R_m = 94(2)\%$ as illustrated in Fig. 6.4(a). Therefore, three quasi-pure ToF-ICR spectra were taken with excitation times of up to 2 s. The ^{195m}Po ToF-ICR spectrum is shown in Fig. 6.5.

In case of the $3/2^-$ low-spin state with $t_{1/2}$=4.64 s, the highest count corresponds to the wavenumber 11853.83 cm^{-1}. This laser setting gave a mixture of the two states of ^{195}Po leading to $R_g = 56(1)\%$ ground state, as deduced from the α spectrum in Fig. 6.4(b). Thus, the difference in the half-life between the two states was exploited, to change the ratio between them. In addition to the RILIS laser configuration, the ions were trapped in the lower-trap (preparation Penning
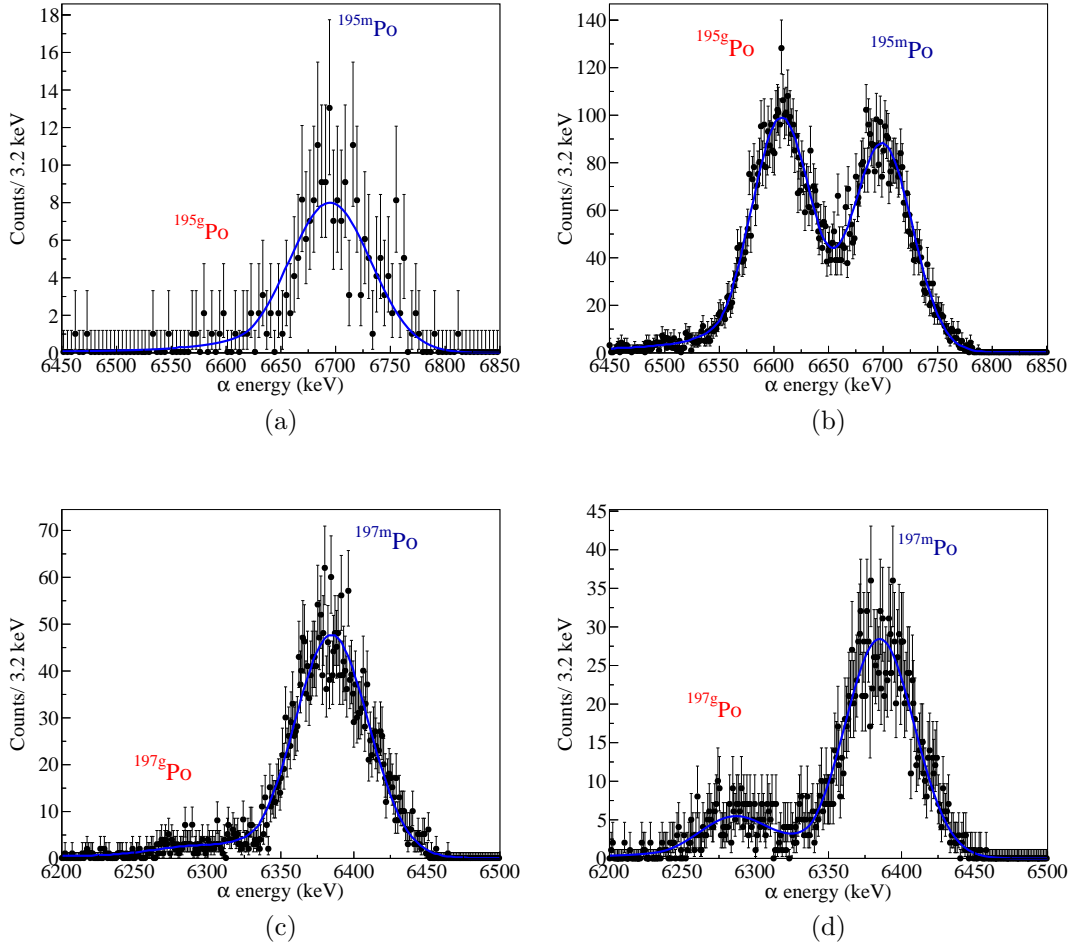
Figure 6.4: The α spectra for ^{195}Po, (a) and (b), and ^{197}Po, (c) and (d). They were recorded at different RILIS wavenumbers: (a) at 11853.75 cm^{-1} and (c) at 11853.95 cm^{-1}, while (b) and (d) at 11853.83 cm^{-1}. This figure is taken from Ref. [68].

trap) for more than 2 s and then ejected to the upper-trap (precision Penning trap) for precise mass measurement. In this way, the ratio of the $3/2^-$ state was enhanced to be 75-85 %, and thus three ToF-ICR spectra were taken with excitation times up to 2 s in the upper-trap, see Fig. 6.5. The weighted-average value $\bar{r}$ is shown in Table 6.1 for each state.

6.3.2 ^{197}Po

For the longer-lived ^{197}Po ($t_{1/2}$=32 s), it was possible to obtain pure high-spin ToF-ICR spectra, with excitation times of 3 s, by tuning the RILIS laser to a
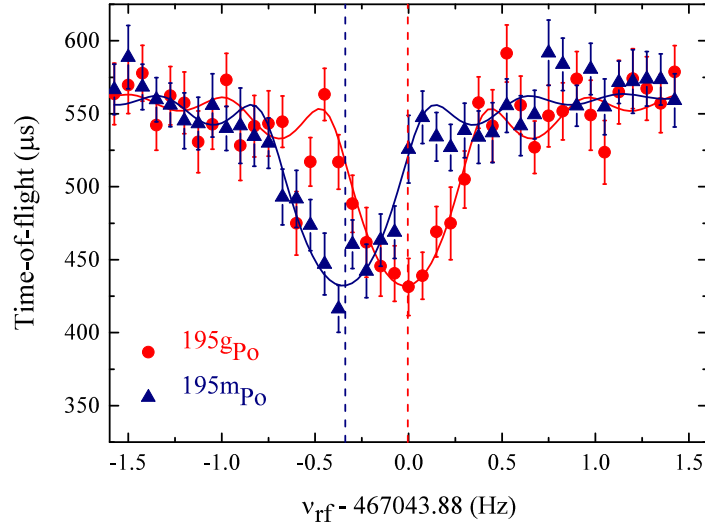
Figure 6.5: ToF-ICR resonances of $^{195(g,m)}$Po with $T_q=2$ s. Blue triangles (red circles) represent the isomeric (ground) state. The blue (red) dashed line denotes the centroid frequency of the isomeric (ground) state. Pure samples of either state were determined thanks to the isomer selectivity offered by RILIS and the difference in the half-lives (see text for details). The solid lines represent the fit of the theoretical line shape [57] to the experimental data. This figure is taken from Ref. [68].

wavenumber of 11853.95 cm^{-1}, see Fig. 6.1(b). With this laser setting, no evidence for the low-spin in the α spectrum is seen, as shown in Fig. 6.4(c). The low count rate of the ground state refers to the ionisation scheme that was used in this experiment. At this mass number, an additional contamination from ^{181}Ta^{16}O was also present in the beam. Thus, an alternative ionisation scheme was investigated to obtain the optimal one. This resulted in less production of the ground state than in previous studies [31, 32, 90].

On the contrary, the hyperfine structure of the low-spin state shows an overlap with the high-spin state as illustrated in Fig. 6.1(b). The high-spin state is also present in the α spectrum of Fig. 6.4(d). By using the RILIS wavenumber 11853.83 cm^{-1}, the beam intensity for the $3/2^-$ state was $R_g = 25(1)\%$ as obtained from the α-decay measurements. With a quadrupole excitation time of 5 s, fully-resolved resonances of the isomer and ground states were obtained, see Fig. 6.6. In fact, the simultaneously trapped ground- and isomeric-state ions could shift the cyclotron frequency centre [95]. In order to check if there is any
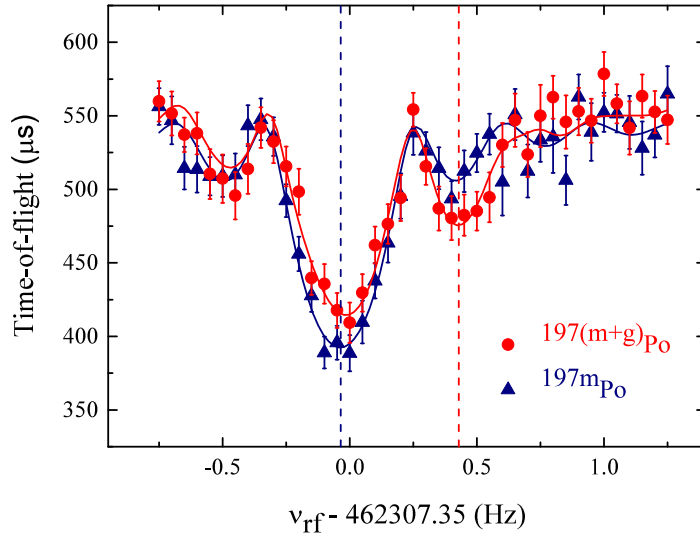
Figure 6.6: ToF-ICR resonances of $^{197(g,m)}$Po. The low-spin ToF- ICR resonance was taken with T_q= 5 s, while the high-spin with T_q=3 s. The ToF-ICR spectrum, with red circles, includes two resolved resonances; isomeric (left) and ground (right) states. The blue triangle ToF-ICR spectrum represents the pure isomeric state. The blue (red) dashed line represents the centroid frequency of the isomeric (ground) state. The solid lines are fits of the experimental data to the theoretical line shape [57]. This figure is taken from Ref. [68].

resulting shift, the frequency was determined for different numbers of ions that were present in the precision trap for one cycle. No significant change in the frequency centre was observed when considering only one ion per cycle. Therefore, the number of detected ions was limited to 2 ions in each measurement cycle to allow sufficient counts for a reliable fitting [95]. For each state, weighted-average value $\bar{r}$ is presented in Table 6.1.

6.3.3   Analysing mixed resonances

The most important sources of the uncertainty associated with the mass measurements are the drift of the magnetic field and the mass-dependent effect [75]. This is further discussed in Section 4.2.5. Another possible systematic error (originating from the presence of a small fraction of ground/isomeric state in the $^{195(g,m),197m}$Po measurements, that were fitted as single-resonances) was investigated. Therefore, each questionable file was investigated individually. The
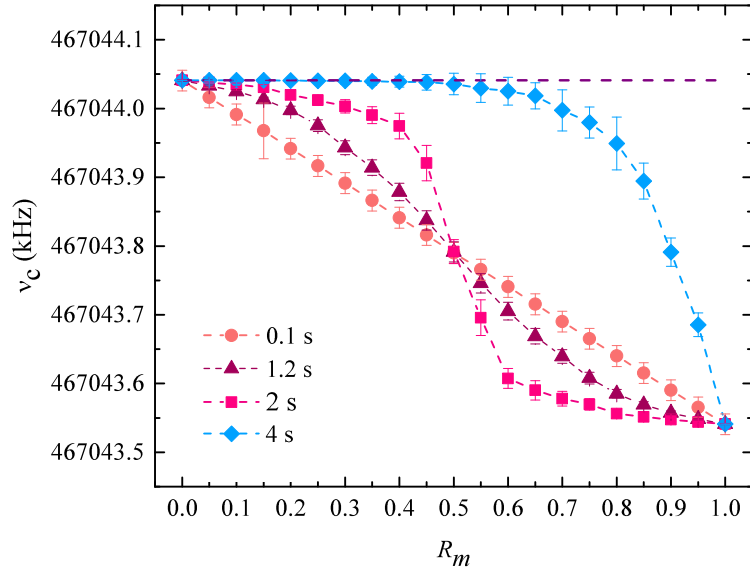
Figure 6.7: The centre cyclotron-frequency ν_c of ^{195g}Po for different excitation times, as a function of the isomeric state ratio R_m. It was obtained by fitting a mixed resonance with a single-resonance curve. The purple dashed straight line denotes the centre cyclotron-frequency of $3/2^-$ state. When two resonances are clearly identified (for longer excitation times), the resonance of interest is systematically selected. See text for details. This figure is taken from Ref. [68].

Table 6.1: Weighted-average values $\bar{r}$ of the polonium isotopes alongside the corresponding mass excess values (ME). The ratios were obtained with respect to ^{133}Cs$^+$ [96, 97]. AME16 values were taken from [96, 97]. # denotes systematic.

Isotopes	I^π	$\bar{r}$	ME (keV)	AME16 (keV)
^{195g}Po	$3/2^{(-)}$	1.4671205566(495)	$-11117.9(61)$	$-11060(40)$
^{195m}Po	$13/2^{(+)}$	1.4671217650(584)	$-10968.3(72)$	$-10965(28)$ #
^{196g}Po	0^+	1.4746257515(477)	$-13467.9(59)$	$-13473(14)$
^{197g}Po	$(3/2^-)$	1.4821505060(804)	$-13396.4(100)$	$-13360(50)$
^{197m}Po	$13/2^{(+)}$	1.4821521160(523)	$-13197(7)$	$-13130(90)$ #
^{199m}Po	$(13/2^+)$	1.4971864768(395)	$-14929.4(49)$	$-14897(18)$
^{203g}Po	$5/2^-$	1.5272639530(453)	$-17310.3(56)$	$-17311(9)$
^{208g}Po	0^+	1.5648835996(448)	$-17469.5(55)$	$-17469.6(17)$

investigated file was first fitted as a pure single-resonance with a least-squares fit from which the optimum-fit parameters were extracted. These parameters

were used to produce a pure resonance in the correct frequency range and with the representative parameters. A second resonance was then produced, with the same parameters but being an admixture of the isomeric and ground resonances with the respective ratio obtained by the α-decay measurements. The resulting resonance was then also evaluated using a single-resonance fit. The difference between the two fits was added in quadrature to the systematic uncertainties.

The evaluation of systematic uncertainties is shown in Fig. 6.7. The fitted ground-state frequency was systematic shifted towards the isomeric frequency when the ratio of the isomeric state varied from 0 (no isomeric state is present) to 1 (purely isomeric state). In case of 0.1 s excitation, one would expect a linear shift of the ground-state frequency towards the low frequency since the two resonances are not fully resolved. With 1.2 and 2 seconds, the resonances are still not completely resolved and therefore a symmetric pattern of the frequency shift around R_m=50% is observed. The long excitation time 4 s shows a smooth behaviour, starting with a pure ground state until the centre frequency slowly drifts towards the isomeric state. The behaviour of the frequency shift depends on the frequency difference between the two states. For example in ^{195}Po, where the difference between the low and high states is only about 0.32 Hz, it is likely to have two partially overlapping resonances even with 4 s excitation time, since the peak width is around 0.25. Thus a jump to the isomeric state is expected around 50%.

The frequency ratio in this work determined with respect to ^{133}Cs$^+$. The weighted average of the cyclotron-frequency ratios of the polonium isotopes and their mass excess (ME) are presented in Table 6.1. The precise ME values of ^{195g}Po and ^{197g}Po agree with AME2016 values [96, 97], within 2σ and 1σ, respectively. Note that the masses of the ^{195m,197,m}Po were obtained for the first time experimentally through this work and agreed with AME2016 values that are estimated from systematic studies.
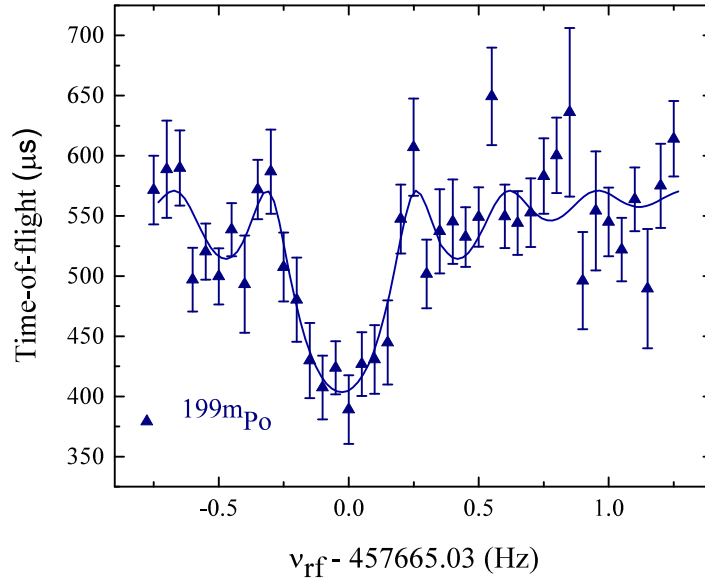
Figure 6.8: The ToF-ICR resonance of ^{199m}Po recorded with 3 s excitation. The solid line is the fit of the experimental data to the theoretical line shape [57].

6.3.4 ^{199m}Po

For the mass measurements of ^{199}Po, the RILIS laser was set in the broadband mode in order to produce a balanced ratio between the two investigated states ($13/2^+$ and $3/2^-$ states). The α-decay measurements with this setting leads to $R_m = 96(1)\%$, in favor of the $13/2^+$ state. Therefore, it was difficult to obtain a favorable ratio for the $3/2^-$ state. However, when the laser wavenumber tuned at 11854.02 cm^{-1}, the beam content was enhanced to be $R_m = 99.1(3)\%$, with high purity for the $13/2^+$ state. The mass of this state was determined from four ToF-ICR measurements with excitation times of 3 s. The ^{199m}Po ToF-ICR resonance is shown in Fig. 6.8. Table 6.1 shows the weighted-average value $\bar{r}$ alongside ME value of ^{199m}Po, which is in agreement with AME2016 value.

6.3.5 ^{196,203,208}Po

The masses of ^{196,203,208}Po were also measured by using the precision Penning trap. Two ToF-ICR resonances were determined for ^{196}Po and three for ^{203,208}Po, with

an excitation time of 1.2 s. Table 6.1 presents the weighted-average values $\bar{r}$ for these isotopes with the corresponding ME values. The ME values of ^{196,203,208}Po in a good agreement with the AME2016 values, agreeing within 1σ [96, 97].

Table 6.2: Excitation energies of isomeric states in odd-A polonium isotopes as well as other isotopes linked by α-decay chains [68].

Isotopes	I^{π}	E^* (keV)
^{205}Ra	$13/2^{(+)}$	278(31)
^{203}Ra	$13/2^{(+)}$	246(17)
^{201}Rn	$13/2^{(+)}$	248(12)
^{199}Rn	$13/2^{(+)}$	222(13)
^{197}Po	$13/2^{(+)}$	199(11)
^{195}Po	$13/2^{(+)}$	150(10)
^{193}Pb	$13/2^{(+)}$	95(28)
^{191}Pb	$13/2^{(+)}$	55(12)

6.4   Discussion

In this work, the α-decay measurements assisted the mass measurements by providing an accurate ground-to-isomeric state ratio for a given RILIS wavenumber setting. The obtained ratio was used to identify the spin of the nuclear state that was present in the ToF-ICR spectrum. Moreover, it was possible to determine the state ordering when two resolved resonances were observed in ToF-ICR spectra. According to Eq. (3.2), the state with a lower cyclotron frequency corresponds to the state with higher mass (excited state) and conversely, the one with a higher cyclotron frequency corresponds to the lighter mass (ground state). The results obtained from both measurements (α-decay spectroscopy and mass measurements) show that the state with the spin $13/2^+$ is the excited state in ^{195}Po and ^{197}Po.
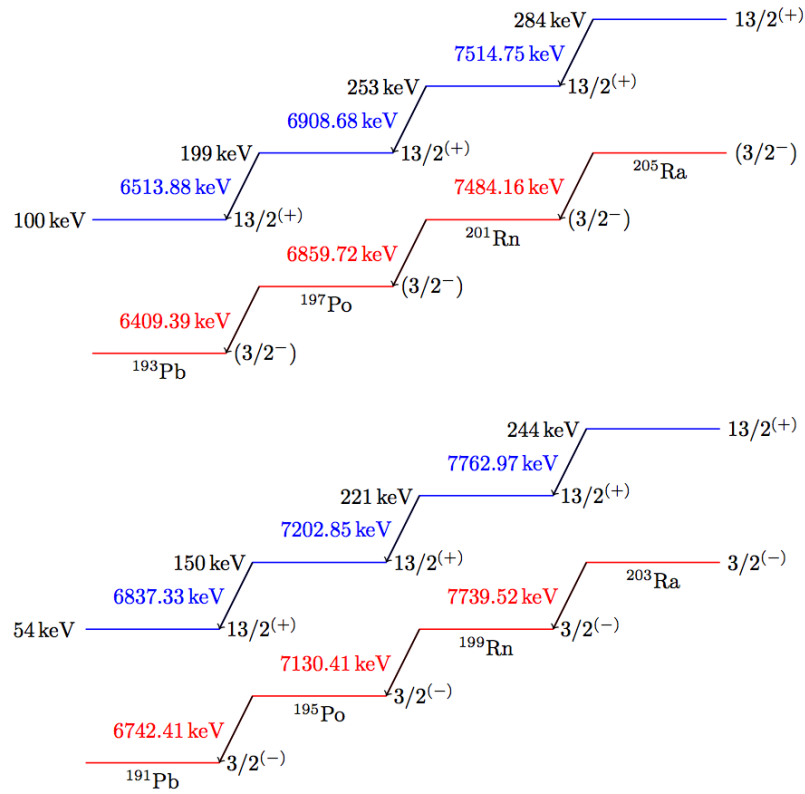
Figure 6.9: The α-decay scheme of isomeric and ground, from ^{203,205}Ra to ^{191,193}Pb. Excitation energies in each isotope were determined by using the energy of the $13/2^+$ state in ^{195,197}Po and the Q_α-values [96, 97]. The blue and red lines represent the isomeric and ground states, respectively. This figure is taken from Ref. [68].

The excitation energy E^* of the excited state in ^{195,197}Po isotopes can be obtained in terms of the measured cyclotron frequency by using Eq. (4.2.5) Ref. [68]:

$$E^* = (\bar{r}_m - \bar{r}_g)(m_{ref} - m_e)c^2, \tag{6.1}$$

Here $\bar{r}_m$ ($\bar{r}_g$) is the weighted average of the cyclotron-frequency ratios of isomeric (ground) state.

In addition, the excitation energies of the isotopes that are linked with ^{195,197}Po by α-decay chains, as shown in Fig. 6.9, were obtained by subtracting or adding the difference in Q_α-values between the two high- and low-spin chains. Based on the new results presented here, the $13/2^+$ states never become the ground states in ^{191,193}Pb, ^{195,197}Pb, ^{199,201}Rn and ^{203,205}Ra. The excitation energies of
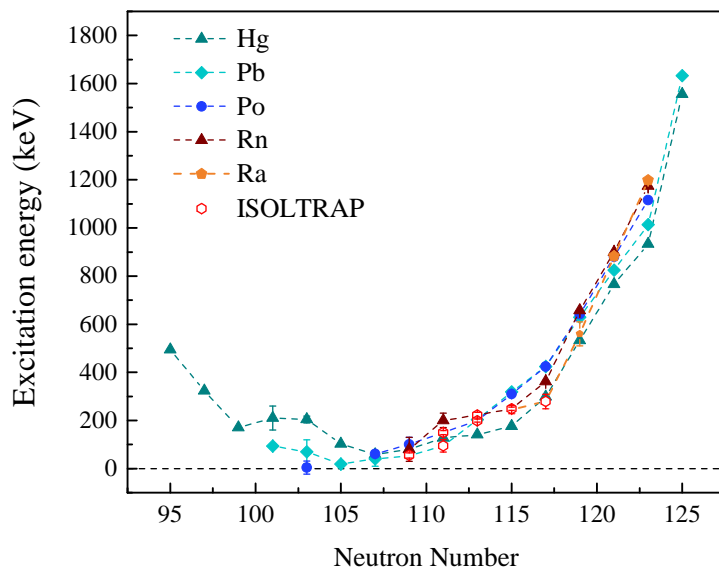
Figure 6.10: The energy of the $13/2^+$ state in odd-A polonium isotopes in the Pb region. The excitation energies obtained by using the new mass values and α-decay Q_α-values. The ISOLTRAP's results are shown in red and data from [96, 97] are shown with other colors. This figure is taken from Ref. [68].
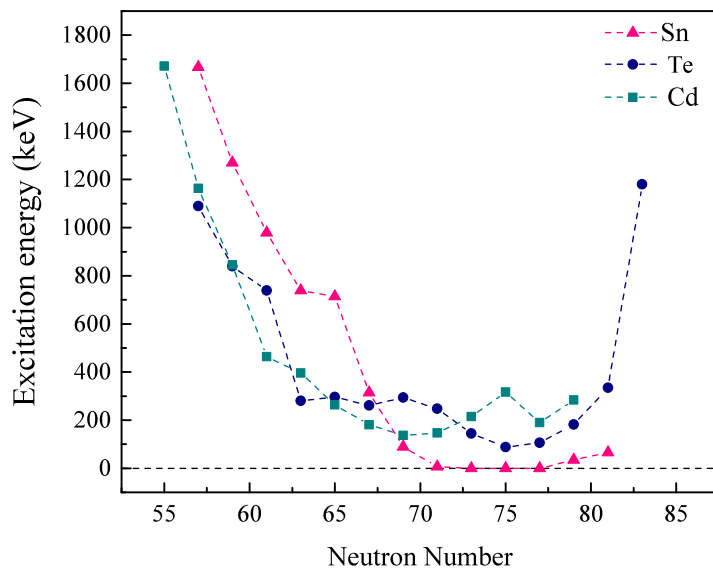

Figure 6.11: The energy of the $11/2^-$ state in the neutron-rich isotopes near the tin region. Data are taken from [96–98].

the $13/2^+$ states are presented in Table 6.2. Figure 6.10 illustrates the excitation energies of the $13/2^+$ states over a long chain of isotopes in the Pb region.

The excitation energies show a parabolic trend, with a minimum at $N = 103$ for polonium, $N = 105$ for lead and $N = 107$ for mercury. The same trend is seen in the neutron-rich tin region as illustrated in Fig. 6.11. The $\nu h_{11/2}$ state is identified as an excited state in neutron-rich cadmium ($Z = 48$), tin ($Z = 50$) and tellurium ($Z = 52$) isotopes. The excitation energy of the $11/2^-$ state drops from $N = 82$ and nearly degenerate with the ground states $\nu s_{1/2}$ and $\nu d_{3/2}$ between $N = 65$ and 82. This likely implies a decrease in the energy spacing between the $11/2^-$ and $3/2^+$ states with smaller N, which causes a level inversion where the excited state $11/2^-$ becomes the ground state for nuclei between between $N = 73$ and $N = 77$.

Another striking feature is the similarity between isotopic chains. They all behave alike, whether being a closed shell at $Z = 82$ (Pb), with two proton holes below $Z = 82$ (Hg), or having protons in orbitals above $Z = 82$ (Po, Rn, and Ra). The energies of the $13/2^+$ states in these isotopes seem to be independent of the occupation of the proton shells.

6.5   Summary

This chapter discussed the results of the mass measurements of ^{195g,m}Po and ^{197g,m}Po. With purified ion beam the masses of $^{(195,197)m,g}$Po were measured by using Penning-trap mass spectrometry. Based on the mass values, the excitation energy and the state ordering of the $13/2^+$ state in ^{195,197}Po were obtained for the first time. The state identification was achieved by adding an α-decay-spectroscopy setup behind the MR-ToF MS. The $13/2^+$ excitation energy of the polonium isotopes' α-decaying daughters and parents was determined. The results provide information on the behaviour of the $13/2^+$ states in the lead region near $N = 104$, which remain excited states.

The remainder of this page was intentionally left blank.

Chapter 7

Decay-spectroscopy measurements

The α energies and the half-lives of the ^{195m,g}Po isotope have been measured by several experimental groups in the past. The earlier reliable study was undertaken by Sivola [104]. In his work, ^{19}F beams delivered from the Berkeley Linear Accelerator with an energy 140-160 MeV bombarded an isotopically enriched ^{185}Re target. The ^{195}Po was formed in 9n fusion-evaporation reactions. Evaporation residues were deposited by a helium gas stream on an aluminium plate located in front of a solid state counter where the subsequent α-particle spectra were measured. He reported the observation of two α groups that have energies of 6.624(8) MeV and 6.710(10) MeV with half-lives of 4.5(5) s and 2.0(2) s. The previous measurements of ^{195g}Po resulted in significantly longer half-lives of about 30 s and they are presented in [104]. Wauters and a group from Leuven University precisely measured α energies and half-lives of presented Po isotopes [87]. They created polonium isotopes through the decay of Rn isotopes. The heavy Rn isotopes were produced at Leuven Isotope Separator On Line (LISOL) via heavy ion induced fusion-evaporation reactions (240 MeV Ne projectile on heavy ^{182}W target). The beam was implanted into a movable aluminized mylar tape. A silicon detector was used to record the activities of the implanted beam. The half-lives resulting from this study were 1.92(2) s for high-spin state and

4.64(9) s for the low-spin state, in agreement with the those in Ref. [104]. The half-lives of the $^{195(g,m)}$Po isotope, were also measured by a group from the University of Jyväskylä through α-decay studies of neutron-deficient Ra isotopes and their corresponding daughter Rn and grand-daughter Po. The delivered copper beams ^{65}Cu, with energies up to 300 MeV, from the JYFL accelerator were used on a ^{141}Pr target to produce the ^{203}Ra isotopes via 3n evaporation channel. A gas-filled recoil separator method was used to separate the ^{203}Ra isotopes from the beam. The α decays of the implanted ^{203}Ra isotopes and those resulting from daughter and grand-daughter activities were identified by silicon detectors. The half-lives reported are 3.9^{+32}_{-12} s for low spin and 2.8^{+10}_{-6} s for high spin [105], with a notable difference from the previous measurement.

In all previous studies, the neutron-deficient Po nuclei were created in fusion evaporation reactions. A significant advantage of this method is the production of an isobarically pure sample, however, the energy of the isomeric state is almost degenerate with the ground state. Thus, the α energy spectrum of the isomeric state always overlaps with the one produced by the ground state. Besides this fact, the polonium isotopes can be contaminated by isobaric products at high-energy tail [90], when they are produced by Isotope Separator On Line (ISOL) method. Considering all the above facts, the measured half-life value can be shifted from the real one. Therefore, the half-life measurement of the investigated state in an isobarically and isomerically pure beam is preferable. At ISOLTRAP, the measurements of half-lives became available with increasing precision. Thanks to ISOLTRAP's MR-ToF MS [106] in combinations with the isomeric selectivity of the RILIS [107], hyper-pure samples can be isolated and studied with the DSS2.0 [82]. In this chapter, the experiment to determine the half-lives of the $^{195(g,m)}$Po using the α-decay is discussed.
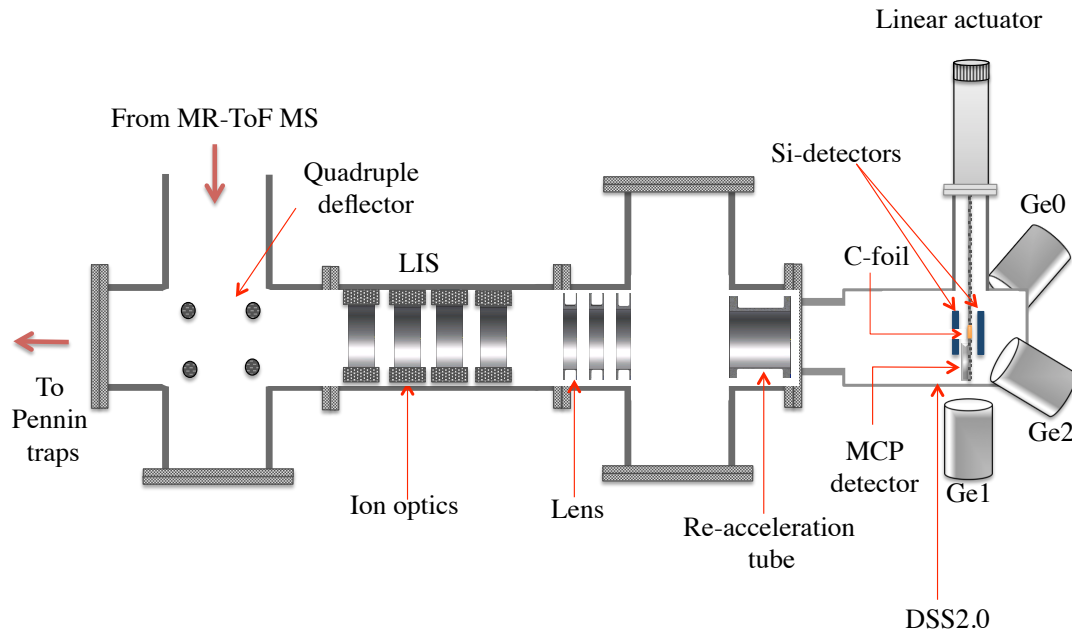
Figure 7.1: A schematic of the decay station used during the experiment.

7.1 Experimental setup

As it was mentioned above the MR-ToF MS with RILIS selectivity were used to deliver a pure sample of ^{195}Po to the DSS2.0. A possible isobaric contaminant was ^{195}Tl, see Fig. 6.2(a), that could come from the hot cavity in the ion source from ISOLDE [90]. In the polonium experiment, a mass resolving power of 10^5 was obtained, while 10^4 was required to purify ^{195}Tl. This was sufficient to remove any isobaric contaminant from the polonium beams. The pure sample was then extracted from MR-ToF MS, deflected to the DSS2.0, and implanted into the C-foil, which has 90 nm thickness. Figure. 7.1 shows a schematic of the decay station that was used during the experiment.

The α particles, emitted from ^{195}Po, were detected by two silicon detectors placed on two sides around the implantation spot. A circular detector PIPS, with an active area 300 mm^2, set behind the C-foil and another annular detector APIPS, with an active area 450 mm^2, set in front of the C-foil. The two silicon detectors were calibrated using the known α-particle energies from the decay of ^{195,196,197}Po
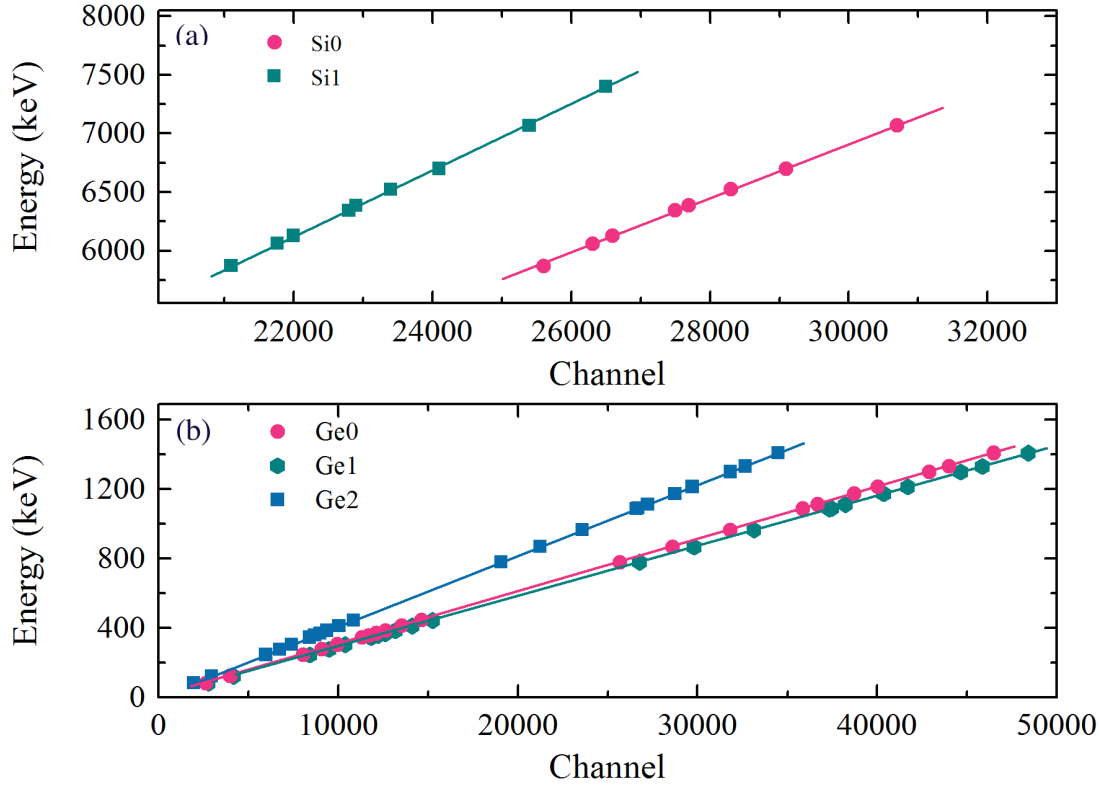
Figure 7.2:   The energy calibration curves for the silicon detectors, (a), and
HPGe detectors, (b), obtained during the run.

and ^{221}Fr. Decay products resulted from ^{221}Fr such as its daughter ^{217}At, grand-
daughters ^{213}Bi and ^{213}Po were also used. Figure. 7.2(a) shows the calibration
curves for both silicon detectors. The energy resolution (FWHM) of them was
obtained during the experiment; the energy resolution of the circular detector
was 44 keV and 35 keV for the annular detector at 6341 keV. SRIM calculations
showed that, the implantation depth of ^{195}Po ions with an energy of 3 keV is 57 Å.
The calculations also showed that, the solid angle coverage for both APIPS and
PIPS detectors is around 63% of 4π. In addition, the detection setup includes
three HPGe detectors placed around DSS2.0, as shown in Fig. 7.1. They were
labelled Ge0, Ge1, and Ge3. The energy calibration of the HPGe detectors system
was performed during the run using ^{133}Ba and ^{152}Eu. The calibration curves are
shown in Fig. 7.2(b) and were used for the analysis. The photo-peak efficiency for
the three detectors was measured using ^{152}Eu (16.3 kBq) and ^{133}Ba (11.6 kBq).
Figure. 7.3 illustrates the efficiency curves for γ rays that were obtained from the
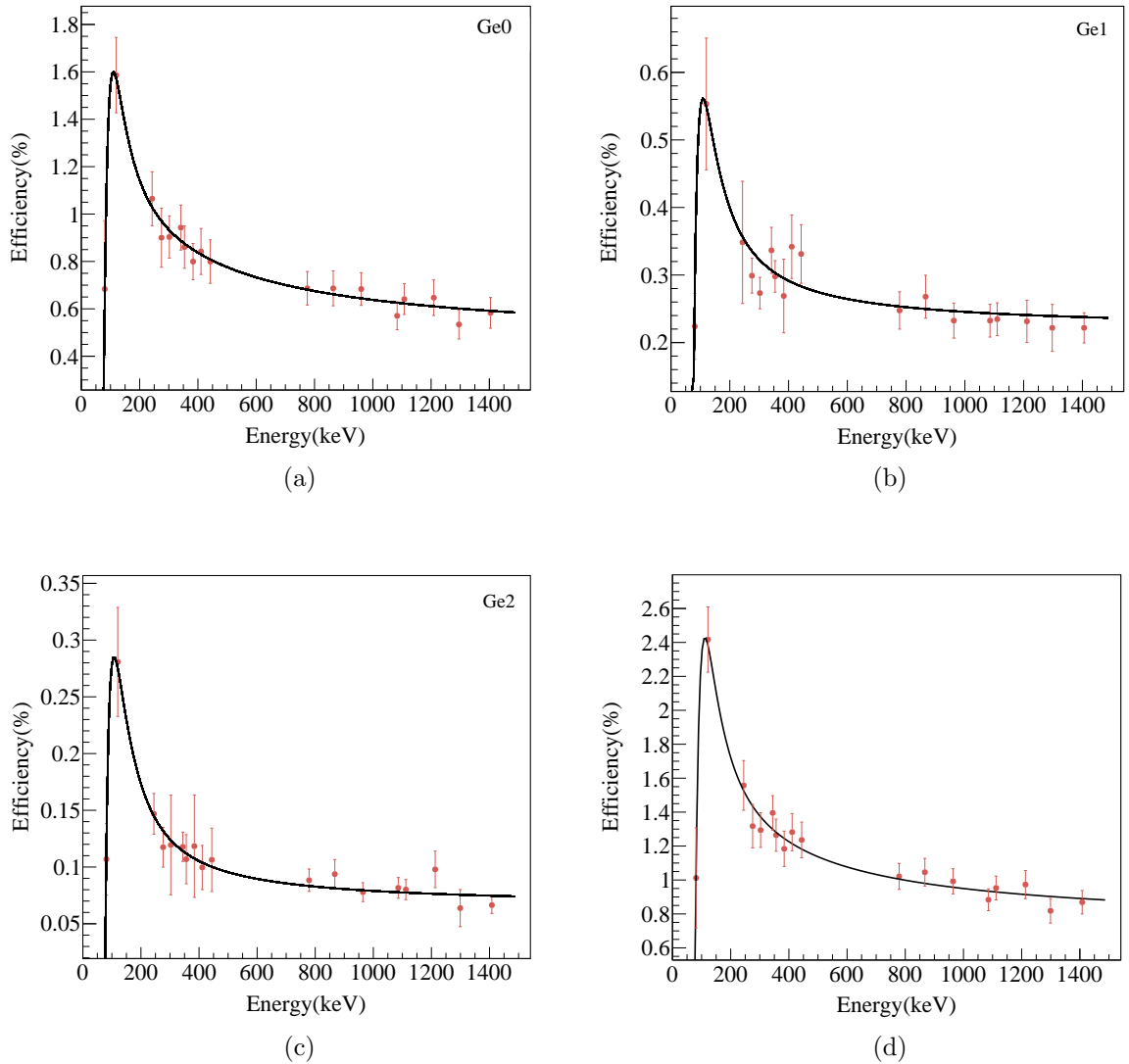three HPGe detectors for a total efficiency of 1% at 1 MeV [108].

Figure 7.3: The photo-peak efficiency curves of γ-ray calculated for all HPGe detectors separately. The the total efficiency is shown in (d). The solid line shows a fit to the efficiency curves [108].

During the experiment, a total of six measurements of isomeric half-life of ^{195}Po were acquired. They were grouped into two sets according to the RILIS laser setting. A summary of the beam content is given in Table 7.1. Set I consists of three measurements obtained with a laser frequency tuned to 11853.73 cm^{-1} to have an as pure isomer as possible (the laser frequency that was used in the mass measurements was 11853.75 cm^{-1}). The purified low-energy (3 keV) polonium beam was implanted into the C-foil for 10 s (within a time window set according to the expected lifetime). Afterwards, the beam turned off for 10 s waiting for

Table 7.1: The beam content, according to the RILIS laser setting, during ^{195}Po half-life measurements.

	RILIS setting	Measurement	Date	Counts		$R_m(\%)$
				m	g	
Set I	11853.73 cm^{-1}	1	27Aug15	911	74	92
		2	27Aug15	15768	1386	90
		3	27Aug15	12705	1186	90
Set II	broadband	4	27Aug15	5786	3424	58
		5	27Aug15	50797	29261	58
		6	28Aug15	41208	22862	60

^{195}Po to decay. The beam was turned on again for 10 s to build up the polonium and record the growth signals. Set II, includes three measurements, that were recorded with broadband laser setting. A time window of 20 s implantation and 30 s decay was applied for this measurements. The half-life of ^{195g}Po was also measured using set II. The energy signals for the two silicon detectors were acquired event by event and time stampted as well as the pulse of Mass Measure 6.0 (MM6), which is associated with the beam implantation onto the C-foil.

7.2 Analysis procedure

The half-life curve was obtained by plotting time differences between the α-decay event time stamp and MM6 pulses. An energy gate was applied to the decay curve to only include α particles originating from one particular state and ignoring other activity. The fit-function is defined to include both decay and growth curves with four free parameters as follows:

$$C = \begin{cases} C_0 \cdot e^{\frac{-ln2 \cdot t}{t_{1/2}}} + B, & \text{for decay curve,} \\ C_0 \cdot (1 - e^{\frac{ln2 \cdot (t-t_0)}{t_{1/2}}}) + B, & \text{for growth curve.} \end{cases}$$

Here C is the count rate at time t, C_0 is the count rate at time $t = 0$, $t_{1/2}$ is the half-life, t_0 is the start of the growth curve, and B is a flat background.

For sake of comparison, both sets were fitted using two methods: the least-squares fit (LS) and maximum likelihood fit (ML) [92, 93, 109]. The later was considered as a more reliable method when dealing with low counting experiments, especially if the total numbers of counts per bin are very few (or zero) [109].

7.2.1 $\quad {}^{195m}$Po

In the analysis of ^{195m}Po half-life, special care was taken to eliminate the effect of the possible overlap between the tails of the 6699 keV and 6609 keV lines. Thus, the upper energy limit was fixed at E_α=6800 keV, while the lower energy gate was scanned across different limits. The resulted curves were then fitted to obtain the half-life. Set I shows a stable fit results independent of the energy gate. In set II, a shift in the isomeric half-life towards low values was found up to 6680 keV where the half-life almost became stable. This was due to the non-negligible overlap of the tail of the isomeric state with the ground state, see Fig. 7.4 (b). The deduced half-life versus the α-energy gate is shown in Fig. 7.5. The optimal energy gate was found to be from 6680 keV to 6800 keV. This energy gate was then applied to the decay curve during the fit.

The half-life results of ^{195m}Po were obtained by fitting the decay activity curves using the fit-function and methods mentioned above. The fit residual was plotted to validate the accuracy of the fit model. The residue is defined as a difference between an observed event and the corresponding estimated value resulting from the fit. The decay curve and the resulting fit from the set I and II are shown in Fig. 7.6 and 7.7. In the set I, the residual is scattered around the zero-point as shown in Fig. 7.6. Although the residue of set II (measurements with a beam-on time 20 s) follows the same pattern, a systematic trend at the beginning is observed as illustrated in Fig. 7.7.

(a)

(b)
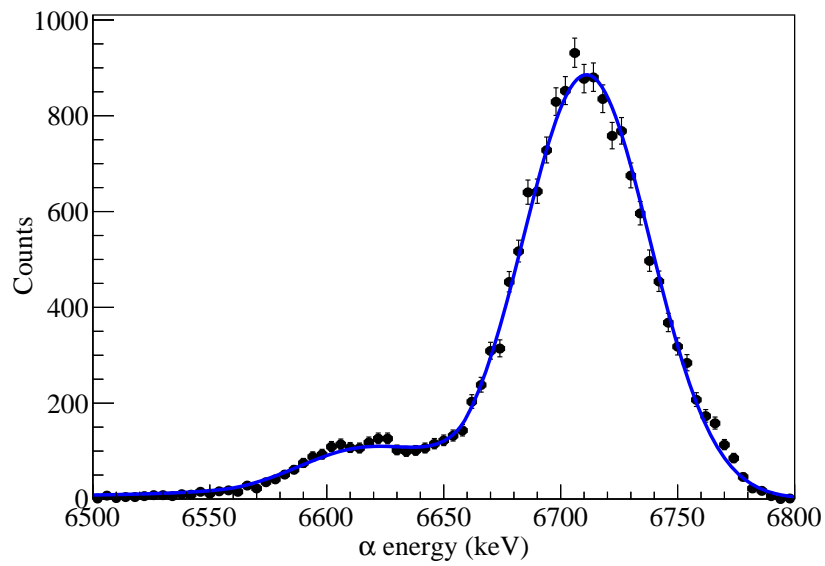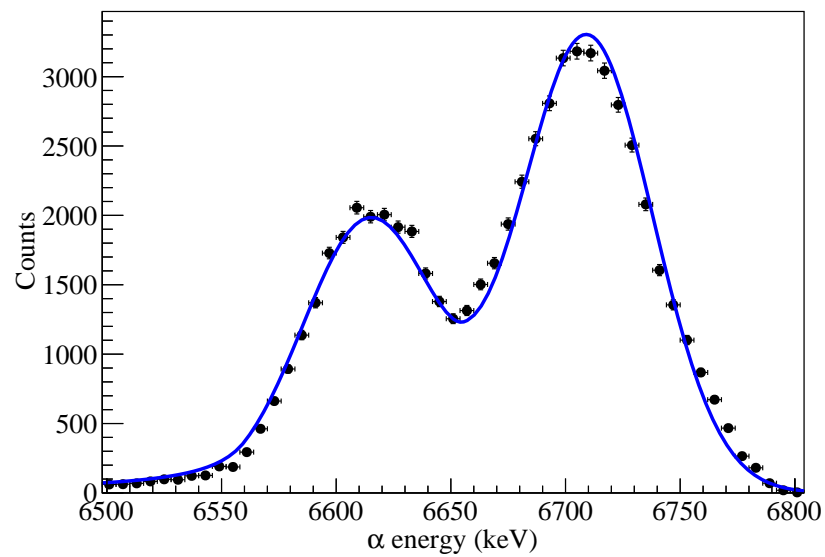
Figure 7.4: α-spectrum associated with ^{195}Po decay. The spectrum in (a) was obtained with RILIS wavenumber 11853.75 cm^{-1} and the one in (b) was obtained with the broad-band setting.
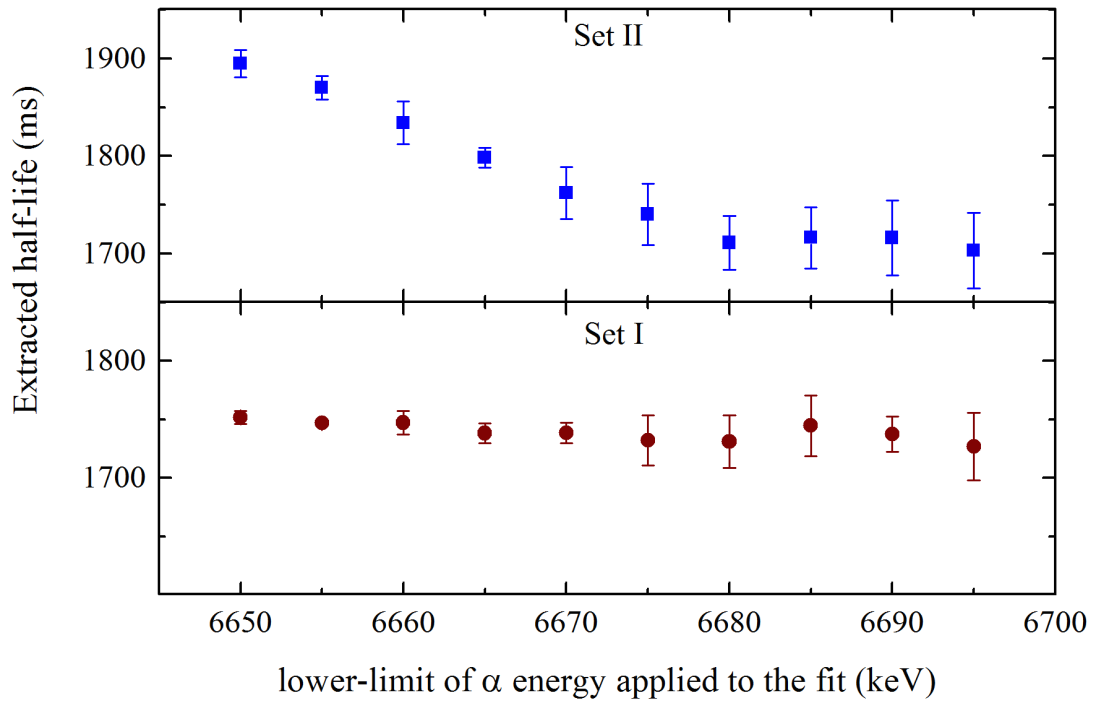
Figure 7.5: The half-life obtained by varying the low-energy limits. The upper part is determined from the fit of set II and the lower part from set I. The increase in the error bar results from the fact that the statistics are being removed as the gate width decrease.

The systematic pattern in the residual may result from the measurement errors or indicates the existence of some parameters that were not taken into consideration in the fit model. Therefore, several tests were performed in an attempt to understand the reason behind these outliers and to search for any systematic effects that may affect the half-life results.

Although the optimal-energy gate was applied, a further test for any possible contributions coming from a small fraction of long-lived impurities was performed to the questionable fits. A sum of two exponential distributions was used as a fit-function with extra three parameters: the half-life of the ground state, the weight of the ground state, and the weight of the isomeric state. The first parameter was fixed to the literature value [87], and the last two parameters were changeable from 0 to 1. The half-life that determined in this way shows no significant change to the half-life values with an overall increase in the statistical uncertainty. No enhancement in the systematic pattern was observed in the residual when using the two exponential fit.
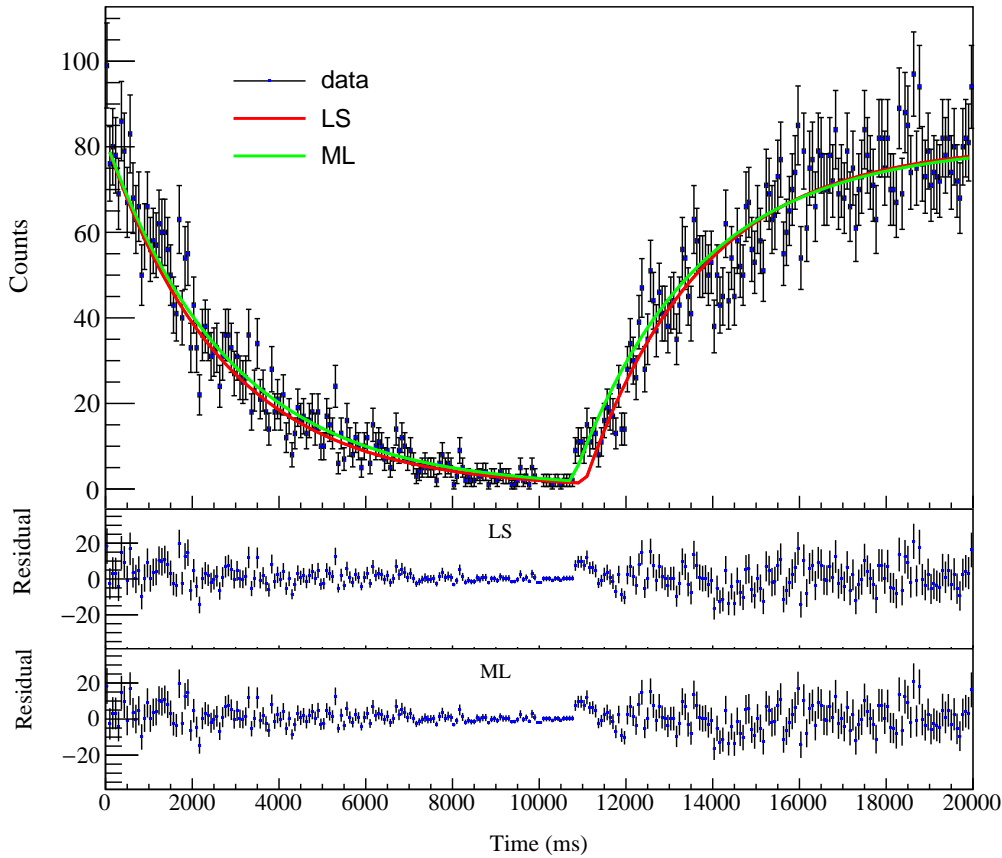
Figure 7.6: Decay-growth curve of the ^{195m}Po and the fit obtained with ML
(green) and LS (red) methods for set I. The fit-function includes one decay time
and one counts number component. The corresponding residuals are displayed
in the lower panels. The plot shows a random pattern in the residuals.

The possible for the counting-rate dependence was also tested by excluding the
contribution of data from the channels with high count rate, and then re-fit the
curve. The number of the excluded time channels were varied from 0 to 2 s in
steps of 0.1 s (for the set I from 0 to 1.5 s in steps of 0.05 s). The test was
first performed on the decay curve only after removing the growth curve. For
all measurements including those with a good fit (set I) the resultant half-life of
the ^{195m}Po as a function of the excluded channels remains consistent with the
first value (at $t = 0$) as the data being removed, see Fig. 7.8 (a). Therefore, no
evidence from the decay curve analysis indicates the presence of any counting-rate
dependence.

In the same manner, the analysis was carried out on the curve including both
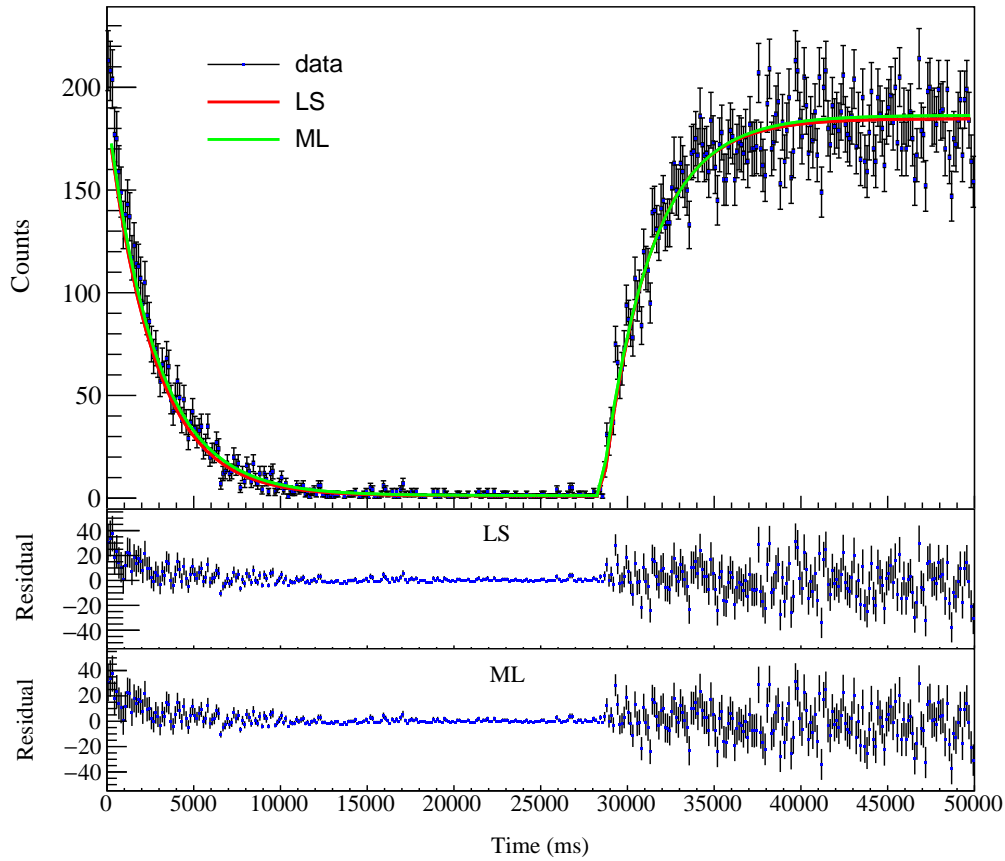
Figure 7.7: Decay-growth curve of the ^{195m}Po and the fit obtained with ML (green) and LS (red) methods for set II. The fit-function includes one decay time and one counts number component. The corresponding residuals are displayed in the lower panels where a systematic pattern is observed.

decay and growth events. In the data acquired with long implantation time (beam-on time 20 s), the half-life of ^{195m}Po is systematically shifted towards lower values as the high-rate data are excluded, as seen in the Fig. 7.8 (b). This might explain the presence of the systematic pattern in the residual. The growth count rate seems to be slightly different about the decay count rate. In order to correct this shift, the total number of counts of the growth curve was set to be independent of the one in the decay curve. The fit-function was modified to include two count rate parameters: C_0 for the decay curve and C_1 for the growth curve. As an additional check, the shift in the extracted half-life, from the modified fit-function, as high rate being removed, was examined (see Fig. 7.8 (b)). The results show a very small residual rate dependence, however,
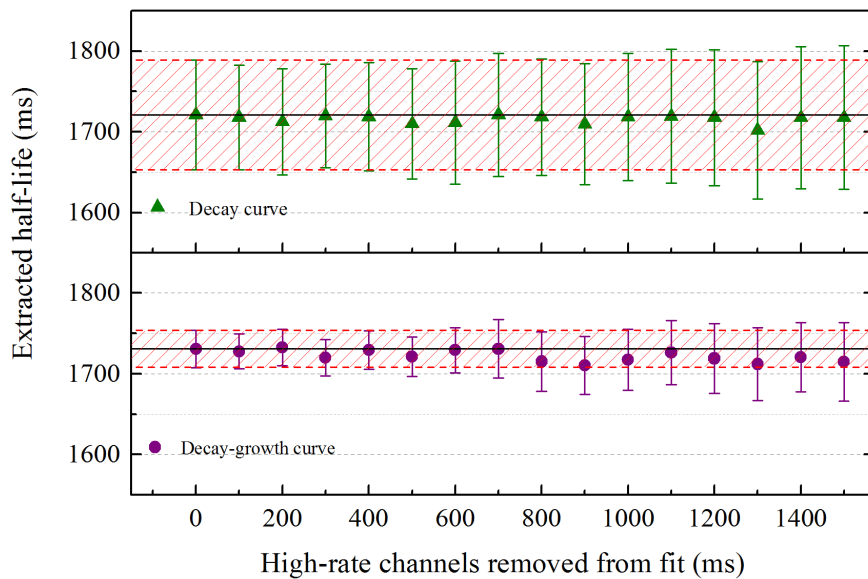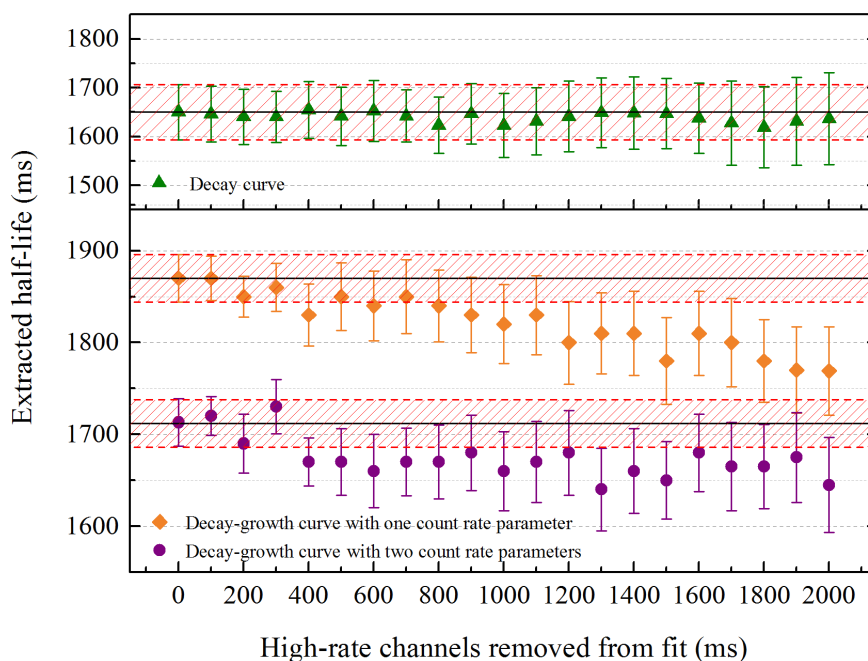
Figure 7.8: The determined half-life of ^{195m}Po as the high-rate channels are removed. Set I in plot (a) shows no evidence of rate dependence unlike set II, (b), where the half-life deduced from decay-growth curve was systematically shifted to low values as the rate data are removed. This case is seen when the fit-function includes one parameter of count rate, see text for more details. The solid black line is the first value of the half-life (with no channels being removed) and the shaded red area its uncertainty.
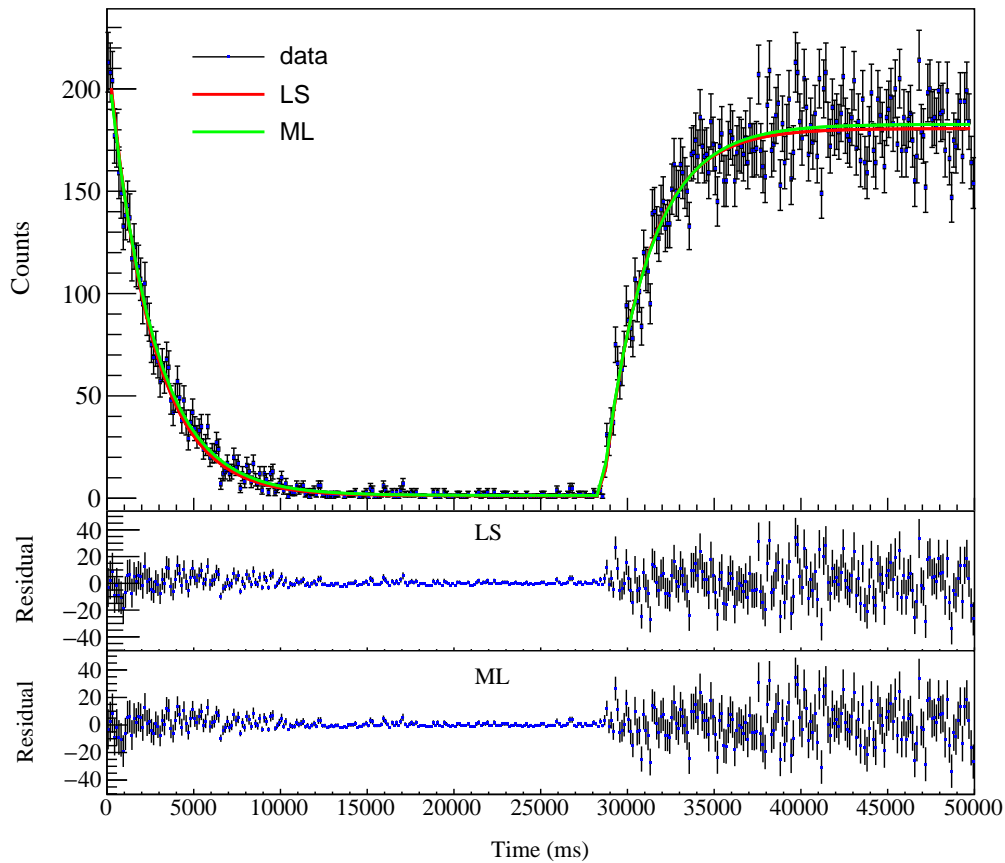
Figure 7.9: Decay-growth curve of the ^{195m}Po and the best fit for set II. The fit was performed with one exponential fit-function includes two different number of counts components. The fit obtained with ML (green) and LS (red) methods. The corresponding residuals are displayed in the lower panels with no systematic pattern is observed.

the absolute difference of the resultant half-lives are within the uncertainties of the first value. The residual obtained from the modified fit-function demonstrates an improvement in the fit as illustrated in Fig. 7.9.

Table 7.2: Deduced ^{195m}Po half-lives analysed with the resulting statistical uncertainties.

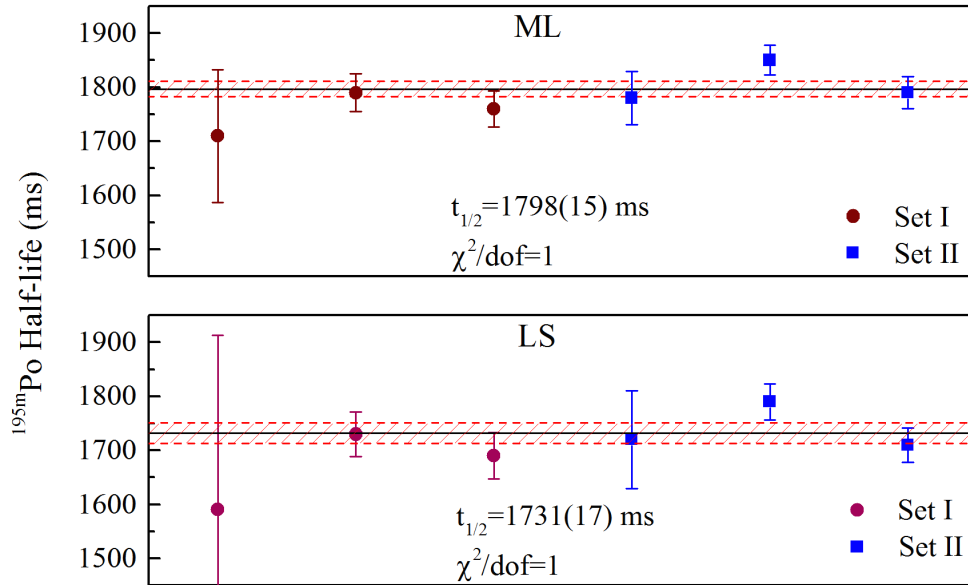|	Set I		Set II	
	ML	LS	ML	LS
Decay-growth curve	1772(24)	1705(30)	1815(23)	1744(27)
Decay curve	1765(35)	1680(55)	1804(31)	1720(40)

Figure 7.10:   The half-life of ^{195m}Po with statistical errors deduced from the 6 measurements using ML (upper part) and LS (lower part) methods. The weighted average of the half-life is represented by the solid black line. The red shaded area is the uncertainty of the weighted average.

By using the analysis procedure described above the half-life of ^{195m}Po was extracted from the fit using ML and LS. The fit results for all measurements were converged and resulted in a value close to one for $\chi^2/$dof. The half-life curve and the resulting best fit are shown in Figs. 7.6 and 7.9 for the set I and II, respectively. Treating each set as an independent measurement of the ^{195m}Po half-life, the ML of the decay-growth curve yields a half-life of 1772(24) s for set I and 1815(23) for set II. The LS for the decay-growth curve leads to less half-life value for both sets. The comparison of these results with those obtained from the decay curve reveals a consistency within 1σ.

Combining these sets, the weighted average deduced from the six measurements when using ML method yielding a ^{195m}Po half-life of $t_1/2$=1.798(15) s with a $\chi^2/$dof=1 for the decay-growth curve, see Fig. 7.10. This value is in a good agreement and even more precise than the value resulting from the decay curve ($t_1/2$=1.794(21) s) when using the same method. The half-life weighted average obtained from LS is 4% (5%) less than the ML values of the decay-growth (decay) curve. Generally, the half-life of ^{195m}Po deduced in this work is lower than the previous literature value with precision similar to the previous one [87]. The
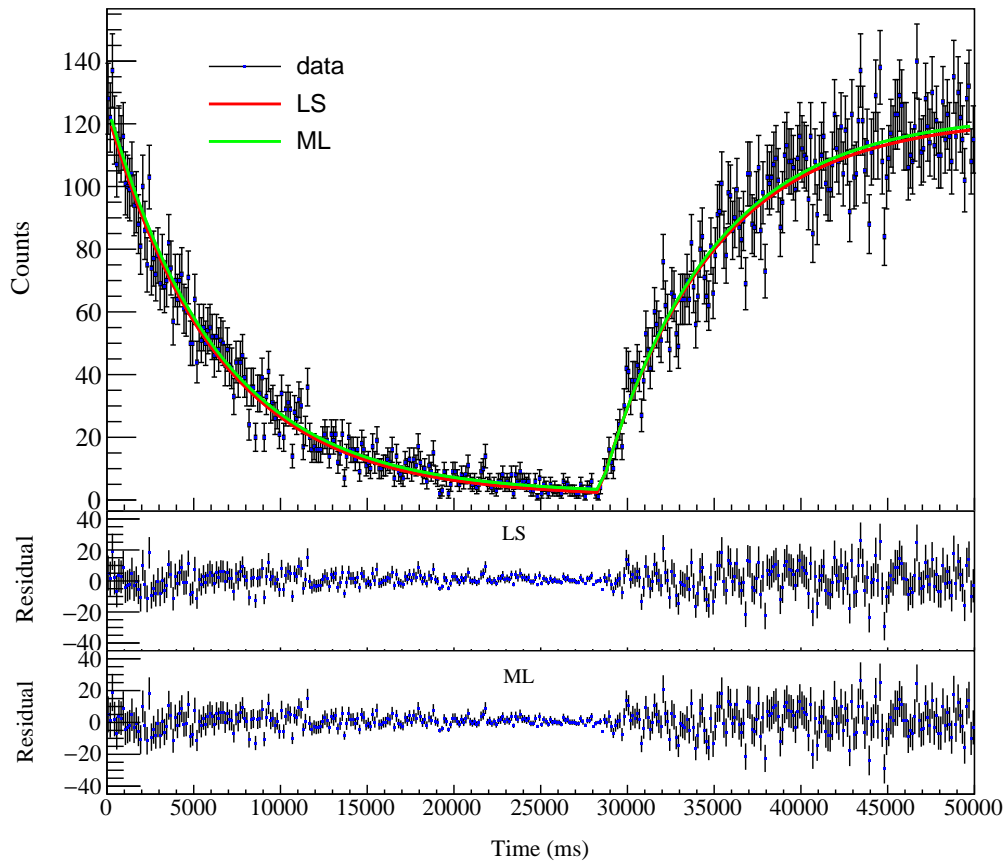
Figure 7.11: Decay-growth curve of the ^{195g}Po and the best fit. The fit obtained with ML (green) and LS (red) methods. The corresponding residuals are displayed in the lower panels.

weighted average values for each set are tabulated in Table 7.2 with the results when considering only the decay curve. The quoted error associated with these values are purely statistical.

7.2.2 ^{195g}Po

The half-life of ^{195g}Po was determined from set II where the beam-on time was 20 s and the waiting time was 30 s. This waiting time was sufficiently long to remove any other background activities coming from the other state. The half-life of ^{195g}Po was extracted from the fit-function mentioned above using ML and LS methods. The decay-growth curve and the resulting best fit are displayed
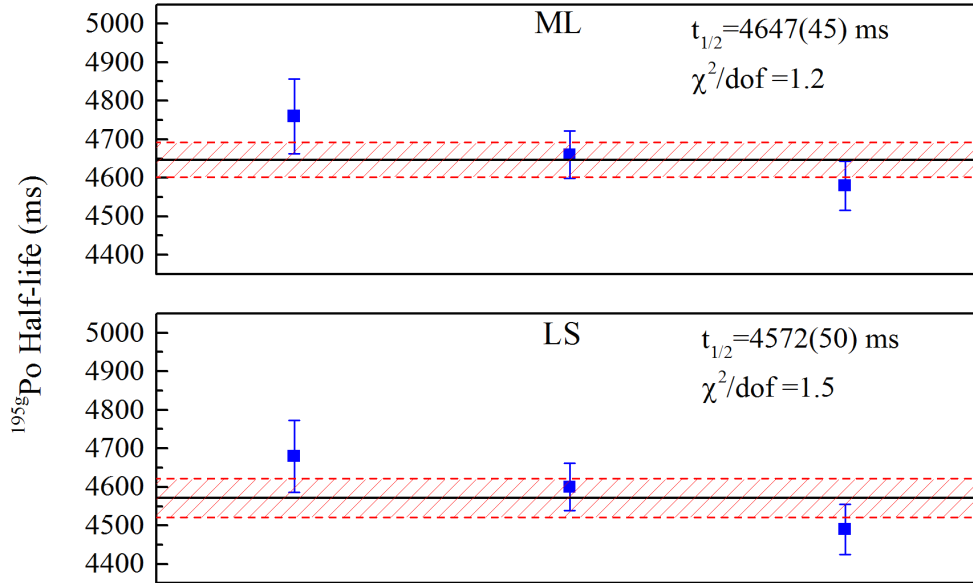
Figure 7.12: The half-life of ^{195g}Po with statistical error deduced from the set II measurements using ML (upper part) and LS (lower part) methods. The weighted average of the half-life is represented by the solid black line. The red shaded area is the uncertainty of the weighted average.

Table 7.3: Deduced ^{195g}Po half-lives analysed with the resulting statistical uncertainties.

	Set II	
	ML	LS
Decay-growth curve	4647(45)	4572(50)
Decay curve	4633(59)	4523(63)

in Fig. 7.11. Figure. 7.12 shows the half-life values for the individual measurement from set II. The ^{195g}Po half-life demonstrates an agreement between values extracted from the decay-growth and decay curve using ML method. The ML results are in good agreement with Ref. [87] with an improvement in the precision. The half-life values obtained with LS method are 2% lower than ML method. These results are consistence with those in Ref. [87]. The results of ^{195g}Po half-life are shown in Table 7.3. The final results of our measurements are shown in Table 7.4
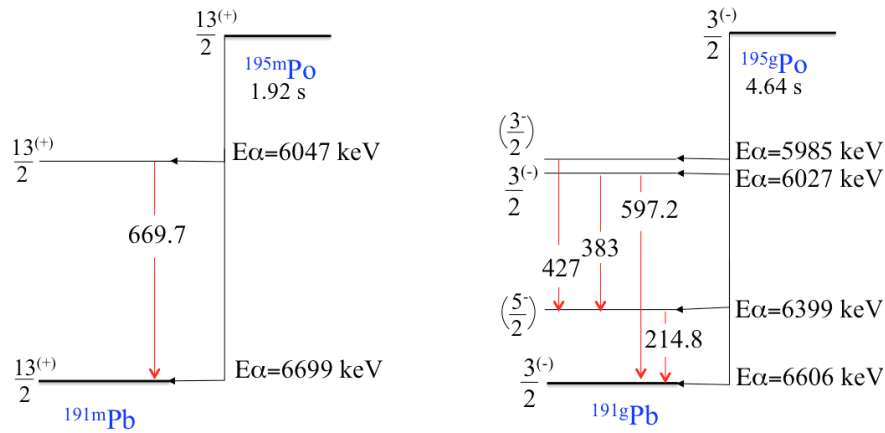
Figure 7.13: The decay schemes of $^{195(g,m)}$Po according to Ref. [90].

Table 7.4: The final results of the $^{195(m,g)}$Po half-life measurements that obtained in this work. The literature half-life values were taken from [87].

	Half-life (ms)	
	This work	Literature value
^{195g}Po	4647(45)	4640(90)
^{195m}Po	1798(15)	1920(20)

7.3 Alpha-gamma coincidence measurements

In addition to the half-lives measurements, the coincidences that occur between the emissions of α particles and γ rays ($\gamma - \alpha$ coincidence) were investigated. The two states of ^{195}Po nucleus (ground state with $3/2^-$ spin and excited state with $13/2^+$ spin) decay via α-particle emission to ^{191}Pb. The schematic of α-decay process for ^{195}Po is shown in Fig. 7.13. The α-particle energy spectrum in Fig. 7.14 displays α peaks originating from the decay of $^{195(g,m)}$Po to the daughters ^{191}Pb.

For a prompt identification of $\alpha - \gamma$ coincidences, the coincidence matrix between α decays and γ rays with a time window of Δt=3 μs (Δt is a time difference between the germanium and silicon detectors) was obtained as shown in Fig. 7.15. The $\alpha - \gamma$ coincidence events were identified between E_α=6000 keV and E_α=6050
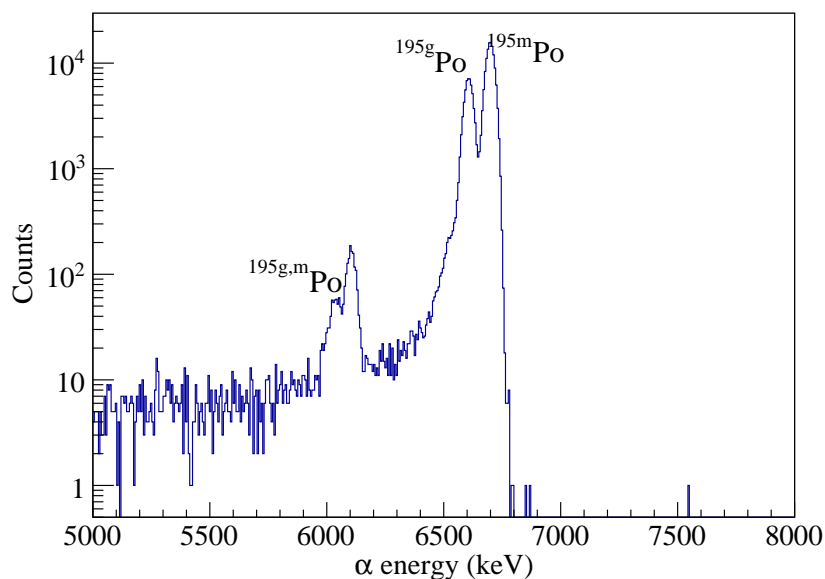
Figure 7.14: The energy spectra of α particles recorded in the silicon detectors.
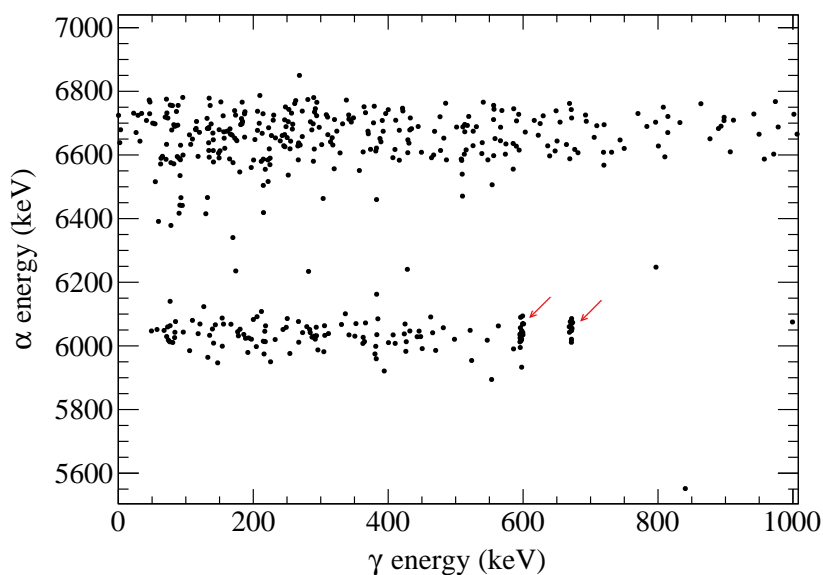
Figure 7.15:   2-D α-γ coincidences matrix, using a time difference between silicon and germanium detectors of Δt=3 μs. Arrows point to coincidence events.

keV. The coincidence spectrum of γ-ray energy can be obtained by gating on any α-peak energy of interest and obtaining γ that coincide with the gated α energy. In the coincidence analysis, a background subtraction was performed [110]. Thus, two energy gates on the tails around the gated peak of interest were chosen as close to the gated-peak region as possible. The sum of the two gates widths then

(a)

(b)
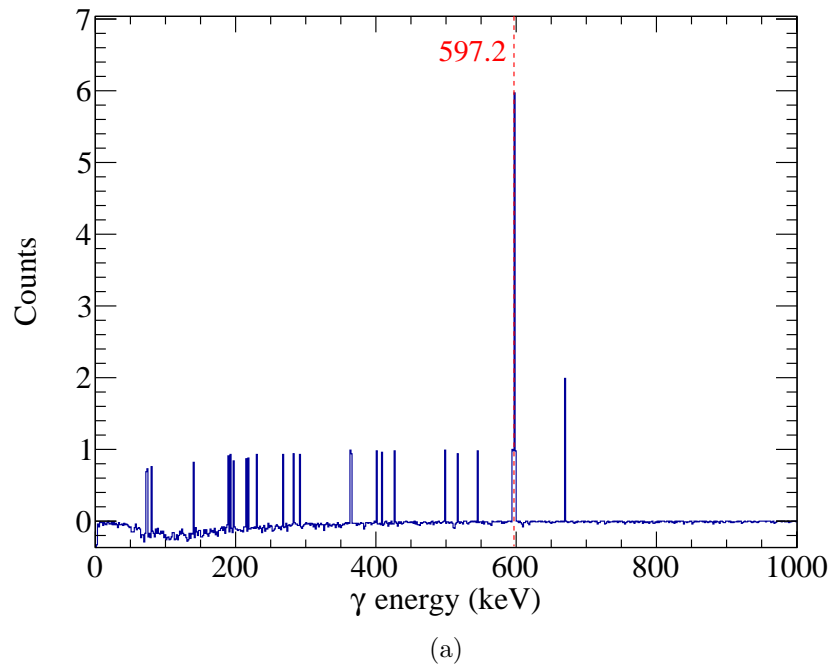
Figure 7.16: Random- and background-subtracted γ-ray energy spectrum in coincidence with $E_\alpha=6027$ keV, (a), and $E_\alpha=6047$ keV, (b).

was subtracted from the gate width under the peak of interest, see Appendix B.

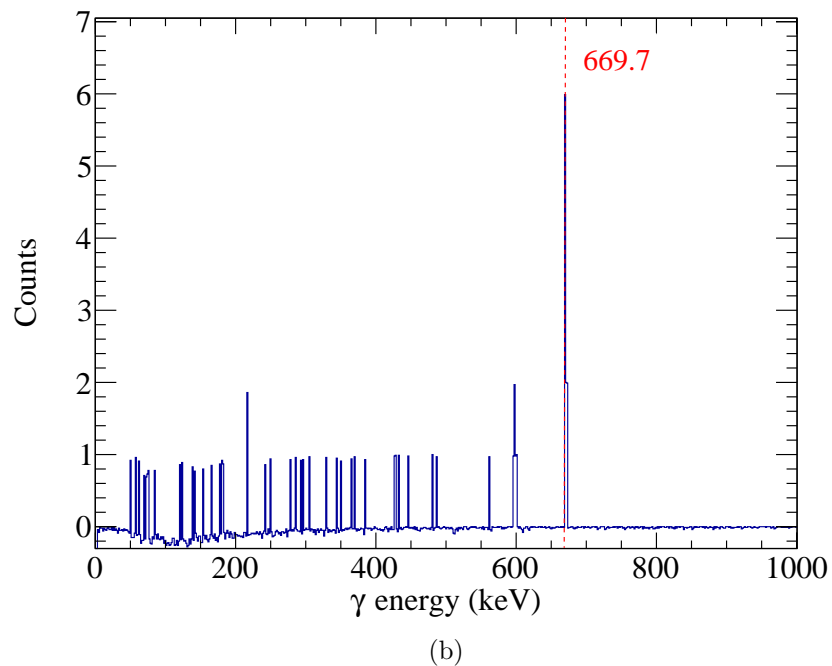By gating on the tails around the α peak at $E_\alpha=6027$ keV, the coincidence with one strongest γ-ray transition at 597.2 keV is seen, see Fig. 7.16 (a). The γ peak at

(a)

(b)
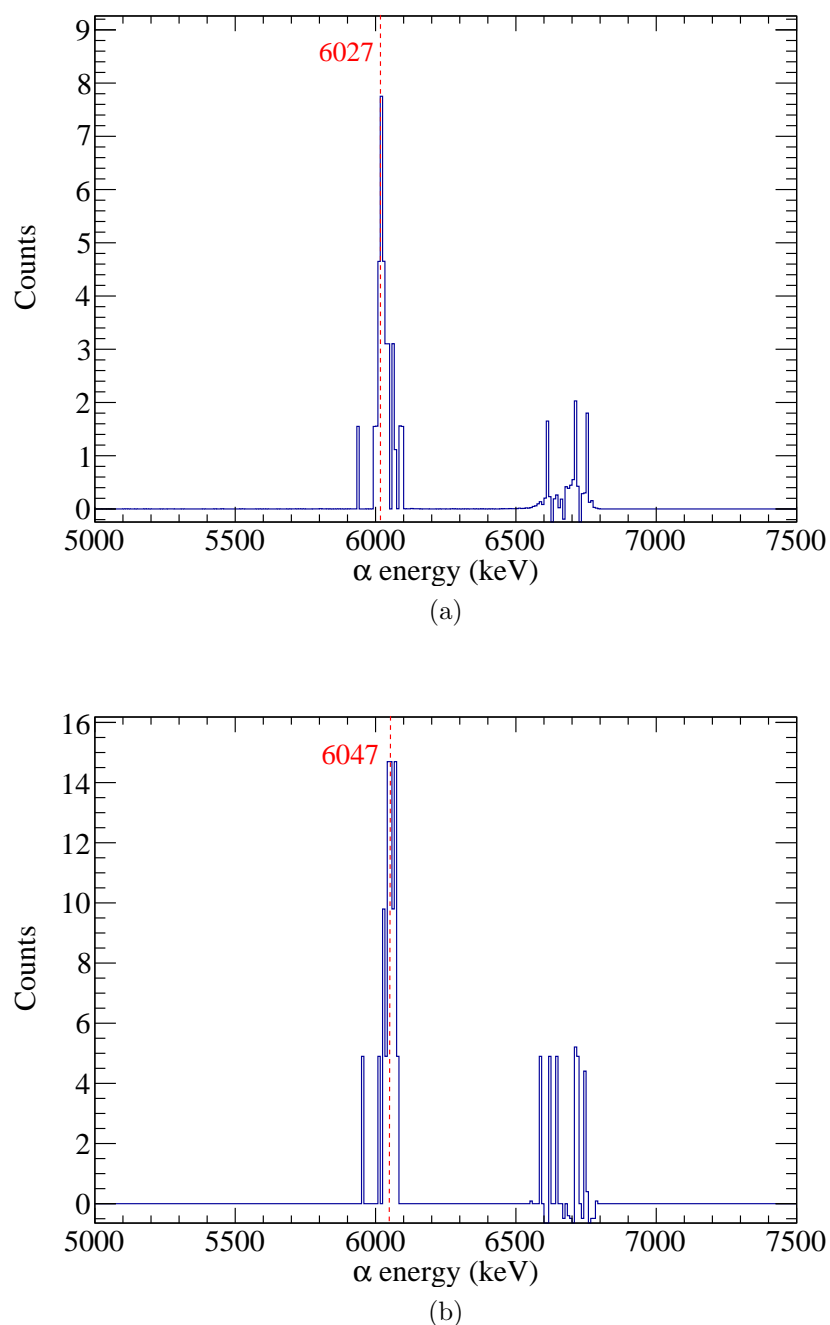
Figure 7.17: Subtracted random-background α-spectrum. The spectrum in
(a) and (b) are the background and random-subtracted of α-particle energy
obtained when gated on γ-rays 597.2 keV and 669.7 keV respectively.

597.2 keV resulting from the transition between the excited and ground states of
^{191}Pb [90]. Figure. 7.16 (b) shows the γ-ray transition at 669.7 keV when gating
on α at E_α=6047 keV. This 669.7-keV γ peak originating from the transition
between the excited states of ^{191}Pb [90]. The same procedures can be applied to

determine the α-energy coincidence spectrum. The α lines in coincidence with 597.2-keV and 669.7-keV γ transitions were observed when the energy gate was set on those transitions. Figure. 7.17 shows the coincident α spectrum when gating on 597.2-keV and 669.7-keV transitions. The others γ-ray transitions appeared in the schemes of ^{195g,m}Po in Fig. 7.13 were investigated. However, the statistics collected in this experiment was not sufficient to clearly distinguish any γ rays when gating on α energies coincidences with these transitions.

7.4   Summary

In this chapter, the results of the α-decay spectroscopy studies were discussed. The isomer selectivity of RILIS combined with the isobar purification of the the MR-TOF MS allowed to deliver a hyper-pure beam to the DSS2.0. Consequently, the half-lives of ^{195g,m}Po were determined and yielded 4647(45) and 1798(15) for the ground and isomeric states, respectively (see Table 7.4). In addition, $\alpha - \gamma$ coincidences were investigated and the main $\alpha - \gamma$ peaks were identified. However, the limited statistics did not allow to extend beyond the existing knowledge on the decay of ^{195}Po to ^{191}Pb.

The remainder of this page was intentionally left blank.

Chapter 8

Conclusion

Mass measurements of the neutron-deficient $^{195,197(g,m)}$Po and ^{199m}Po isotopes have been performed using the ISOLTRAP setup in combination with RILIS laser purification and α-decay spectroscopy. The RILIS laser system was used to selectively enhance production of either the isomer or the ground state of polonium. An additional isobaric purification for the beam delivered from ISOLDE was achieved with ISOLTRAP's MR-ToF MS to suppress any surface-ionised contaminants such as thallium.

In this experiment, the installation of α-decay-spectroscopy setup behind the MR-ToF MS demonstrates how decay spectroscopy can add valuable information to mass spectrometry measurements. This is the first application of MR-ToF-assisted decay-spectroscopy at ISOLTRAP. The α-decay spectroscopy was used to identify the nuclear state that was present in the ToF-ICR spectrum. In addition, it provided an accurate ground-to-isomer ratio necessary for accurate mass measurements.

The hyperfine structure of the odd-A polonium isotopes only allowed the determination of a pure high-spin state by using the RILIS selectivity. The low-spin state was always mixed with the high-spin state. Thus, it was difficult to produce a pure ground state beam. This was especially true in the case of ^{199g}Po, where

the yield of the low-spin was too low compared to the high-spin. This resulted in only the high-spin state being measured for this isotope.

In addition to the selection offered by the RILIS, the difference in the half-lives between the ground and isomeric states of ^{195}Po allowed modification of the ratio between the two states in favour of the low-spin state. For ^{197}Po, the half-lives are too long-lived, therefore only a pure high-spin or a mixture of the two states with comparable ratios could be obtained.

The present work has succeeded in measuring the masses of $^{195,197(g,m)}$Po with the high-precision Penning-trap mass spectrometry. Based on the precise mass values, the state ordering and the excitation energy of the high-spin $13/2^+$ states in ^{195,197}Po were obtained for the first time. From this, the excitation energy of the states linked by α-decay chains was also determined. The results of the mass measurements provide information on the behaviour of the $13/2^+$ states in the lead region near $N = 104$, which remain in an excited state as a result of the pairing force in high-j orbitals. This is in contrast to the $11/2^-$ state in the Sn region, which becomes the ground state between $N = 73$ and $N = 77$.

Within this work, the benefit was taken from the MR-ToF MS resolving power to perform decay spectroscopy measurements with less contamination. Thus, decay information was collected in isobarically pure conditions. The half-lives of $^{195(g,m)}$Po were obtained by fitting half-life curves with ML and LS methods. The ML method is generally suited to analysing data due to the low yield in this experiment. The possible effect that could affect results (such as instability of count rate) has been corrected for. The resulting ^{195g}Po half-life value is in agreement with the literature value while improving the precision of the value. The ^{195m}Po half-life value is significantly smaller than the literature value.

Besides these successful measurements, $\alpha - \gamma$ coincidences benefited from isobaric-free conditions. When gating on the two γ-ray transition at 597.2 keV and 669.7 keV, coincident α lines were observed at 6027 keV and 6047 keV, respectively. However, the coincidences studies were limited by production yield in this experiment.

Finally, this work extends the knowledge about the excitation energy of the $13/2^+$ state in the lead region by measuring the masses of the $3/2^-$ and $13/2^+$ states in ^{195,197}Po. The new information completes the energy systematics of the odd-A isotopes in this region. The evolution of the nuclear structure in the neutron-deficient lead region and, in particular, the competition between the neutron $\nu_i 13/2$ and $\nu_p 3/2$ can become important ingredients to establish a theoretical research in the future. Experimentally, the precision mass measurement of ^{199m}Po will provide a new constraint on the ME of ^{199g}Po with improved uncertainty. In terms of the technical aspects, the precision on mass measurements at ISOLTRAP setup will further improve in the future. A new approach using the Phase-Imaging Ion-Cyclotron-Resonance (PI-ICR) method is currently being developed [111]. In this method, the cyclotron frequency is measured by the projection of the radial motion onto a high-resolution position-sensitive detector. The new approach is 25-times faster and offers a 40-fold increased resolving power. With this new technique, mass measurements of species that have low production or short-lived will be accessible with a relative mass uncertainty of 10^{-9} [111]. Additionally, the successful operation of the α-decay-spectroscopy setup with the resolving power of ISOLTRAP's MR-ToF MS will open the door for more decay spectroscopy studies in isobaric-free conditions at ISOLTRAP.

The remainder of this page was intentionally left blank.

Appendix A

A.1 Simulation of the depth distribution

This Appendix includes some output files of TRIM calculations that were performed on ^{195m}Po to determine the geometric efficiency.
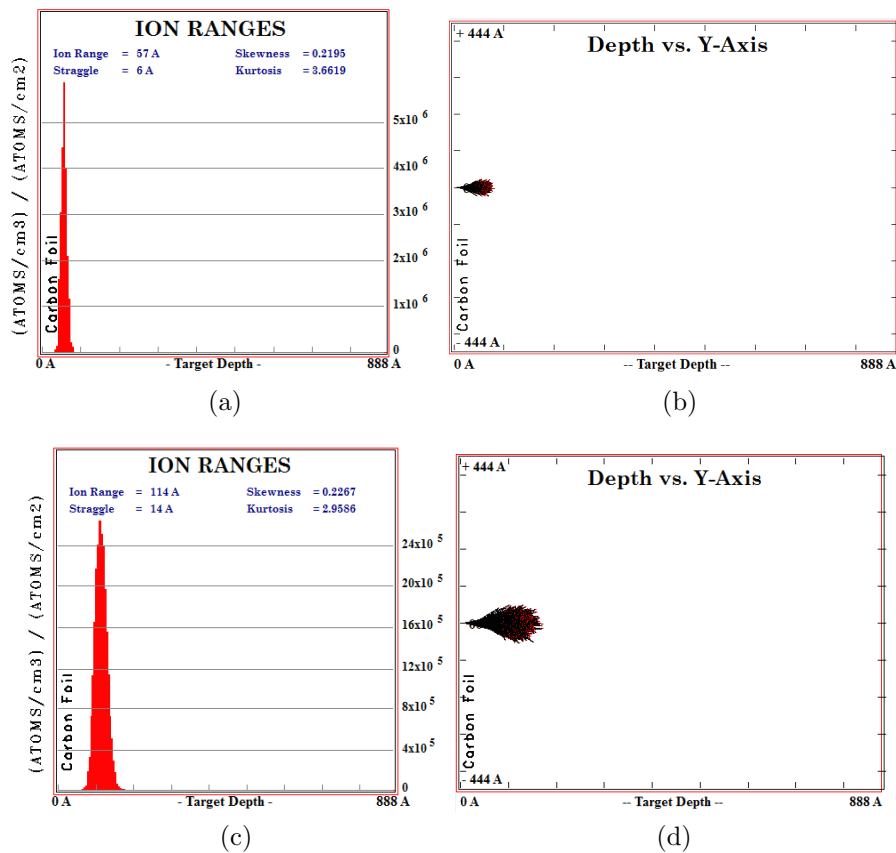

Figure A.1: Ranges of ^{195m}Po ions in the C-foil. (a) and (b) represent ions with 3 keV implantation energy, while (c) and (d) represent 13 keV implantation energy (the broad peak results as the ions get deeper into the target).

Figure A.1 shows the final distribution of ^{195m}Po ions that were implanted into the target. The numerical values are tabulated and shown in Fig. A.2.

```
============================ SRIM-2013.00 ============================
======================================================================
===== TRIMOUT.txt: File of Transmitted / Backscattered / Sputtered Atoms =====
=  This file tabulates the kinetics of ions or atoms leaving the target.    =
=  Column #1: S= Sputtered Atom, B= Backscattered Ion, T= Transmitted Ion.  =
=  Col.#2: Ion Number, Col.#3: Z of atom leaving, Col.#4: Atom energy (eV). =
=  Col.#5-7: Last location:  X= Depth into target, Y,Z= Transverse axes.    =
=  Col.#8-10: Cosines of final trajectory.                                  =
= *** This data file is in the same format as TRIM.DAT (see manual for uses).=
-- He 2 6699000 50.014 1.6009 -1.6406 0.915891 0.086444 -0.39201
 Ion  Atom    Energy         Depth      Lateral-Position        Atom Direction
 Numb Numb     (eV)          X(A)       Y(A)       Z(A)      Cos(X)  Cos(Y) Cos(Z)
 B    1   2 .6695085E+07 -  4133195E-07  .2985E+02  .2752E+03  -.2007225  .0714666  .9770379
 T    2   2 .6672426E+07    8893059E-04  .1708E+02 -.9761E+03  .6473142  .0195082 -.7619736
 B    3   2 .6686324E+07 -  9218540E-07  .4048E+02 -.3574E+03  -.1347515  .1308734 -.9821987
 B    4   2 .6689918E+07 -  7122715E-07 -.1734E+02  .6300E+01  -.9006719 -.4298725  .0632435
 B    5   2 .6689366E+07 -  1485636E-07 -.4602E+02  .1568E+02  -.7663419 -.6090326  .2044493
 B    6   2 .6686928E+07 -  6146306E-06 -.1019E+03 -.1185E+03  -.3882358 -.6354538 -.6674365
 B    7   2 .6687990E+07 -  6492880E-07  .7396E+02 -.7617E+00  -.5947798  .7978433 -.0984025
 B    8   2 .6688546E+07 -  1794104E-06 -.5683E+02 -.1432E+03  -.3624162 -.2898342 -.8858051
 T    9   2 .6648810E+07    8880700E-04 -.2444E+04  .1768E+04  .2660979 -.7819190  .5637327
 B   10   2 .6697239E+07 -  5675411E-06  .1807E+03  .1004E+02  -.3189044  .9469305  .0402817
 B   11   2 .6683499E+07 -  6732905E-07 -.3828E+03  .4328E+03  -.0980822 -.6521194  .7517448
 T   12   2 .6653841E+07    8880668E-04 -.4280E+03  .2065E+04  .3651253 -.1874701  .9118873
 T   13   2 .6669195E+07    8881285E-04  .1039E+04  .1045E+03  .6242931  .7772435  .0784255
 T   14   2 .6553498E+07    8881277E-04  .8975E+04 -.6880E+03  .0913532  .9930572 -.0741074
 T   15   2 .6615089E+07    8880362E-04  .3181E+04  .3472E+04  .1740913  .6661455  .7252188
 T   16   2 .6670796E+07    8880291E-04 -.1250E+04  .1008E+04  .4582811 -.6905276  .5595981
 T   17   2 .6584161E+07    8882276E-04 -.1560E+00  .7232E+04  .1142022  .0008482  .9934572
 B   18   2 .6688725E+07 -  1317234E-06  .5691E+02  .2579E+02  -.7598084  .6108131  .2227076
 B   19   2 .6687377E+07 -  1296313E-06  .1816E+03 -.9685E+02  -.2579413  .8455010 -.4675407
 T   20   2 .6672512E+07    8892121E-04  .1220E+03  .7696E+03  .7247041  .1088809  .6804035
 T   21   2 .6674731E+07    8887933E-04  .5475E+03 -.2605E+03  .8094966  .5317789 -.2488503
 T   22   2 .6677096E+07    8893988E-04  .3116E+03  .3275E+03  .8776522  .3230154  .3541012
 T   23   2 .6622034E+07    8882814E-04 -.4648E+03 -.4995E+04  .1636726 -.0921305 -.9822033
```

Figure A.2: The output TRIM file. The first column displays event name: B (T) stands for the backscattered (transmitted) ions. The second column displays the number of events. The third and forth columns represent the ion atomic number and the energy (in eV unit), respectively. The depth of the ion in the target is shown in the fifth column, it is a positive (negative) number for the transmitted (backscattered). The rest of the columns show the position of the ions in Y and Z axis and their directions [85, 86].

The remainder of this page was intentionally left blank.

Appendix B

B.1 Calculation of the peak area

The peak is usually contaminated by background signals. To extract the exact counts under the peak of interest, a background subtraction should be applied. The exact counts of the peak A above the background is given by subtracting the background areas (left, (B_L) and right (B_R)) from the total counts of the peak P [110]:
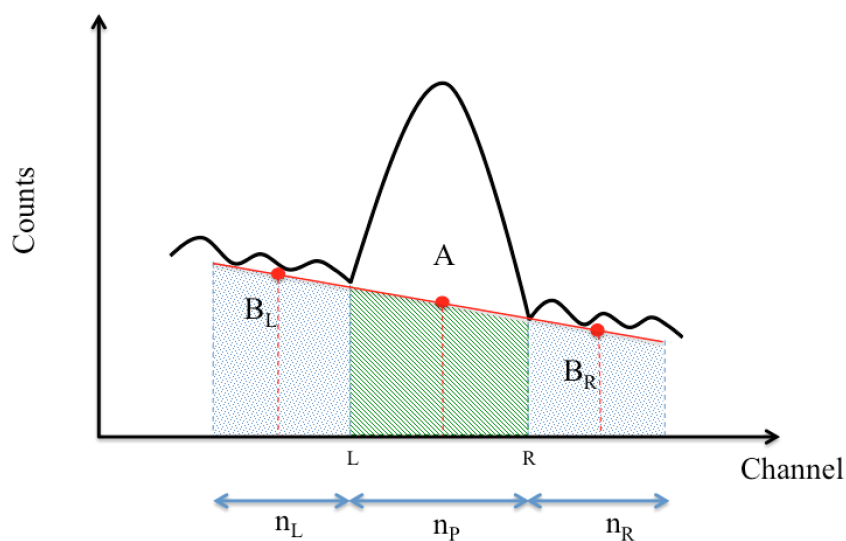

Figure B.1:   Calculating the peak area by using the left B_L and right B_R background areas.

$$A = P - \frac{n_P}{2}\left(\frac{B_L}{n_L} + \frac{B_R}{n_R}\right),$$ (B.1)

where $B_L = \sum\limits_{i=L-n_L}^{L} C_i$ is the is the counts average over n_L channels and $B_R = \sum\limits_{i=R}^{R+n_R} C_i$ is the is the counts average over n_R channels.

The remainder of this page was intentionally left blank.

Bibliography

[1] K. Heyde and J. L. Wood, Rev. Mod. Phys. **83**, 1467 (2011).

[2] N. Bree *et al.*, Phys. Rev. Lett. **112**, 162701 (2014).

[3] K. Heyde *et al.*, Phys. Rep. **102**, 291 (1983).

[4] A. M. Oros *et al.*, Nucl. Phys. A **645**, 107 (1999).

[5] K. Heyde *et al.*, Phys. Lett. B **155**, 303 (1985).

[6] K. Heyde *et al.*, Nucl. Phys. A **466**, 189 (1987).

[7] A. N. Andreyev *et al.*, Nature **405**, 430 (2000).

[8] R. Julin, K. Helariutta and M. Muikku, J. Phys. G **27**, R109 (2001).

[9] J. Elseviers *et al.*, Phys. Rev. C **84**, 034307 (2011).

[10] P. Rahkila *et al.*, Phys. Rev. C **82**, 011303(R) (2010).

[11] N. Kesteloot *et al.*, Phys. Rev. C **92**, 054301 (2015).

[12] K. Van de Vel *et al.*, Eur. Phys. J. A **17**, 167 (2003).

[13] F. G. Kondev and S. Lalkovski, Nucl. Data Sheets **112**, 707 (2011).

[14] M. Anselment *et al.*, Phys. Rev. C **34**, 1052 (1986).

[15] F. Le Blanc *et al.*, Phys. Rev. C **72**, 034305 (2005).

[16] C. Weber *et al.*, Phys. Lett. A **347**, 81 (2005).

[17] A. N. Andreyev *et al.*, Phys. Rev. C **66**, 014313 (2002).

[18] J. Sauvage *et al.*,   Eur. Phys. J. A **49**, 109 (2013).

[19] P. Ring and P. Schuck. *The nuclear many-body problem*, Springer-Verlag, (1980).

[20] J. Stanja *et al.*, Phys. Rev. C **88**, 054304 (2013).

[21] Ch. Böohm *et al.*, Phys. Rev. C **90**, 044307 (2014).

[22] C. Van Beveren *et al.*, Phys. Rev. C **92**, 014325 (2015).

[23] M. Mukherjee *et al.*, Eur. Phys. J. A **35**, 1 (2008).

[24] S. Kreim *et al.*, Nucl. Instrum. Meth. Phys. Res. Sec. B **317**, 492 (2013).

[25] S. Rothe *et al.*, Nucl. Instrum. Meth. Phys. Res. Sec. B **317**, 561 (2013).

[26] V. N. Fedosseev*et al.*, Rev. Sci. Instrum. **83**, 020000 (2012).

[27] B. A. Marsh *et al.*, Hyp. Interact. **227**, 101 (2014).

[28] E. Kugler, Hyp. Interact. **129**, 23 (2000).

[29] R. N. Wolf *et al.*, Int. J. Mass Spectrom. **349**, 123 (2013).

[30] R. N. Wolf *et al.*, Phys. Rev. Lett. **110**, 041101 (2013).

[31] T. E. Cocolios *et al.*, Phys. Rev. Lett. **106**, 052503 (2011).

[32] M. D. Seliverstov *et al.*, Phys. Lett. B **719**, 362 (2013).

[33] G. Gamow, *et al.*, Proc. Roy. Soc. London A **126**, 632 (1930).

[34] C. F. v. Weizsäcker, Z. Phys. **96**, 431 (1935).

[35] H. A. Bethe and R.F. Bacher, Rev. Mod. Phys. **8**, 82 (1936).

[36] E. Wigner, Phys. Rev. **51**, 106 (1937).

[37] N. D. Cook. *Models of the Atomic Nucleus*, Springer-Verlag Berlin Heidel-berg (2010).

[38] W. D. Myer. *Droplet model atomic nuclei*, Plenum New York NY (1977).

[39] K. S. Krane. *Introductory nuclear physics*, Wiley New York NY (1988).

[40] M. G. Mayer, Phys. Rev. **75**, 1967 (1949).

[41] O. Haxel, J. Jensen, and H. Suess, Phys. Rev. **75**, 1766 (1949).

[42] M. G. Mayer, Phys. Rev. **74**, 235 (1948).

[43] K. Heyde. *The nuclear shell model* , Wiley Springer Berlin (1994).

[44] M. Bender, P.-H. Heenen and P.-G. Reinhard, Rev. Mod. Phys. **75**, 121 (2003).

[45] E. Caurier *et al.*, Rev. Mod. Phys. **77**, 427 (2005).

[46] B. G. Hogg and H. E. Duckworth, Phys. Rev. **91**, 1289 (1953).

[47] E. A. McClatchie *et al.*, Phys. Rev. C **1**, 1828 (1970).

[48] J. Lilley. *Nuclear Physics*: *Principles and Applications*, Wiley-Blackwell (2001).

[49] E. Aprile *et al.*, Phys. Rev. D **59**, 072008 (2017).

[50] A.Grau Malonda and A.Grau Carles, Appl. Radiat. Isot. **56**, 153 (2002).

[51] F. G. Major, V. N. Gheorghe, and G. Werth. *Charged Particle Traps*, Springer (2005).

[52] L. S. Brown and G. Gabrielse, Rev. Mod. Phys. **58**, 233 (1986).

[53] H. G. Dehmelt and F. L. Walls, Phys. Rev. Lett **21**, 127 (1968).

[54] K. Blaum *et al.*, Contemp. Phys. **51**, 149 (2010).

[55] G. Savard *et al.*, Phys. Lett. A **158**, 247 (1991).

[56] G. Gräff, H. Kalinowsky and J.Traut, Z. Phys. A **297**, 35 (1980).

[57] M. König *et al.*, Int. J. Mass Spectrom. **142**, 95 (1995).

[58] G. Bollen *et al.*, Nucl. Instrum. Meth. Phys. Res. Sec. A **368**, 675 (1996).

[59] G. Bollen *et al*., J. Appl. Phys. **68**, 4355 (1990).

[60] Isolde.web.cern.ch, http://isolde.web.cern.ch/isolde.

[61] J. Al-Khalili and E. Roeckl. *The Euroschool Lectures on Physics with ExoticBeams*, Springer Berlin Heidelberg (2006).

[62] E. Bouquerel *et al*., Nucl. Instrum. Meth. Phys. Res. Sec. B **266**, 4298 (2008).

[63] R. Kirchner, Nucl. Instrum. Meth. Phys. Res. **186**, 275 (1981).

[64] L. Penescu *et al*., Rev. Sci. Instrum. **81**, 02A906 (2010).

[65] B. Jonson and A. Richter, Hyp. Interact **129**, 1 (2000).

[66] A. Herlert, Nucl. Phys. News **20**, 5 (2010).

[67] F. Herfurth *et al*., Nucl. Instrum. Meth. Phys. Res. Sec. A **469**, 254 (2001).

[68] N. A. Althubiti *et al*., Phys. Rev. C **96**, 044325 (2017).

[69] H. Schnatz *et al*., Nucl. Instrum. Meth. Phys. Res. Sec. A **251**, 17 (1986).

[70] H.-J. Kluge *et al*., Int. J. Mass Spectrom. **349**, 26 (2013).

[71] F. Wienholtz *et al*., Phys. Scr. **T166**, 014068 (2015).

[72] F. Wienholtz *et al*., Nature **498**, 346 (2013).

[73] M. Rosenbusch *et al*., Phys. Rev. Lett. **114**, 202501 (2015).

[74] H. Raimbault-Hartmann *et al*., Nucl. Instrum. Meth. Phys. Res. Sec. B **126**, 378 (1997).

[75] A. Kellerbauer *et al*., In: Eur. Phys. J. D **22**, 53 (2003).

[76] C. Bohm. *Setup of a carbon-cluster laser ion source and the application of the invariance theorem at ISOLTRAP*, Diploma thesis,(2009).

[77] M. Marie-Jeanne, *et al*., Nucl. Instrum. Meth. Phys. Res. Sec. A **587**, 464 (2008).

[78] G. Bollen Nucl. Phys. A **693**, 3 (2001).

[79] A. Kellerbauer *et al.*, Nucl. Instrum. Meth. Phys. Res. Sec. A **469**, 276 (2001).

[80] M. Kowalska *et al.*, Nucl. Instrum. Meth. Phys. Res. Sec. A **689**,102 (2012).

[81] S. Naimi. *Onsets of nuclear deformation from measurements with the Isoltrap mass spectrometer*. PhD thesis (2010).

[82] K. M. Lynch *et al.*, Nucl. Instrum. Meth. Phys. Res. Sec. A **844**, 14 (2017).

[83] SIMION. http://simion.com.com.

[84] D. A. Dahl , Int. J. Mass Spectrom. **200**, 3 (2000).

[85] SRIM. http://www.srim.org/.

[86] J. F. Ziegler, J. P. Biersack and M. D. Ziegler. *SRIM the Stopping and Range of Ions in Matter*, (2008).

[87] J. Wauters *et al.*, Phys. Rev. C. **47**, 1447 (1993).

[88] K. Debertin and R. G. Helmer. *Gamma-* and $X - Ray$ *Spectrometry with Semiconductor Detectors*, North-Holland, (1988).

[89] S. Tavernier. *Experimental Techniques in Nuclear and Particle Physics*, Springer, (2010).

[90] T. E. Cocolios *et al.*, J. Phys. G **37**, 125103 (2010).

[91] L. Lista. *Statistical Methods for Data Analysis in Particle Physics* First Edition, Springer (2016).

[92] I. Antcheva *et al.*, Comput. Phys. Commun. **180**, 2499 (2009).

[93] F. James and M. Roos, Comput. Phys. Commun. **10**, 343 (1975).

[94] F. Wienholtz *et al.*, Int. J. Mass Spectrom. **285**, 421 (2017).

[95] G. Bollen *et al.*, Phys. Rev. C **46**, R2140(R) (1992).

[96] G. Audi *et al.*, Chin. Phys. C **41**, 030001 (2017).

[97] M. Wang *et al.*, Chin. Phys. C **41**, 030003 (2017).

[98] D. Lascar *et al.*, Phys. Rev. C **96**, 044323 (2017).

[99] P. Dabkiewicz *et al.*, Phys. Lett. B **82**, 199 (1979).

[100] M. D. Seliverstov *et al.*, Eur. Phys. J. A **41**, 315 (2009).

[101] M. D. Seliverstov *et al.*, Phys. Rev. C **89**, 034323 (2014).

[102] G. Ulm *et al.*, Z. Phys. A **325**, 247 (1986).

[103] H. De Witte *et al.*, Phys. Rev. Lett. **98**, 112502 (2007).

[104] A. SIIVOLA, Nucl. Phys. A **101**, 129 (1967).

[105] J. Uusitalo *et al.*, Phys. Rev. C **71**, 024306 (2005).

[106] R. N. Wolf *et al.*, Nucl. Instrum. Meth. Phys. Res. Sec. B **376**, 275 (2016).

[107] J. Van Roosbroeck *et al.*, Phys. Rev. Lett. **92**, 112501 (2004).

[108] G. Gilmore, J. D. Hemingway. *Practical Gamma Ray Spectrometry*. John Wiley Sons, New York (1995).

[109] S. Baker-Cousins and R. D. Cousins, Nucl. Instrum. Meth. Phys. Res. **221**, 437 (1984).

[110] R. Van Grieken and A. Markowicz. *Handbook of X-Ray Spectrometry*, Second Edition, CRC Press (2001).

[111] S. Eliseev *et al.*, Appl. Phys. B **114**, 107 (2014).